NTNU – Trondheim
Norwegian University of
Science and Technology

Numerical Modelling of a Pile Model Test with Focus on Small-strain Stiffness

Jørn Hetland

Civil and Environmental Engineering
Submission date: Januar 2015
Supervisor: Gudmund Reidar Eiksund, BAT

Norwegian University of Science and Technology
Department of Civil and Transport Engineering

NORWEGIAN UNIVERSITY OF SCIENCE AND TECHNOLOGY
DEPARTMENT OF CIVIL AND TRANSPORT ENGINEERING

Report Title: Laboratory Investigations and Numerical Modelling of a 1:20 scale Monopile Foundation.	Date: Number of pages (incl. appendices):				
	Master Thesis	X	Project Work		
Name: Jørn Hetland					
Professor in charge/supervisor: Gudmund Eiksund					
Other external professional contacts/supervisors:					

Abstract:

This thesis investigated the dynamic characteristics of a 1:20 scale model of a monopile offshore wind turbine foundation. For the scope of this Thesis, the focus was on back-calculations and numerical modelling of the model pile. First, however, the dynamic properties of the model pile was investigated in the laboratory. The eigenfrequency was investigated using strain gage measurements and were found to be in the range of 7.7 to 8.8 Hz for different values of overburden pressure, increasing with increased overburden pressure. Using the decay in the strain gage measurements, the damping properties of the Hokksund sand used in the experiments could also be investigated. This was performed using the method of logarithmic decay, and the damping properties were also found to vary with overburden pressure. Damping was observed to decrease with increased overburden pressure.

The eigenfrequency and damping properties of the soil were also found to be time-dependent, or more correctly amplitude-dependent. The eigenfrequency increased with time, and this was believed to be caused by the increased soil stiffness with decreasing strain amplitude. This is a feature of soils investigated by many researchers, and was implemented in the Hardening Soil Small model in PLAXIS. The damping ratio found by the method of logarithmic decay also varied significantly with time. Decreased damping ratio with time or amplitude was observed from the laboratory tests. Soil damping is caused by friction between grains and irreversible plastic strains. Thus, the decreasing damping ratio observed with time was believed to have been caused by the reduced amplitude reducing the amount of friction and irreversible strains.

Numerical modelling of the problem was performed using the FEM-software PLAXIS 3D. Two different material models were used. First the problem was solved using linear elastic soil with increasing stiffness with depth. This was found to give a good estimate of the system's first eigenfrequency, overestimating it with a factor of around 1.03. However, the Hardening Soil Small model performed significantly better, overshooting the eigenfrequency only by a factor of around 1.01.

On the basis of these results it can be concluded that PLAXIS 3D is well-suited for numerical modelling of the model pile. It can also be concluded that the stiffness found from shear wave measurements gives a good estimate with regards to the soil stiffness that should be used for such structures. Although mostly influenced by the structural stiffness, the eigenfrequency was found to be significantly influenced by the soil stiffness, and using stiffness found from conventional laboratory testing would in this case significantly underestimate the system eigenfrequency.

Keywords:

1. Geotechnical Engineering
2. Soil Dynamics
3. Dry Sand
4. Soil Modelling

Acknowledgements

I would like to thank Professor Gudmund Eiksund for his continuous guidance during the semester and for always welcoming questions and discussion regarding my Thesis. Especially helpful was his advice regarding numerical modelling of the problem. Also, I would like to thank PhD candidate Stian Baardsgaard Hanssen for a good cooperation during laboratory work and for welcoming discussion regarding results and result interpretation.

Preface

This thesis is the result of the work carried out at NTNU during the autumn semester of 2014. The thesis work was conducted in cooperation with a research project within the field of monopile offshore wind turbine foundations, and the Thesis should also be viewed in connection with a project work performed during the spring of 2014. During this project work, instrumentation, calibration and preparation of the laboratory setup was carried out.

The main scope of this master thesis, was to perform back-calculations of the laboratory investigations. The work went through different phases: Starting with laboratory work, enabling result interpretation and determination of important parameters and characteristics of the model pile. Then the focus was on back-calculations, where accurate modelling of the problem was of main concern. The laboratory results were then compared to the results from the numerical model and conclusions were drawn on this basis.

The process of conducting this master thesis was very demanding as well as educational and interesting. Having a varied range of tasks concerning laboratory work, literature study as well as numerical modelling made the work even more interesting.

Summary

This thesis investigated the dynamic characteristics of a 1:20 scale model of a monopile offshore wind turbine foundation, and performed numerical modelling of the model pile using the FEM-software PLAXIS 3D. The build-up of the laboratory model as well as pile instrumentation was performed in a project work during the spring of 2014.

For the scope of this thesis, the focus was on back-calculations and numerical modelling of the model pile. First, however, the dynamic properties of the model pile was investigated in the laboratory. The first eigenfrequency was investigated using strain gage measurements, and were found to be in the range of 7.7 to 8.8 Hz for different values of overburden pressure, increasing with increased overburden pressure. Using the decay in the strain gage measurements, the damping properties of the Hokksund sand used in the experiments could also be investigated. This was performed using the method of logarithmic decay, and the damping properties were also found to vary with overburden pressure. Damping was observed to decrease with increased overburden pressure.

The eigenfrequency and damping properties of the soil were also found to be time-dependent, or more correctly amplitude-dependent. The eigenfrequency increased with time, and this was believed to be caused by the increased soil stiffness with decreasing strain amplitude. This is a feature of soils investigated by many researchers, and is a feature Benz (2006) implemented in the Hardening Soil Small material model in PLAXIS. The damping ratio found by the method of logarithmic decay also varied significantly with time. Decreased damping ratio with time or amplitude was observed from the laboratory tests. Soil damping is caused by friction between grains and irreversible plastic strains. Thus, the decreasing damping ratio observed with time was believed to have been caused by the reduced amplitude reducing the amount of friction and irreversible strains.

Numerical modelling of the problem was performed using the FEM-software PLAXIS 3D. This software is well-known to geotechnical engineers, and its application to problems of this sort is therefore of great interest. An effort was made to model the laboratory conditions in an accurate manner, describing the physical conditions in the laboratory. The model pile was assumed to operate in the small-strain range, and soil stiffness was found by shear wave measurements. In order to reduce computational time, a half model was created. This was found to model the problem in a good manner.

Two different soil models were used. First the problem was solved using linear elastic soil with increasing stiffness with depth. This was found to

give a good estimate of the system's first eigenfrequency, overestimating it with a factor of around 1.03. However, the Hardening Soil Small model performed significantly better, overshooting the first eigenfrequency only by a factor of around 1.01.

The series without overburden pressure was found to have a larger error than the other series when comparing the numerical model to laboratory investigations. Structures of this type are believed to operate in the small-strain range, and therefore soil stiffness can be well-estimated using shear wave measurements. However, for the model pile in this case with a relatively low embedded length and relatively low stiffness without the use of overburden pressure, it was believed that larger strains occured, causing the model pile to behave too soft compared to the numerical model with assumptions of small-strain stiffness.

On the basis of these results it can be concluded that PLAXIS 3D is well-suited for numerical modelling of the model pile. It can also be concluded that the stiffness found from shear wave measurements gives a good estimate with regards to the soil stiffness that should be used for such structures. Although mostly influenced by the structural stiffness, the eigenfrequency was found to be significantly influenced by the soil stiffness, and using stiffness found from conventional laboratory testing would in this case significantly underestimate the first eigenfrequency.

Samandrag

Denne masteroppgåva utforska dei dynamiske eigenskapane til eit monopel offshore vindmøllefundament konstruert i skala 1:20. I tillegg vart numerisk modellering med elementmetodeprogrammet PLAXIS 3D utført. Modellen vart laga i samband med eit prosjektarbeid utført ved NTNU våren 2014, der óg instrumentering av pelen vart gjennomført.

Denne oppgåva er avgrensa til å omhandla numerisk modellering av laboratoriemodellen ved bruk av elementmetodeprogrammet PLAXIS 3D. Før tilbakerekninga kunne gjennomførast vart dei dynamiske eigenskapane utforska ved bruk av laboratorieforsøk. Systemet sin første eigenfrekvens vart bestemt ved bruk av strekklappmålingar, og vart funnen til å variere mellom 7.7 til 8.8 Hz for ulike overtrykk. Høgare overtrykk gav høgare eigenfrekvens grunna auka jordstivleik ved høgare effektivspenningsnivå. Strekklappmålingane vart undersøkt ved bruk av logaritmisk dekrement, og det vart funne at jorddempinga minka ved høgare effektivspenningsnivå.

Eigenfrekvens og demping vart funne til å variere med tid i dei ulike målingsseriane. Eigenfrekvensen auka med tid, noko som kan forklarast med den aukande jordstivleiken med minkande amplitude. Dette er ein eigenskap ved jord som mange forskarar er enige om, og som mellom anna Benz (2006) tok i bruk i si doktoroppgåve til å lage ein jordmodell i PLAXIS. Dempinga derimot minka med tid, eller meir korrekt; den minka med minkande amplitude. Jorddemping oppstår grunna friksjon mellom korn og plastiske deformasjonar. Når amplituden vert mindre, vert óg dempinga mindre.

Jordstivleiken vart funnen med målingar av skjærbølgesnøggleik. Dette saman med strukturstivleiken danna grunnlaget for numerisk modellering som vart utført ved bruk av to ulike materialmodellar. Den lineær-elastiske modellen overestimerte den første eigenfrekvensen til systemet med ein faktor på rundt 1.03, medan modelleringa med Hardening Soil Small overestimerte eigenfrekvensen med ein faktor på rundt 1.01. Dette var som venta grunna Hardening Soil Small modellen sin eigenskap til å redusere jordstivleiken med amplitude.

Målinga utan overtrykk vart funnen å ha større feil enn dei resterande målingane. Dette er truleg grunna at den nedseinka delen av pelen er låg samanlikna med den verkelege situasjonen. Dette kombinert med låg jordstivleik for dette tilfellet forårsakar større feil enn i dei resterande forsøka.

På bakgrunn av desse resultata kan det konkluderast med at PLAXIS 3D er godt eigna for berekning av slike problem. Det kan óg konkluderast med at jordstivleiken frå skjærbølgemålingar gir eit bra estimat for jordstivleik til å bruke i slike tilfelle. Sjølv om eigenfrekvensen til systemet er mest

påverka av strukturen sin stivleik, spelar óg jorda ei vesentleg rolle, og dersom jordstivleiken frå konvensjonelle undersøkingsmetodar hadde blitt teken i bruk, ville eigenfrekvensen vorte underestimert i dette tilfellet.

Contents

Chapter 1

Introduction

1.1 Background

There exists significant political interest to expand the production of offshore wind energy. Due to high production costs, an effort is made to optimize the design of offshore wind turbines. This master thesis is written in cooperation with a research project which aims at improving design methods for monopile offshore wind turbine foundations.

Due to the nature of the excitation forces, the horizontal foundation stiffness is of great interest for these structures. The eigenfrequency is, to a large extent, affected by the structural stiffness. However, soil stiffness also influences and is shown to have been underestimated by current design methods. Offshore wind turbines are subjected to harsh environmental conditions due to loading from wind and waves. Underestimating soil stiffness and thus eigenfrequency could cause more fatigue and could in worst case scenario cause structural failure.

One of the methods used for determination of the lateral stiffness of monopile offshore wind turbine foundations, is the well-known $p-y$ curves. Replacing the soil with discrete lateral springs with stiffness based on $p-y$ curves, enables efficient calculation of the many load cases needed for safe design of such structures. Figure 1.1 shows two different idealizations of such a structure, where the soil is modelled as springs and viscous dampers (left) and as a cantilever beam with equivalent length (right). The wind turbine itself is modelled as a lumped mass on top of the structure.

Soil stiffness is known to vary depending on soil type as well as stress- and strain magnitude. The large diameter monopiles used for such structures are believed to operate in the small-strain range, and the soil should therefore exhibit larger stiffness than for conventional foundation types.

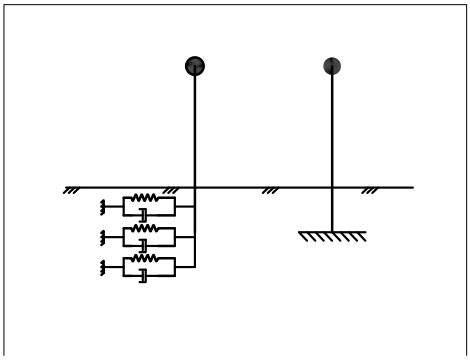

Figure 1.1: Beam on elastic foundation (left) and cantilever beam (right) with equivalent length

1.2 Problem Formulation

Stress-strain behaviour of laterally loaded piles is a complex problem without any known analytical solution. This thesis aims at evaluating the performance of a numerical solution to the problem. A 1:20 scale model of a monopile foundation is loaded laterally by an impact load, and a numerical model is created using a dynamic 3D FEM-software. The performance of a FEM-software is highly dependent on the material model and its applicability to the problem. Therefore the performance of two different soil models is evaluated and compared to laboratory measurements. An effort is made to ensure that the measurements performed in the laboratory are of high quality and comparable to the numerical model.

1.3 Objective

This thesis consists of three main objectives:

- Performing laboratory measurements to establish reliable parameters for back-calculation.
- Creating a numerical model representative for the physical conditions of the laboratory tests.
- Evaluating the performance of two different soil models as well as their applicability to the problem.

1.4 Thesis Structure

This master thesis consists of a theoretical background within wave propagation and dynamic properties of soils, including soil stiffness and soil damping. The basic concept of the Finite Element Method will also be explained, and a review of the different material models appropriate to this problem will be performed. Laboratory results and result interpretation will be presented as well as results from the back-calculations. The numerical results will be compared to the laboratory measurements and at last conclusions will be drawn. An effort will also be made to put this thesis in context with the research project.

Part I

Theoretical Background

Chapter 2

Wave Propagation

2.1 Introduction

Due to the continuous nature of soils and geological material, their dynamic behaviour is often understood in the context of wave propagation. While most structures can be idealized as a set of discretized masses with corresponding stiffnesses, soils in most cases can not. Therefore, in order to fully understand the dynamical behaviour of soils, elastic wave propagation must be considered.

Materials consist of atoms which can be vibrated about their position of equilibrium. When the particles produce a unison movement, they can be considered to create a mechanical wave. Such waves will propagate through a material until it reaches the material boundaries, where they will be reflected or transmitted depending on the boundary conditions. In an infinite elastic medium there is considered to be only two types of waves: P-waves and S-waves. In an elastic half space, however, boundary conditions are introduced, which leads to two additional types of waves. These are called Rayleigh and Love waves. While Rayleigh waves are known to exist in a homogeneous elastic half-space, Love waves require a surficial layer of lower S-wave velocity and is therefore outside the scope of this thesis.

2.2 P-waves

P-waves are also called compressional waves due to their "push-pull" movement in the direction of propagation. Figure 2.1 shows the behaviour of a P-wave, inducing particle motion in the direction of propagation. P-waves will propagate radially from the source and be transmitted or reflected at the material boundary.

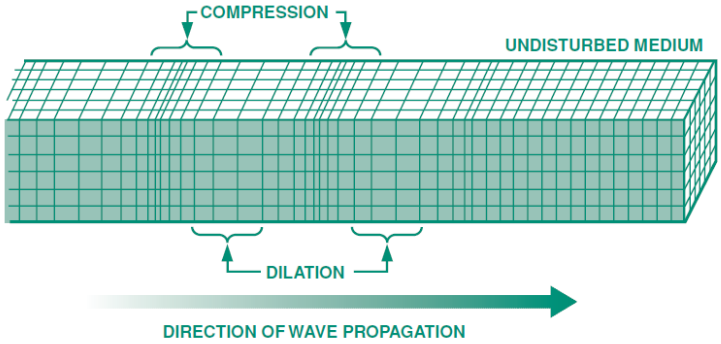

Figure 2.1: Dilate and compressive behaviour of a P-wave propagation through a material (Olivadoti (2001))

2.3 S-waves

S-waves are also called transverse waves and induce particle motion perpendicular to the propagation direction. Figure 2.2 shows a S-wave and the particle movement caused by such a wave.

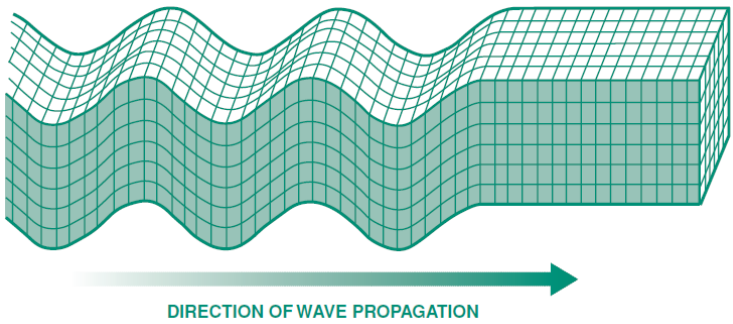

Figure 2.2: S-wave propagation through a material inducing particle motion in the direction perpendicular to the direction of propagation (Olivadoti (2001))

2.4 Rayleigh Waves

When there exists a boundary, there may also be a third type of waves called Rayleigh waves. Rayleigh waves can be seen as a combination of P- and S-waves, with particle motion induced in the direction of propagation as well as the transverse direction. These waves are confined to the boundaries of the material and their effect decrease with depth. Figure 2.3 shows a Rayleigh wave propagating through a material.

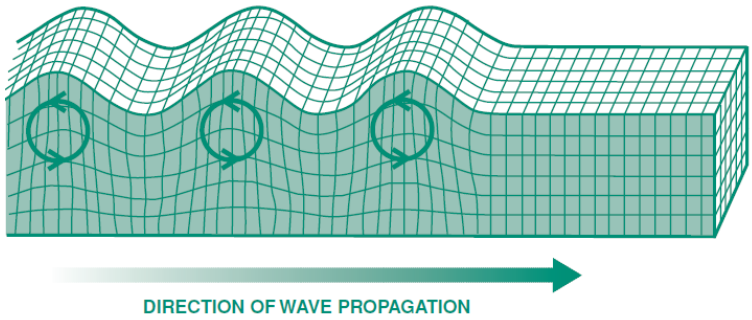

Figure 2.3: Rayleigh waves propagating through a material inducing a particle motion with similarities to both P- and S-waves (Olivadoti (2001))

2.5 Wave Propagation Characteristics

The main types of waves propagating through a material are as described above. These waves will propagate through a material with a certain velocity and wavelength, depending on the material and loading characteristics. These quantities for the different wave types will be described here.

2.5.1 Velocity

The wave velocity is of great interest for investigation of the dynamic response of soils. Determining the S-wave velocity allows for determination of the shear stiffness according to equation (2.2) when the density of the material is known. The propagation velocities in materials are dependent on the density and stiffness of the material. Equation (2.1) to (2.3) gives the wave velocity for P-, S- and Rayleigh waves respectively. As by Kramer (1996),

the Rayleigh wave velocity is defined in relation to the S-wave velocity.

$$V_P = \sqrt{\frac{E_{oed}}{\rho}} = \sqrt{\frac{(1-\nu)E}{\rho(1+\nu)(1-2\nu)}} \tag{2.1}$$

$$V_S = \sqrt{\frac{G}{\rho}} = \sqrt{\frac{E}{2\rho(1+\nu)}} \tag{2.2}$$

$$\frac{V_R}{V_S} = \alpha K_{Rs} = \sqrt{\frac{(1-2\nu)}{(2-2\nu)}} K_{Rs} \tag{2.3}$$

where E_{oed} is the oedometer stiffness, ρ is the material density, ν is the Poisson's ratio, E is the Young's modulus and G is the shear modulus of the material. Solutions for K_{Rs} can be found for various values of ν, and figure 2.4 shows how the wave velocities of the three wave types vary with Poisson's ratio, normalized with regards to V_S. As can be seen from figure 2.4, P-waves travel faster than S-waves. This is due to the stiffer behaviour of soils for volumetric compression than for shearing. The Rayleigh waves travel slightly slower than the S-waves.

2.5.2 Wavelength

When harmonic waves propagate through a material, they will travel with a characteristic length called wavelength. The wavelength describes how far distance a wave travels in the material for one period of loading. The wavelength is thus related to the propagation velocity and the frequency of applied loading.

$$\lambda = \frac{V}{f} \tag{2.4}$$

where V is the velocity of the corresponding wave and f is the frequency of the applied loading. The loading can either be an earthquake or an arbitrary source from which the waves are spreading.

2.6 Reflection of Waves

In reality, layering and boundaries will exist in a material and introduce wave reflections. Understanding how waves behave when reaching a material boundary, is important for considerations of how a foundation will act when subjected to dynamic loading. When a wave reaches an interface between two different materials, part of it will be reflected back into material

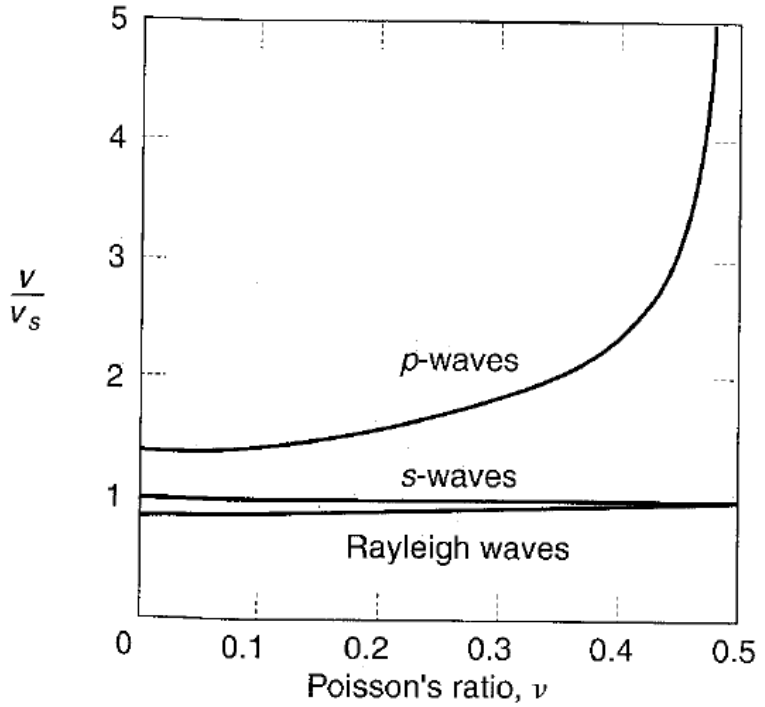

Figure 2.4: Wave velocities for the different wave types, normalized with regards to V_S (Kramer (1996))

1 and part of it will travel into material 2 with a wavelength λ_2. Considering an infinitely long rod with a material boundary (figure 2.5), it is possible to derive an expression for the reflected and transmitted amplitude A and stress σ depending on the wave velocity and density of the materials. Defining the impedance ratio as $\alpha_z = (\rho_2 V_2)/(\rho_1 V_1)$, the equations become (Kramer (1996)):

$$A_r = \frac{1-\alpha_z}{1+\alpha_z} A_i \tag{2.5}$$

$$A_t = \frac{2}{1+\alpha_z} A_i \tag{2.6}$$

$$\sigma_r = \frac{\alpha_z - 1}{1+\alpha_z} \sigma_i \tag{2.7}$$

$$\sigma_t = \frac{2\alpha_z}{1+\alpha_z} \sigma_i \tag{2.8}$$

where index r is for the reflected wave, t is for the transmitted wave and i is for the incident wave. Considering the special case where $\alpha_z = \infty$, the incoming wave will be fully reflected and there will be no transmittance. The special case of $\alpha_z = 0$ implies that the wave is approaching a free end and therefore no stress can be transmitted. Due to this condition, the displacement of the boundary must be twice the initial wave amplitude.

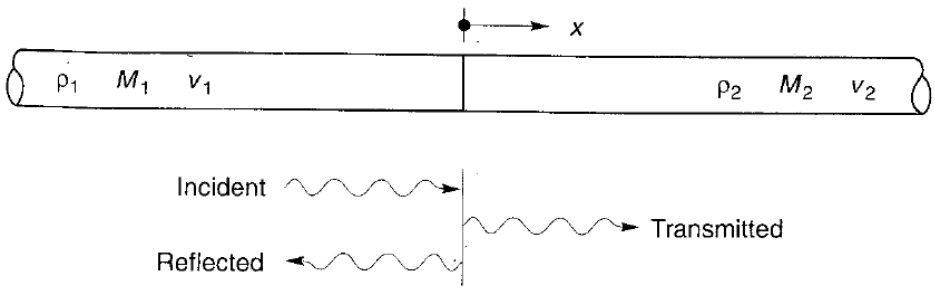

Figure 2.5: Infinetly long rod consisting of two different materials (Kramer (1996))

2.7 Attenuation of Waves

In homogeneous linear elastic material, waves travel an infinite distance without change in amplitude. In real materials, however, there will be a

certain amount of wave attenuation. This is partly due to material damping and partly due to geometrical damping, and will both cause energy dissipation in a system.

2.7.1 Material Damping

In reality, part of the energy from a travelling wave is transferred to the material as heat. For convenience, viscous damping is often used to describe this energy dissipation by the use of dashpots. However, this will give an elliptical damping, while soils dissipate energy hysteretically by the slippage and rearrangement of grains (Kramer (1996)). Figure 2.6 shows a load cycle for a soil, where the dissipated energy is proportional to the area inside the loop.

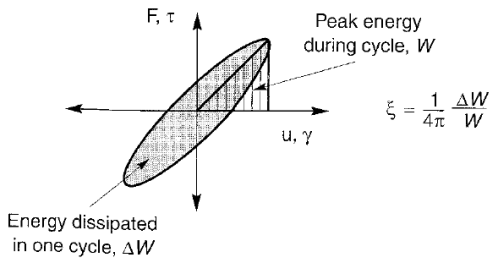

Figure 2.6: Hysteretic loop with damping ratio proportional to the area inside the loop (Kramer (1996))

2.7.2 Geometric Damping

Geometric damping can be best understood as the spreading of elastic energy over a larger area as the waves propagate through a material. Although the amount of energy is constant, the specific energy (energy per unit volume) will decrease. The energy decrease is found to be of rate $1/r$ for body waves and $1/\sqrt{r}$ for surface waves (Kramer (1996)), where r is the distance from the wave source.

Chapter 3

Dynamic Properties of Soils

One of the main challenges with regards to dynamic analysis of soil response, is the establishment of the dynamic properties of soils. The parameters found to be of major importance is the small-strain stiffness, also known as the dynamic moduli, and the damping ratio. These parameters also show significant dependencies on other soil parameters, and this subject will be treated in this Chapter.

3.1 Small-Strain Stiffness

3.1.1 Introduction

For many years it has been known that most soils, to some extent, show a non-linear, non-reversible stress-strain relationship. Soil stiffness is also found to be dependent on the strain level to which the soil is exposed. Therefore small-strain stiffness is defined as the stiffness soils exhibit at a small level of strains. There also exists a convention called *dynamic stiffness*. This expression developed due to the observed stiffer behaviour of structures subjected to dynamic loading. For many years this stiffer behaviour was believed to be caused by inertia effects. Today, however, many researchers believe that the stiffer behaviour is due to the fact that dynamic structures tend to operate at a lower strain level. Therefore, today, the dynamic moduli is normally referred to as small-strain stiffness. Figure 3.1 exemplifies this characteristic of soils. When exposed to a smaller strain level γ_1 soils show a stiffer behaviour which can be seen by $G_1 > G_2$ in figure 3.1. The nature of the dynamic problems is often related to the lateral loading of piles, where the shear modulus is of great importance. Another advantage of the shear modulus is that it relates to the shear wave velocity and density of a

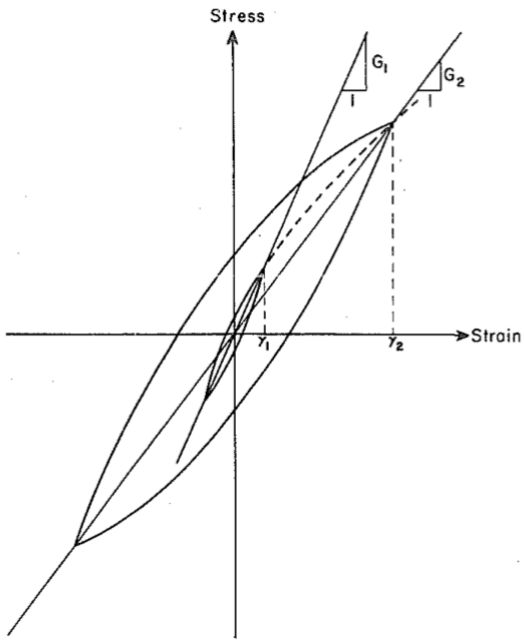

Figure 3.1: Stress-strain relation for a soil subjected to different strain amplitudes (Seed and Idriss (1970))

material, and can therefore be found by measurement of wave propagation velocity. A more well-known parameter, especially within problems related to steel and concrete, is Young's modulus E. Shear modulus G is related to Young's modulus by equation (3.1) from theory of elasticity.

$$G = \frac{E}{2(1+\nu)} \tag{3.1}$$

where ν is the Poisson's ratio of the soil.

Soil stiffness is also of great importance regarding geotechnical problems related to the settlement of foundations and displacement of retaining walls. However, for problems involving displacement of such structures, one is believed to operate at a higher strain level which means the stiffness is significantly reduced compared to the small-strain stiffness.

Definitions

Figure 3.2 shows strain ranges for different types of structures as well as the strain range at which the different laboratory tests are applicable. There exist no exact limit on the different strain ranges. However, shear strains $\gamma_s \leq 10^{-6}$ are defined as very small strains and $\gamma_s \geq 10^{-3}$ as larger strains by Benz (2006). This means small-strain stiffness is in the range of $10^{-6} \leq \gamma_s \leq 10^{-3}$. This will vary from soil to soil and should not be considered a fixed limit.

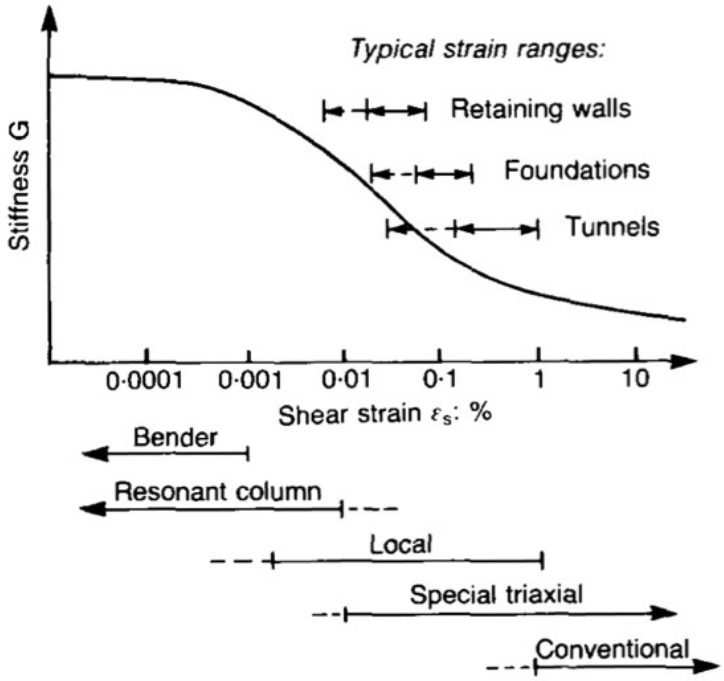

Figure 3.2: Application of different tests to measure soil stiffness and strain ranges for different structures (Mair et al. (1993))

For very small strains, soil is often considered an elastic material. This means that soils have a constant stiffness in this strain range, often referred to as initial stiffness G_0 or maximum stiffness G_{max}. In this thesis, G_0 will be used. Figure 3.3 shows this definition. Another important parameter with regards to small-strain stiffness is the reference shear strain $\gamma_{0.7}$. Hardin and Drnevich (1972b) used a reference shear strain to develop the hyperbolic stiffness reduction law. This has been modified throughout literature and is here defined as the shear strain level at which the stiffness is reduced to 70 % of its initial value. Figure 3.4 shows this definition.

3.1.2 Dependencies of Small-Strain Stiffness

As previously mentioned, soil stiffness varies with applied strain. However, other parameters are also of importance with regards to small-strain stiffness. In 1972 Hardin and Drnevich (1972b) presented a study of different parameters and their effect on small-strain stiffness. The table was later modified by Benz (2006) and the results can be seen in table 3.1. In table

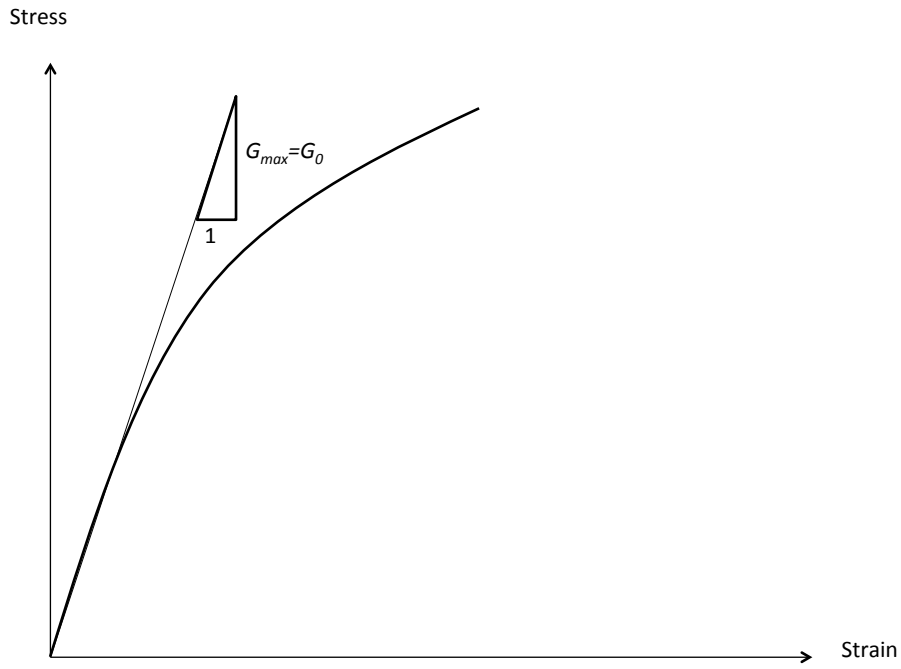

Figure 3.3: Definition of initial stiffness G_0

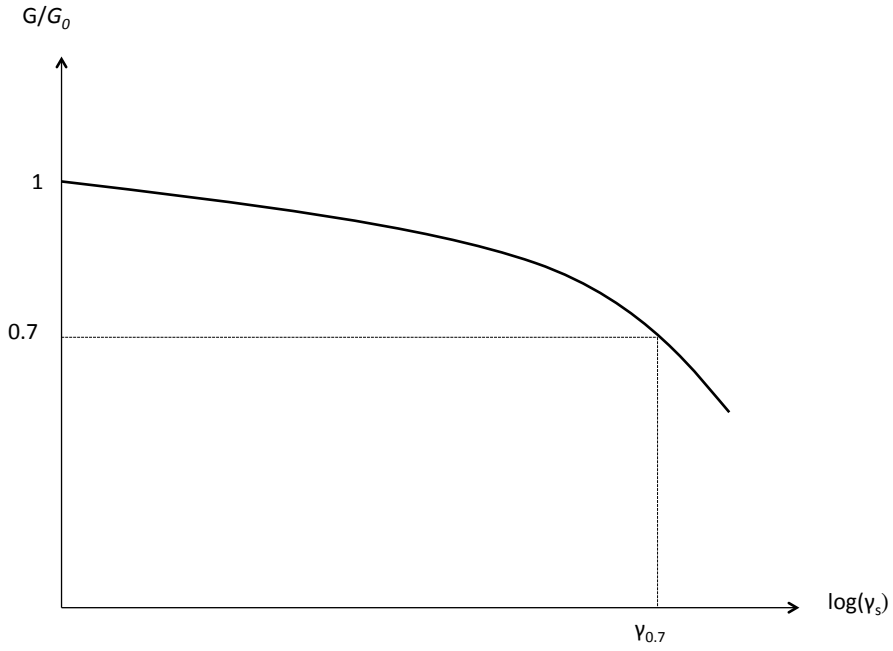

Figure 3.4: Definition of $\gamma_{0.7}$

Parameter	Importance to			
	G_0		$\gamma_{0.7}$	
	Sands	Cohesive Soils	Sands	Cohesive Soils
Strain amplitude	V	V	V	V
Confining stress	V	V	V	V
Void ratio	V	V	R	V
Plasticity index	-	V	-	V
OCR	R	L	R	L
Diagenesis	V	V	R	R
Strain history	R	R	V	V
Strain rate	R	R	R	R
Eff. material strength	L	L	L	L
Grain characteristics	L	L	R	R
Degree of saturation	R	V	L	L
Dilatancy	R	R	R	R

Table 3.1: How different parameters affect small-strain stiffness. (Benz (2006))

3.1 V means very important, L means less important and R means relatively unimportant. Note that table 3.1 refers to clean sands as sands. Considering table 3.1, small-strain stiffness's dependencies cover a variety of parameters. However, strain amplitude and confining stress is considered to be of most importance for this thesis, and will be treated in the next section.

Confining Stress

When Janbu (1967) presented his work for settlement calculations, he used a power law to model the stress dependent feature of soils. The use of power law is also confirmed to hold for the small-strain stiffness range. The relation of Janbu (1967) is similar to the relationship presented by Hardin and Drnevich (1972a):

$$G_0 \propto (p')^m \tag{3.2}$$

where m is an exponent depending on the soil type in question and p' is the mean effective confining stress given by equation (3.3).

$$p' = \frac{\sigma'_1 + \sigma'_2 + \sigma'_3}{3} \tag{3.3}$$

Correlations are also made between G_0 and σ'_1 or σ'_3. However, the principle is still the same. According to Benz (2006) the exponent m is confirmed in

the range of $0.40 \leq m \leq 0.55$ for granular soils. For cohesive soils, m values from 0.5 to 1.0 have been found.

Confining stress relates to void ratio, which is, according to table 3.1, also considered to be a very important parameter with regards to small-strain stiffness. This should be taken into account when comparing m-values for different stress ranges.

The stiffness reduction curve is constructed by use of the reference strain $\gamma_{0.7}$. Darendeli (2001) studied the reference shear strain and found it to correlate well with confining stress of the form:

$$\gamma_{0.7} = (\gamma_{0.7})_{ref}(\frac{p'}{p'_{ref}})^m \tag{3.4}$$

where p'_{ref}=100 kPa is a reference pressure, $(\gamma_{0.7})_{ref}$ is the reference shear strain at $p' = p'_{ref}$ and $m = 0.35$. Benz presented the results of Darendeli (2001) and test data and concluded that the power law works reasonably well also for the threshold shear strain and that the exponent m is usually in the range of 0.35 to 0.65.

Strain Amplitude

In the work of Hardin and Drnevich (1972a), it was presented a set of equations and graphs in order to describe the stress-strain behaviour of soils. The work presented was a hyberbolic stress-strain relation based on the parameters G_0 (or G_{max} as by Hardin and Drnevich (1972a)), G, γ, and γ_r:

$$\frac{G}{G_0} = \frac{1}{1 + \frac{\gamma}{\gamma_r}} \tag{3.5}$$

where $\gamma_r = \frac{\tau_{max}}{G_0}$. However, they found equation (3.5) not to hold without modification, and thus presented a modification of equation (3.5) by defining a hyberbolic strain γ_h.

$$\gamma_h = \frac{\gamma}{\gamma_r}[1 + aexp^{-b\frac{\gamma}{\gamma_r}}] \tag{3.6}$$

where a and b are soil constants which describe the deviation of the stress-strain relation from the hyperbolic curve. This gives the following modification of equation (3.5):

$$\frac{G}{G_0} = \frac{1}{1 + \frac{\gamma}{\gamma_h}} \tag{3.7}$$

with $a = -0.5$ and $b = 0.16$, equation (3.7) describes the modulus of clean, dry sands. Comparing the values of calculated and measured results, the curves and equations were found to fit well with measurements. Throughout literature, modification of equation (3.5) have been presented, and it is widely used due to its simplicity. Also, the well-known geotechnical FEM-software PLAXIS uses a modification of the Hardin and Drnevich (1972a) relation in the Hardening Soil Small model.

3.2 Damping Ratio for Soils

3.2.1 Introduction

Damping ratio is a parameter describing the energy going out of a system. Damping ratio ζ is defined as (Chopra (1995)):

$$\zeta = \frac{c}{c_{cr}} \tag{3.8}$$

where c_{cr} is the critical damping coefficient and c is a measure of the energy dissipated in one cycle. For soils, damping occurs due to friction between grains as well as plastic strains created along discontinuities in the soil. As previously mentioned, soils show a nonlinear stress strain relationship, and the damping ratio is proportional to the area inside the hysteretic loop in figure 3.1. Thus, it is apparent that the damping ratio of soils will be dependent on the strain amplitude induced. Damping ratio for soils is generally difficult to estimate, and a study of the parameters affecting the damping ratio of soils will be presented here in order to get a better idea of what to expect.

3.2.2 Dependencies of Damping Ratio

Many researchers have investigated the dependencies of damping ratio for soils. Hardin and Drnevich (1972b) performed a parameter study, and presented a table of parameters affecting the damping ratio of soils. Where V means very important, L means less important, R means relatively unimportant and U means relative importance was not known at the time. Later research, as by Seed et al. (1986), concluded that factors such as grain size characteristics, degree of saturation, void ratio, lateral earth pressure coefficient, friction angle and strain history have minor effects on the damping ratio of sands. According to Seed et al. (1986), the main factors affecting the damping ratio are the strain level and the effective confining stress. Figure

Parameter	Importance to Damping ratio ζ	
	Clean Sands	Cohesive Soils
Strain amplitude	V	V
Confining stress	V	V
Void ratio	V	V
Strain history	V	V
Degree of saturation	L	U
Overconsolidation ratio	R	L
Effective strength envelope	L	L
Octahedral shear stress	L	L
Strain rate	R	L
Other time effects	R	L
Grain characteristics	R	R
Dilatancy	U	R
Soil structure	R	R

Table 3.2: How different parameters affect damping. (Hardin and Drnevich (1972b))

3.5 shows the effect of confining stress and strain amplitude on the damping ratio for dry sands.

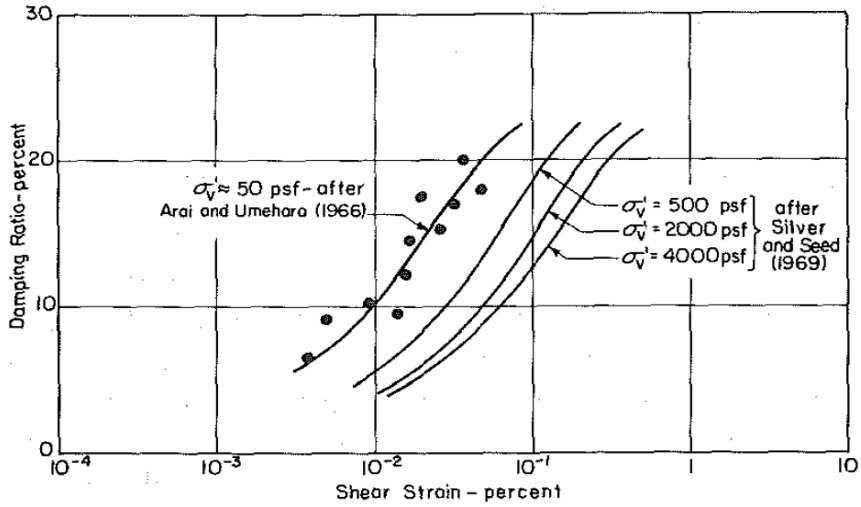

Figure 3.5: Damping ratio for dry sands (Seed et al. (1986))

As can be seen from figure 3.5, the damping ratio of sands decrease significantly when increasing the confining stress. This is less true for higher values of confining stress, where an increased in confining stress plays a lesser role. This means that with an exception of the top few meters of the soil deposit, the parameter of most importance with regards to the damping ratio of sands, is the induced strain amplitude.

Ishibashi and Zhang (1993) investigated the shear moduli and damping properties of both cohesive and granular soils, and found that, although dependencies were found with regards to confining stress and strain amplitude, cohesive soils also show a dependency on plasticity index.

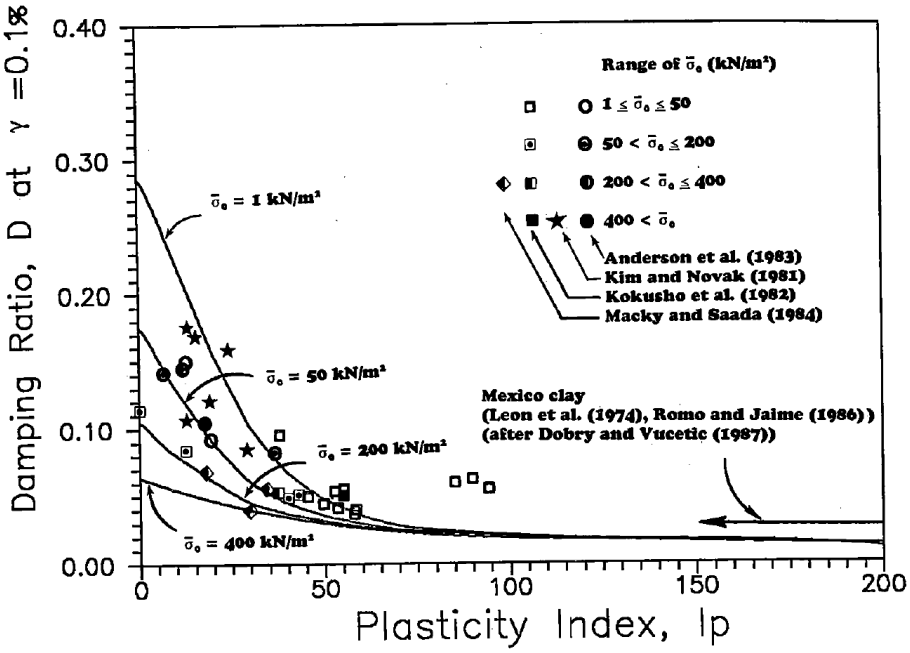

Figure 3.6: Damping ratio for cohesive soils with constant induced strain amplitude (Seed et al. (1986))

As from figure 3.6, cohesive soils also show a tendency of decreasing damping ratio with increased confining stress. The tendency is, however, also for the damping ratio to decrease with increasing plasticity index.

Chapter 4

The Finite Element Method

4.1 Introduction

The basic physical concept of the Finite Element Method is the breakdown or disassembly of a complex mechanical system into simpler, disjoint components called finite elements. The response of an element is characterized by its degrees of freedom. These degrees of freedom are represented as the values of the unknown functions at a set of node points. The element response is defined by algebraic equations constructed from physical or energy arguments. Mathematically, the FEM is characterized as a procedure for obtaining numerical approximations to the solution of boundary value problems over a domain replaced by several sub-domains called finite elements. (Oñate (2013)).

The FEM-software used in this thesis is the FEM-software PLAXIS 3D. This Chapter aims at presenting the basic concepts of FEM and dynamic behaviour in FEM. However, certain sections here are also directly linked to usage of PLAXIS 3D.

4.2 Dynamic behaviour in FEM

Dynamic systems are systems with displacement that develops over time. Its behaviour is governed by a differential equation, here presented on matrix form:

$$[M][\ddot{u}] + [C][\dot{u}] + [K][u] = [P(t)] \tag{4.1}$$

where $[M]$ is the system mass matrix, $[C]$ is the system damping matrix, $[K]$ is the system stiffness matrix, $[u]$ is the nodal displacement vector and $[P(t)]$ is the applied dynamic force vector. The mass matrix is implemented

as a lumped matrix in PLAXIS, while the stiffness matrix is the same as for static calculations. Dynamic systems have a characteristic property called eigenfrequency, defined by equation (4.2) (Chopra (1995)).

$$f = \frac{1}{2\pi}\sqrt{\frac{k}{m}} \tag{4.2}$$

In reality, a structure will be subjected to damping of a certain degree. This is defined by the damping ratio ζ. Damping will also affect the eigenfrequency of a dynamic structure to some extent (Chopra (1995)):

$$f_D = f\sqrt{1-\zeta^2} \tag{4.3}$$

The damping matrix is needed in order to evaluate linear systems with non-classical damping and for analysis of nonlinear structures. For lightly damped systems it is possible to determine the damping properties by using logarithmic decrement as by Chopra (1995):

$$\zeta = \frac{1}{2\pi j} ln \frac{u_i}{u_{i+j}} or \zeta = \frac{1}{2\pi j} ln \frac{\ddot{u}_i}{\ddot{u}_{i+j}} \tag{4.4}$$

The damping ratio for the nth mode of a dynamical system described by Rayleigh damping is on the form:

$$\zeta_n = \frac{\alpha_R}{2\omega_n} + \frac{\beta_R \omega_n}{2} \tag{4.5}$$

where α_R and β_R are coefficients that can be determined using the following set of equations:

$$\alpha_R = \zeta \frac{2\omega_i \omega_j}{\omega_i + \omega_j}, \beta_R = \zeta \frac{2}{\omega_i + \omega_j} \tag{4.6}$$

The damping matrix can then be constructed using equation (4.7):

$$\mathbf{c} = \alpha_R [M] + \beta_R [K] \tag{4.7}$$

Here α_R is a coefficient that relates to mass-proportional damping and β_R relates to stiffness-proportional damping. While stiffness-proportional damping can be interpreted physically as energy dissipation due to deformation in joints or stories in large building, the mass-proportional damping has a less physical interpretation. It could be viewed as air damping, however, this will be very small for most structures.

4.2.1 Discretization

Discretization is a vital part of any finite element calculation. In dynamics, using a too coarse mesh could result in filtering of high frequencies, while a too fine mesh would increase computational time significantly. According to Kramer (1996), the maximum dimension of any element should be limited to $\frac{1}{8}$ to $\frac{1}{5}$ of the shortest wavelength considered in the analysis.

4.2.2 Boundary Conditions

In a dynamic finite-element calculation, it is important to model the geometric and material damping in a correct manner. Wave energy will decrease due to the spreading of energy as well as internal absorption of energy in the material.

Fixed Boundaries

Fixed boundaries are when conditions of zero displacement are introduced at the model boundaries. Care should be taken when introducing such boundaries as they will lead to wave reflections and build up of energy in the system.

Viscous Boundaries

Viscous boundaries consist of viscous dampers at the model boundaries, absorbing the wave energy encountering the model boundaries. As by Kramer (1996), viscous boundaries could be used to simulate a semi-infinite region.

Free Field Boundaries

Free field boundaries consist of a load history and a viscous boundary, and are often used for earthquake analysis.

4.2.3 Time Stepping Procedure

Newmark developed several time-stepping methods based on two basic equations (Chopra (1995)):

$$\dot{u}_{i+1} = \dot{u}_i + [(1-\beta)\Delta t]\ddot{u}_i + (\beta\Delta t)\ddot{u}_{i+1} \tag{4.8}$$

$$u_{i+1} = u_i + (\Delta t)\dot{u}_i + [(0.5-\alpha)(\Delta t)^2]\ddot{u}_i + [\alpha(\Delta t)^2]\ddot{u}_{i+1} \tag{4.9}$$

The parameters α and β define the variation of acceleration over a time step, and also determine the stability and accuracy of the numerical scheme.

The recommended values for α and β are those of the constant average acceleration method with $\alpha = 0.25$ and $\beta = 0.50$. According to Chopra (1995), this introduces an unconditionally stable and accurate scheme. Table 4.1 shows the procedure of Newmark's Integration Scheme.

Phase	Procedure
1	$\ddot{u}_0 = \frac{p_0 - c\dot{u}_0 - ku_0}{m}$ Select Δt. $a_1 = \frac{1}{\alpha(\Delta t)^2}m + \frac{\beta}{\alpha\Delta t}c.$ $a_2 = \frac{1}{\alpha\Delta t}m + (\frac{\beta}{\alpha} - 1)c.$ $a_3 = (\frac{1}{2\alpha} - 1)m + \Delta t(\frac{\beta}{2\alpha} - 1)c.$ $\widehat{k} = k + a_1$
2	$\widehat{p}_{i+1} = p_{i+1} + a_1 u_i + a_2 \dot{u}_i + a_3 \ddot{u}_i.$ $u_{i+1} = \frac{\widehat{p}_{i+1}}{\widehat{k}}.$ $\dot{u}_{i+1} = \frac{\beta}{\alpha\Delta t}(u_{i+1} - u_i) + (1 - \frac{\beta}{\alpha})\dot{u}_i + \Delta t(1 - \frac{\gamma}{2\beta})\ddot{u}_i.$ $\ddot{u}_{i+1} = \frac{1}{\alpha(\Delta t)^2}(u_{i+1} - u_i) - \frac{1}{\alpha\Delta t}\dot{u}_i - (\frac{1}{2\alpha} - 1)\ddot{u}_i.$
3	Increase index and repeat time stepping procedure.

Table 4.1: Calculation procedure for Newmark's integration scheme (Chopra (1995))

Using Newmark's integration scheme, displacements, velocities and accelerations can be determined at the end of each time step.

Dynamic Time Step

The FEM-software PLAXIS automatically chooses a time step based on the chosen dynamic calculation time t, the number of dynamic substeps n_D and the maximum number of steps m_D according to equation (4.10):

$$\delta t = \frac{t}{m n_D} \tag{4.10}$$

Using the default parameters for α and β, the integration scheme is unconditionally stable. According to Brinkgreve et al. (2013c), however, the time step in Newmark's scheme is subject to some limitations. A too large time step, will cause an unreliable and inaccurate solution. The critical time step depends on the maximum frequency and the dimensions of the finite element mesh. For a single element, the critical time step is given by the

following equation (Pal (1998)):

$$\Delta t_{critical} = \frac{l_e}{\alpha_e \sqrt{\frac{E(1-\nu)}{\rho(1+\nu)(1-2\nu)}} \sqrt{1 + \frac{B^4}{4S^2} - \frac{B^2}{2S}[1 + \frac{1-2\nu}{4}\frac{2S}{B^2}]}} \tag{4.11}$$

where B is the largest dimension of the finite element, S is the surface area of the finite element, the first root term is the compression wave velocity, l_e is the average element length and α_e is a factor depending on the element type. This time step is chosen to ensure that a wave during a single step does not move a distance larger than the minimum dimension of an element.

4.3 Material Models

To describe the behaviour of soils during stressing, a constitutive model must be formulated. A constitutive model or equation is the relation between two physical quantities, here stress and strain. The simplest constitutive model relating stress and strain is the linear elastic Hooke's law.

In this thesis, the linear elastic soil model will be used as well as the Hardening Soil Small model. The Hardening Soil Small model is characterized as an advanced soil model. In order to fully understand how the Hardening Soil Small model works, the basic principles of elastoplasticity will be presented. The Hardening Soil Small model is based on the Hardening Soil and Duncan-Chang model, and therefore the basic concepts of these models will also be explained.

4.3.1 Linear Elastic Model

A linear elastic relation between stress and strain is often considered insufficient to calculate deformations of soils. However, for certain problems where soils are assumed to operate in the very small-strain range, it can be used. The linear elastic material model behaves in the same manner as the well-known linear elastic perfectly plastic Mohr-Coulomb, but does not create plastic strains. The relation between stress and strain is given by Hooke's law:

$$\sigma = \epsilon E \tag{4.12}$$

An advantage of the linear elastic material model compared to the Mohr-Coulomb linear elastic perfectly plastic is that it enables better control over the model damping, seeing as Mohr-Coulomb will introduce damping for plastic strains (Brinkgreve et al. (2013c)).

4.3.2 Elastoplasticity

Many of the material models used in the FEM-software PLAXIS are based on elastoplasticity, and therefore the basic concepts of elastoplasticity will be presented here. Elastic deformation is induced by the deformation of the material particles which returns to their initial state when stress is removed. For soils, the elastic range is relatively small. When the stress reaches the yield stress, the particles slip among each other and do not return to their initial state although stress is removed. This is called plastic deformation and the stress - strain relation observed in the elastic range, no longer holds. Thus, the constitutive relation between stress and strain must be formulated as a relation between the stress rate and the strain rate. The decomposition of deformation into elastic and plastic deformations is the basic concept of elastoplasticity (Hashiguchi (2009)).

To implement an elastoplastic material into a FEM software, three rules controlling plastic strains must be formulated:

- Yield criterion: This will determine whether the strains are elastic or plastic. The simplest example is the Mohr-Coulomb failure criterion in the Mohr-Coulomb linear elastic perfectly plastic model.
- Flow rule: This describe how the plastic deformation will look like. There are two types of plastic flow: Associated and non-associated. Associated plastic flow means an attempt to expand the yield surface will give plastic strains as a reaction to the plastifying component of the stress increment which induced the plastic strains. Non-associated plastic flow means the flow is perpendicular to a plastic potential surface.
- Hardening rule: This describes how large the plastic strains will be.

4.3.3 The Duncan-Chang Model

In order to fully understand advanced soil models such as Hardening Soil (HS) and Hardening Soil Small (HSS), one must also consider the Duncan-Chang model. When Duncan and Chang (1970) presented their work on the stress-strain behaviour of soils, the aim was to present a stress-strain relationship which takes into account the nonlinear, stress-dependent and inelastic behaviour of soils. Previous research on the subject (Kondner (1963a) and Kondner (1963b)) plotted test data in a stress-strain diagram normalized with regards to $\sigma_1 - \sigma_3$ to find the best fit between a hyperbola and the test data. When doing so, they found that the asymptotic value of

$\sigma_1 - \sigma_3$ is larger than the strength of the soil by a small amount. To account for this, a factor R_f was introduced as by equation (4.13)

$$(\sigma_1 - \sigma_3)_f = R_f(\sigma_1 - \sigma_3)_{ult} \tag{4.13}$$

where $(\sigma_1 - \sigma_3)_f$ is the soil strength and $(\sigma_1 - \sigma_3)_{ult}$ is the asymptotic value. Thus, the final stress-strain relationship presented in Kondner (1963a) and Kondner (1963b), which was an important part of the Duncan-Chang model, was:

$$(\sigma_1 - \sigma_3) = \frac{\epsilon}{\frac{1}{E_i} + \frac{\epsilon R_f}{(\sigma_1 - \sigma_3)_f}} \tag{4.14}$$

which was found to be a convenient and useful way of representing the nonlinearity of soil with regards to stress-strain behaviour. However, soil stiffness was also believed to be stress-dependent, and Duncan and Chang (1970) presented an expression for the tangent modulus E_t for any stress condition on the form:

$$E_t = [1 - \frac{R_f(1 - sin(\phi))(\sigma_1 - \sigma_3)}{2ccos(\phi) + 2\sigma_3 sin(\phi)}]^2 K p_a (\frac{\sigma_3}{p_a})^m \tag{4.15}$$

This expression presents a very important part of the stress-strain relationship presented by Duncan and Chang (1970) and depends on the five soil parameters c, ϕ, R_f, m and K with K being the modulus number as by Janbu (1967). All these parameters can be determined from laboratory tests. To study the usefulness of equation (4.15), a number of tests were performed to develop techniques for evaluating the parameters in equation (4.15). Duncan and Chang (1970) also studied the unloading-reloading characteristics of soil and concluded that "it seems reasonable to believe that the stress-strain behaviour of soil on unloading and reloading may be approximated with a high degree of accuracy as being linear and elastic." For unloading-reloading stiffness, the following expression is used by Duncan and Chang (1970):

$$E_{ur} = K_{ur} p_a (\frac{\sigma_3}{p_a})^m \tag{4.16}$$

where E_{ur} is the unloading-reloading stiffness and K_{ur} is the modulus number. For practical purposes m is the same as in equation (4.15).

This stress-strain relationship can be used for incremental analysis of nonlinear behaviour. Dividing the loading into a number of increments and assuming the soil to behave linearly within each increment, enables the tangent modulus and strains to be calculated for each step. The incremental strain relate to the stress increment by Hooke's law. Using this constitutive

relationship, the relation was compared to triaxial test data and concluded to be sufficiently accurate. The stress-strain relationship presented by Duncan and Chang (1970) includes six parameters: c, ϕ, K, K_{ur}, R_f and m. Those can all be determined by triaxial or plane strain compression tests involving primary loading and unloading reloading. The material model of Duncan and Chang (1970) incorporates three very important characteristic of soils, namely nonlinearity, stress-dependency and inelasticity. Therefore it can be said to provide a simple technique to interpret results from laboratory tests for the use in finite element stress analysis of soil.

4.3.4 The Hardening Soil Model

The Duncan-Chang model was characterized by Schanz et al. (1999) as a pseudo-elastic (hypo-elastic) model since nonlinearity is achieved by a varying Young's modulus. The disadvantages of this model is, however, that a purely hypo-elastic model can not consistently distinguish between loading and unloading. In addition, it is not suited for collapse load computations in the fully plastic range. These restrictions are overcome in the Hardening Soil model by formulating a model in an elastoplastic framework. Hardening Soil supersedes Duncan-Chang by three measures (Schanz et al. (1999)):

- Using theory of plasticity rather than elasticity.
- Including soil dilatancy, often denoted ψ.
- Introducing a yield cap.

In contrast to the linear elastic perfectly plastic Mohr-Coulomb model, the yield surface in Hardening Soil is not fixed in principle stress space but is allowed to expand due to hardening. A special feature of the Hardening Soil model is that there exist both shear hardening and compression hardening. Shear hardening is used to model irreversible strains due to primary deviatoric loading. Compression hardening is used to model irreversible plastic strains due to primary compression in oedometer and isotropic loading. Figure 4.1 shows the concepts of shear and compression hardening. When the elastic region is expanded due to a plastifying stress increment, there will be an expansion of the elastic region as well as plastic deformations governed by either by E_{50}, E_{oed} or a combination of the two.

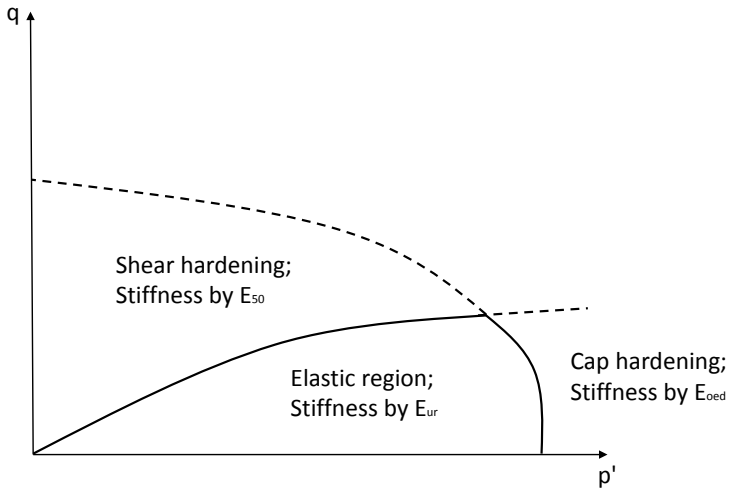

Figure 4.1: Concept of shear and compression hardening. Modified after Brinkgreve et al. (2013a)

Seeing as the Hardening Soil model was verified by using triaxial test data, restrictions are in the following made to the case of triaxial loading with $\sigma_2' = \sigma_3'$. Hardening Soil also uses the hyperbolic stress-strain relationship presented in Duncan and Chang (1970). In the case of primary deviatoric loading, soil stiffness is decreasing and irreversible plastic strains develop. Schanz et al. (1999) found the yield curves for standard drained triaxial tests to be described by:

$$\epsilon = \frac{q_a}{2E_{50}} \frac{(\sigma_1 - \sigma_3}{q_a - (\sigma_1 - \sigma_3)} \tag{4.17}$$

for $q < q_f$ where q_f is the ultimate deviatoric stress from the Mohr-Coulomb failure criterion and q_a is the asymptotic value:

$$q_f = \frac{6sin(\phi_p)}{3 - sin\phi_p}(p + ccot(\phi_p)) \tag{4.18}$$

$$q_a = \frac{q_f}{R_f} \tag{4.19}$$

For $q = q_f$, the failure criterion is reached and plastic yielding occurs, which is one of the advantages of the Hardening Soil model over the Duncan-Chang model. R_f is a value smaller than 1, and is often set to 0.9 by default. Stress-strain for primary loading is nonlinear. Schanz et al. (1999) used E_{50} as a

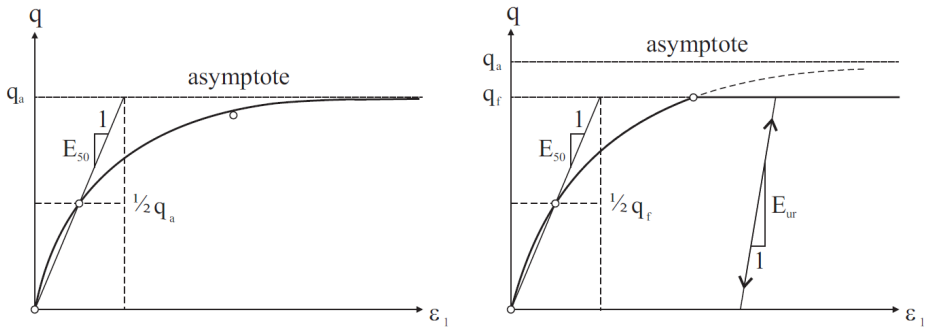

Figure 4.2: Hyperbolic stress-strain relation as by Kondner (1963a) (left) and as used in the HS model (right) (Benz (2006))

tangent modulus and introduced a reference modulus E_{50}^{ref} corresponding to a reference stress σ^{ref}.

$$E_{50} = E_{50}^{ref}(\frac{\sigma_3 + ccot(\phi_p)}{\sigma^{ref} + ccot(\phi_p)})^m \tag{4.20}$$

where m is a parameter controlling how stress dependent the soil is. E_{50}^{ref} is determined from a triaxial stress-strain curve for a mobilization of $0.5q_f$. Seeing as unloading-reloading is considered elastic and known to show a higher stiffness, another modulus is defined for this feature:

$$E_{ur} = E_{ur}^{ref}(\frac{\sigma_3 + ccot(\phi_p)}{\sigma^{ref} + ccot(\phi_p)})^m \tag{4.21}$$

where E_{ur}^{ref} is the reference Young's modulus for unloading and reloading. The hyperbolic stress-strain curve used in the Hardening Soil model can be seen in figure 5.2. The elastic stress components are calculated using Hooke's law, E_{ur} and an unloading-reloading Poisson's ratio ν_{ur}. For drained triaxial stress paths with $\sigma_2 = \sigma_3 = constant$:

$$\epsilon_1^e = \frac{q}{E_{ur}} \tag{4.22}$$

$$\epsilon_2^e = \epsilon_3^e = \nu_{ur}\frac{q}{E_{ur}} \tag{4.23}$$

Note that these are strains that develop during deviatoric loading. Strains developed during consolidation is not considered. Schanz et al. (1999) defined two yield surfaces for the triaxial case with the plastic shear strain γ^p

as a parameter for deviatoric hardening:

$$f_{12} = \frac{q}{E_{50}} \frac{(\sigma_1 - \sigma_2)}{q_a - (\sigma_1 - \sigma_2)} - \frac{2(\sigma_1 - \sigma_2)}{E_{ur}} - \gamma^p \tag{4.24}$$

$$f_{13} = \frac{q}{E_{50}} \frac{(\sigma_1 - \sigma_3)}{q_a - (\sigma_1 - \sigma_3)} - \frac{2(\sigma_1 - \sigma_3)}{E_{ur}} - \gamma^p \tag{4.25}$$

where γ^p is defined as:

$$\gamma^p = \epsilon_1^p - \epsilon_2^p - \epsilon_3^p = 2\epsilon_1^p - \epsilon_v^p \approx 2\epsilon_1^p \tag{4.26}$$

For stiff soils, plastic volumetric strain tends to be small compared to axial strain and thus equation (4.26) holds. For a given value of γ^p, the yield condition can be visualized in a p'-q plot as a yield locus for $f_{12} = f_{13} = 0$.

All plasticity models includes a flow rule, describing a relationship between the rates of plastic strain. For the Hardening Soil model, it is described by the relationship between $\dot{\epsilon}_v^p$ and $\dot{\gamma}^p$:

$$\dot{\epsilon}_v^p = sin(\psi_m)\dot{\gamma}^p \tag{4.27}$$

where the mobilized dilatancy angle ψ_m controls the relationship between the plastic strain rates and is given by:

$$sin(\psi_m) = \frac{sin(\phi_m) - sin(\phi_{cv})}{1 - sin(\phi_m)sin(\phi_{cv})} \tag{4.28}$$

where ϕ_{cv} is the critical state friction angle and ϕ_m is the mobilized friction angle dependent on the stress level and strength of the soil:

$$sin(\phi_m) = \frac{\sigma_1 - \sigma_3}{\sigma_1 + \sigma_3 - 2ccot(\phi_p)} \tag{4.29}$$

where ϕ_p is the friction angle at failure and c is cohesion. Thus, equation (4.29) can be re-written as:

$$sin(\psi_{cv}) = \frac{sin(\phi_p) - sin(\psi_p)}{1 - sin(\phi_p)sin(\psi_p)} \tag{4.30}$$

which enables the critical state dilatancy angle to be calculated from the failure angles ϕ_p and ψ_p.

A second cap yield surface is introduced to close the elastic region in the direction of *p'*. The plastic strains at this yield surface is controlled by the oedometer stiffness E_{oed}.

$$E_{oed} = E_{oed}^{ref} \frac{ccos(\phi_p) + \sigma_1' sin(\phi_p)}{ccos(\phi_p) + p^{ref} sin(\phi_p)} \tag{4.31}$$

Note that compression is positive in equation (4.20), (4.21) and (4.31). The cap yield surface is shown in figure 4.1 and is defined as:

$$f_c = \frac{q^2}{M^2} + (p + a)^2 - (p_c + a)^2 \tag{4.32}$$

where $p = \sigma_1 + \sigma_2 + \sigma_3$, p_c is the pre-consolidation stress and M is an auxiliary parameter that relates to K_0^{NC}. The deviatoric stress measure q is given as:

$$q = \sigma_1 + (\alpha - 1)\sigma_2 - \alpha\sigma_3 \tag{4.33}$$

With $\alpha = \frac{3+sin\phi}{3-sin\phi}$. For yielding on the cap surface, associated flow is assumed, meaning the plastic potential is the same as the yield function $g_c = f_c$. The magnitude of the yield cap is governed by the isotropic pre-consolidation stress p_c.

In 3-dimensional stress space, the Hardening Soil model have the same hexagonal shape of the Mohr-Coulomb model, and the shear yield locus in figure 4.1 is allowed to expand up to the Mohr-Coulomb ultimate failure surface. The cap yield surface will expand as a function of the pre-consolidation stress, and an increase in pre-consolidation stress will increase the elastic region.

4.3.5 The Hardening Soil Small Model

The Hardening Soil Small model is believed to be well-suited for numerical modelling of the problem considered in this thesis. As previously mentioned, small-strain stiffness is a very important feature with regards to the deformation of dynamic structures. The Hardening Soil Small model takes the very small-strain stiffness G_0 and its decay with strain amplitude into account by implementing the hyperbolic law of Hardin and Drnevich (1972a). When Benz (2006) formulated the HSS model, it was formulated as an small-strain overlay model to the Hardening Soil model. This means it used the basics of the Hardening Soil model, adding small-strain stiffness to the model.

Small-strain stiffness decay can be related to the loss of intermolecular and surface forces in the soil skeleton. Once the direction of loading is reversed, the stiffness regains its maximum value which is in the order of the initial soil stiffness. Benz (2006) proposed a strain history dependent multi-axial extension of the Hardin-Drnevich relation:

$$\gamma_{hist} = \sqrt{3}\frac{||\Delta eH||}{||\Delta e||} \tag{4.34}$$

where Δe is the actual deviatoric strain increment, $||...||$ denotes the Hilbert-Schmidt norm and H is a symmetric tensor that represents the deviatoric strain history of the material. Whenever a strain reversal is detected, the tensor H is partially or fully reset before the actual strain increment Δe is added. Note that the scalar valued shear strain is defined as:

$$\gamma = \frac{3}{2}\epsilon_q \tag{4.35}$$

where ϵ_q is the second deviatoric strain invariant. Within the HS Small model, the stress - strain relationship can be simply formulated from the secant shear modulus:

$$\tau = G_s\gamma = \frac{G_0\gamma}{1 + 0.385\frac{\gamma_{hist}}{\gamma_{0.7}}} \tag{4.36}$$

In numerical applications, the secant modulus in equation (4.36) must be converted to a tangent modulus. Taking the derivative with respect to the shear strain gives the tangent shear modulus:

$$G_t = \frac{G_0}{(1 + 0.385\frac{\gamma_{hist}}{\gamma_{0.7}})^2} \tag{4.37}$$

In the HS and HSS model, stiffness degradation due to plastic straining is simulated with strain hardening. To avoid too low stiffness, the small-strain stiffness curve is bounded by a certain lower limit, determined by conventional laboratory tests. This limit is defined by a cut-off shear strain γ_c depending on G_{ur} and G_0 (Benz (2006)):

$$\gamma_c = \frac{\gamma_{0.7}}{a}(\sqrt{\frac{G_0}{G_{ur}}} - 1) \tag{4.38}$$

This results in the stiffness behaviour shown in figure 4.3.

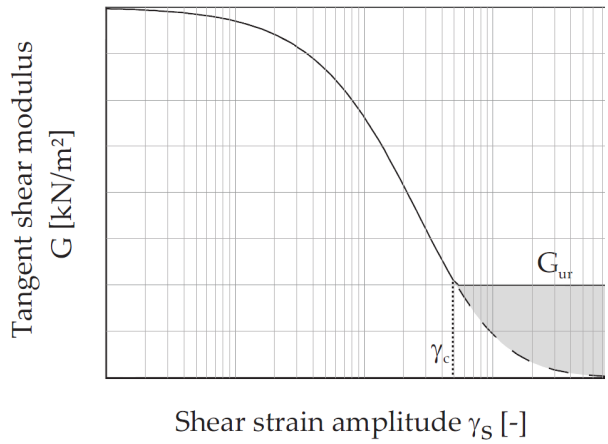

Figure 4.3: Stiffness reduction curve as implemented in the Hardening Soil Small model (Brinkgreve et al. (2013a))

When the calculated strains are larger than the cut-off shear strain, the unloading-reloading stiffness will be used. Otherwise, the tangent modulus in equation (4.37) will be used.

Another advantage of the HSS model is its ability to capture the hysteretic damping characteristic of soils. Upon shearing, the soil will show typical hysteretic behaviour starting with an initial stiffness G_0, which is then reduced during shearing until it restores its full value upon load reversal. The damping is proportional to the area inside the hysteretic loop and will thus increase with increased shear amplitude. The damping ratio is, however, restricted by the cut-off shear strain defined above, and will not increase further once this value is reached.

Part II

Experimental Programme

Chapter 5

Laboratory Investigations

Dynamic testing of a steel pipe installed in dry sand has been carried out in the Foundations Laboratory at NTNU. Preparations and test-setup was performed during the spring of 2014 as a part of a project thesis (Hetland (2014)). Complementary setup and testing has been performed as a part of this master thesis. The aim was to determine important characteristics of the model pile, as well as important material properties relevant to the dynamic behaviour of the model pile. In this chapter, a description of the laboratory will be presented as well as the material properties of the sand found by previous investigations. A detailed description of laboratory setup, instrumentation and post-processing of the measured data is given in Hetland (2014). Shear wave measurements were used to establish the shear stiffness profile, and strain gage measurements were used to determine the system's first eigenfrequency.

5.1 Description of Laboratory

The Foundations Laboratory consists of a 4x4 m wide sand bin with concrete walls. To resemble the monopile foundation of an offshore wind turbine, a pile was installed in the sand bin with total length of 6 m and embedded length of 1.4 m. The pile was pre-installed and the sand rained in afterwards, making it a "wished in place" installation to avoid installation effects. The model was made in scale 1:20, resembling a monopile with 28 m embedded length. Figure 5.1 shows the sand bin with the pile installed and corresponding measurements. To enable measurements with different levels of overburden pressure, a membrane was installed on top of the sand. An effort was made to make the sand bin as airtight as possible. Then a pump was installed into an existing drainage pipe at the bottom of the tank. The

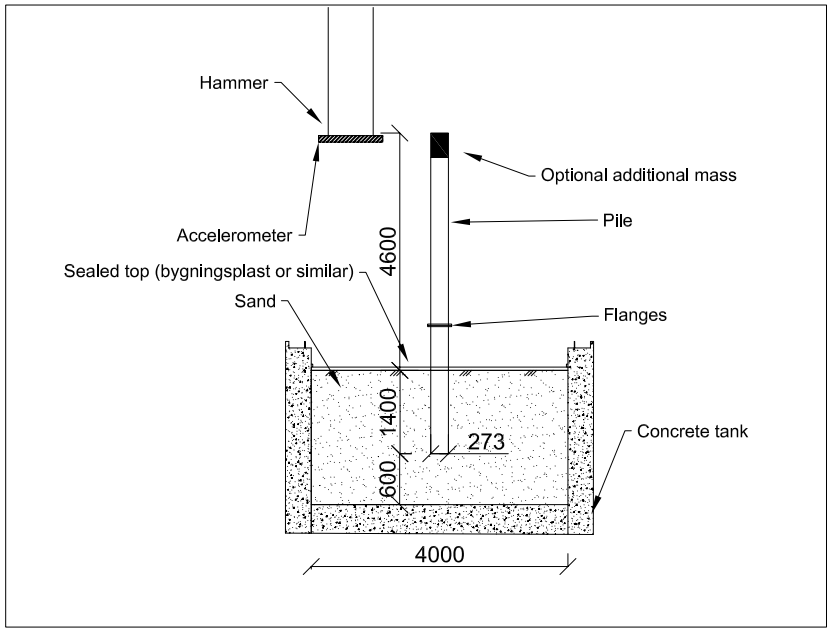

Figure 5.1: Vertical section of the pile installed in the sand with corresponding measurements

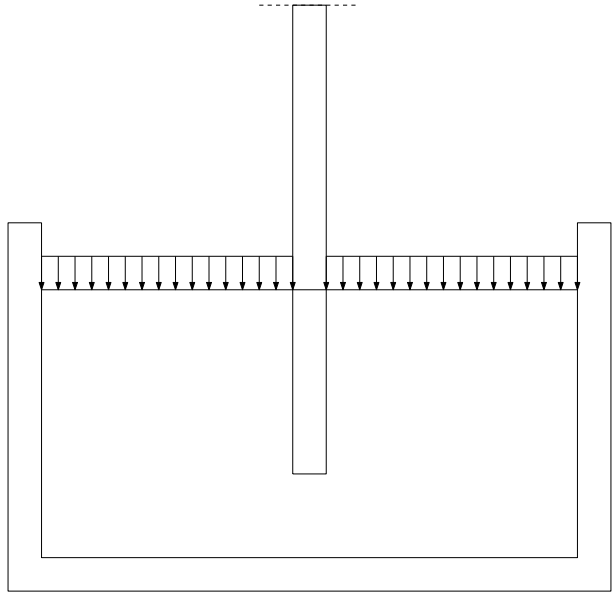

Figure 5.2: Principle sketch of how the suction in the tank was believed to work

suction from the pump was believed to pull the membrane down towards the sand, acting as an overburden pressure. See Appendix C for a principle sketch including the installed pump. The applied overburden pressure was varied by adjusting a valve, and therefore the obtained values of overburden pressure may seem random for some measurements. Figure 5.2 shows a sketch of how the suction was believed to act, pulling the membrane down to form an overburden pressure on the sand.

The hammer in figure 5.1 was used to introduce an impact force to the top of the pile. The hammer was pulled back a distance of 0.13 m for each measurement series, and the acceleration of the hammer was measured to approximate the magnitude of the force. The impact force will excite the pile in all its modes.

5.2 Description of Material Parameters

The sand used in these experiments was from a glazifluvial deposit in Hokksund, Norway. The sand was spread into the tank using 16 mm diameter nozzles, creating uniform conditions in the tank. The material properties of the Hokksund sand have been investigated through numerous experiments

over the years (Moen (1978) and Lieng (1984)), while the Poisson's ratio for small-strains is an assumed value. The S- and P-wave velocities as well as the stress exponent m were measured in the project work performed in the spring of 2014 (Hetland (2014)). Table 5.1 shows the material properties of the sand for the conditions of these tests.

Parameter	Symbol	Unit	Value
Friction angle	ϕ	[°]	38
Porosity	n	[%]	39.9
Min. porosity	n_{min}	[%]	36.4
Max. porosity	n_{max}	[%]	48.8
Rel. density	D_r	[%]	76
Weight density	Υ	$[kN/m^3]$	16.0
Specific density	Υ_s	$[kN/m^3]$	27.1
Poisson's ratio	ν	[-]	0.35
Poisson's ratio (small strains)	ν_{ur}	[-]	0.2
S-wave velocity	V_S	[m/s]	120-200 m/s
P-wave velocity	V_P	[m/s]	200-300
Stress exponent	m	[-]	0.48

Table 5.1: Material properties of Hokksund sand (Moen (1978) and Lieng (1984))

The pile used was a steel pipe, installed with an embedded length of 1.4 m and total length of 6 m. At the top of the pile there was a flange with total mass of 9 kg and 0.6 m above the sand surface there was flange connection with a total weight of 29 kg. A summary of dimensions and material properties of the pile can be seen in table 5.2.

Parameter	Symbol	Unit	Value
Diameter	D	[m]	0.273
Total length	L	[m]	6000
Embedded length	$L_{embedded}$	[m]	1.4
Thickness	t_{pile}	[mm]	4
Distributed mass	m_{pile}	[kg/m]	26.5
Density	ρ_{steel}	$[kg/m^3]$	7850
Flange mass	m_{flange}	[kg]	29
Top flange	m_{top}	[kg]	9
Hammer mass	m_{hammer}	[kg]	15.92
Bending stiffness	EI	$[kNm^2]$	6422

Table 5.2: Material properties of steel pipe

5.3 Pile Instrumentation

The pile was instrumented with strain gages to enable dynamic measurements of the pile response during testing. Additionally, an accelerometer was attached to the hammer to measure the impulse force introduced. For the scope of this thesis, the focus is on back-calculations, and for further details on installation and calibration of measurement equipment it is referred to Hetland (2014).

5.4 Shear Wave Measurements

To establish the stiffness profile of the sand, shear wave measurements were performed. The measurements were performed using two accelerometers placed in the sand at 1.0 m depth. The results were interpreted manually by finding the arrival times of the S-waves at the points where the accelerometers were located. For more details on the procedure and result interpretation it is referred to Hetland (2014). Measurements were performed for a wider range of overburden pressure than in Hetland (2014), allowing for more accurate determination of the stiffness profile. A new pump was installed, increasing the maximum overburden pressure achieved from around 20 kPa to around 50 kPa. This allowed for shear wave measurements for overburden pressure of 0 - 10 - 20 - 30 - 41 and 50 kPa, giving an effective vertical stress of 16 - 26 - 36 - 46 - 57 and 66 at the depth of measurement respectively. The shear wave velocities were found for five measurement series at each effective stress level using the same procedure,

Effective stress [kPa]	V_S [m/s]
16	124
26	145
36	156
46	162
57	171
66	177

Table 5.3: Shear wave velocities at different levels of effective stress

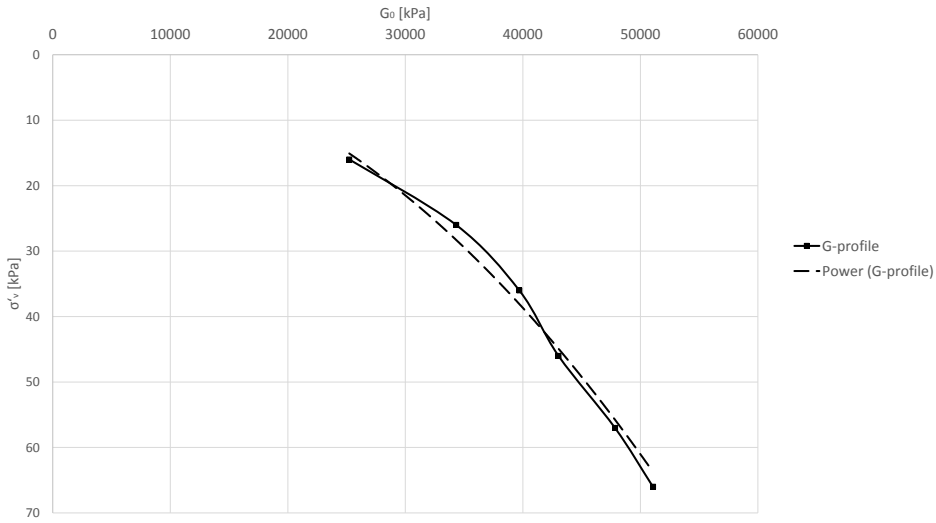

Figure 5.3: G_0-profile from shear wave measurements

and the velocities shown in table 5.3 is the average of these. Equation (5.1) was used to calculate the stiffness based on these average velocities.

$$G_0 = \frac{V_S^2}{\rho} \tag{5.1}$$

Shear wave velocities for different values of overburden pressure can be seen in table 5.3 and the resulting stiffness profile is presented in figure 5.3. Stiffness of soils are known to relate to the effective stress level in the soil (Benz (2006)). Different correlations are used in literature. For simplicity, it is here chosen to relate soil stiffness to the effective vertical stress, seeing as this can be found directly without the use of K_0'. The trendline tool in EXCEL was used to find a function describing the G-profile seen in figure

5.3. The equation was found to be:

$$G_0 = 6826(\sigma_v)'^{0.48} \tag{5.2}$$

Using equation (5.2) it is possible to discretize the stiffness in the finite element model, and get a better estimate of the deformation characteristics of the system. Figure 5.3 shows a comparison between the power series and the measurements.

5.4.1 Sources of Error

Interpretation of shear wave measurements was a challenging process. The results gave no clear indication of the arrival time of the shear waves, and there were significant disturbance from P-waves travelling simultaneously through the sand material, as well as some disturbance from surrounding machines.

There were also uncertainties with regards to whether the waves observed were S-waves or Rayleigh waves, seeing as the accelerometers were located at the shallow depth of 1.0 m. However, Rayleigh waves travel at approximately the same velocity as S-waves (Kramer (1996)), and the results should nonetheless give a good approximation of the S-wave velocity.

The curve fitting tool used in EXCEL will also introduce a small error. For practical purposes, however, this error is relatively small. The change in void ratio with overburden pressure was not considered here, and is not necessary seeing as the stress range used to determine m, was approximately the same stress range used in the calculations.

5.5 Strain Gage Measurements

Strain gages have a wide range of application within engineering. In this case it is restricted for determination of what is assumed to be the first eigenfrequency of the system. For more details on instrumentation and calibration of the strain gages, it is referred to Hetland (2014). The response of the system was measured for different levels of overburden pressure. Appendix A shows the time-series obtained for measurements with different overburden pressure. For convenience, the amplitude is given in volts as was measured from the strain gages. This, however, relates linearly to the pile top displacement, and is therefore also correct to use.

Initially, the eigefrequencies were interpreted manually by finding the time difference from one wave top to the next. It was then observed that the eigenfrequency varied slightly within each test series. Therefore, it was

decided to investigate the variation of the eigenfrequency throughout the series. This was performed automatically by using a MATLAB script found in Appendix C. A sampling frequency of 15,000 Hz (15,000 measurements per second) was used. Several sampling frequencies were tested, and a sampling frequency of 15,000 Hz was found to be necessary in order to avoid too large error in the smoothening process. To obtain a smoothened curve for automatic interpretation of measurement results, a lowpass filter was used in MATLAB. The function used is shown in Appendix C and makes use of two built-in MATLAB-functions in order to execute a lowpass filter that removes the frequencies after a given frequency. The function also takes use of a given number of measurement points to establish the smoothened curve, which explains why such a high measurement frequency was chosen. Appendix B shows the smoothened curve compared to an unfiltered time-series.

The filtered time-series enables automatic detection of the wave tops of the time-series, and the eigefrequency was taken as the inverse of the time difference from one wave top to the next. Five measurements were performed for each of the six different values of overburden pressure. The tendency of the eigenfrequency was to increase with time for each measurement series, meaning the eigenfrequency increased with decreasing amplitude. This indicates a varying stiffness with amplitude, as is also expected from soils due to the re-arrangement of grains and loss of intermolecular forces. There was also the tendency of increasing eigenfrequency with increased overburden pressure. This is believed to have been caused by the increased stiffness with effective stress level. Figure 5.4 shows the development of the eigenfrequency with time. The eigenfrequency of the system in question was found to be increasing with time, and this was especially the case for the measurements with no overpressure. This indicates increasing stiffness with decreasing shear strain which is a property of soil tested and confirmed by many scientists. The results also show some scatter which is due to the fact that a small variation in the point that is found as the wave top will cause a slight change in eigenfrequency.

The accuracy of the measurements carried out here was considered to be of order 10^{-1}, and table 5.4 shows the eigenfrequency decided to be representative for the different levels of overburden pressure.

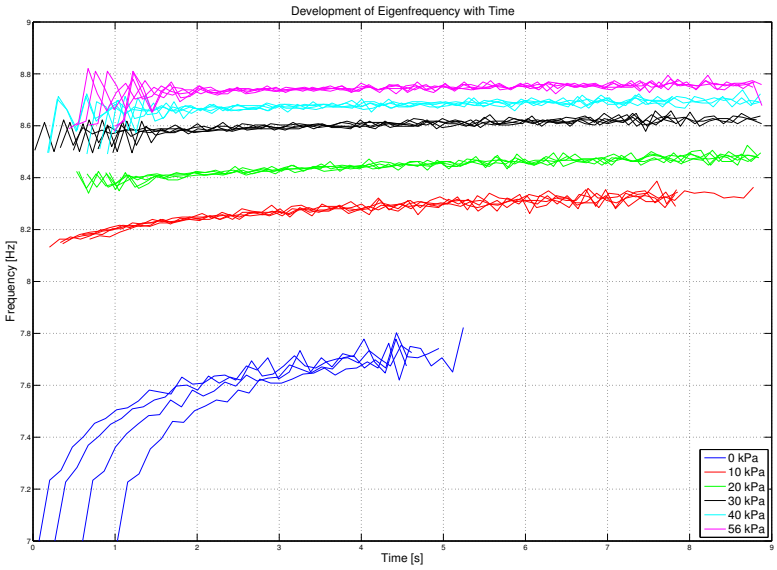

Figure 5.4: Development of eigenfrequency with time for different values of overburden pressure

Overburden Pressure [kPa]	Eigenfrequency [Hz]
0	7.7
10	8.3
20	8.5
30	8.6
40	8.7
56	8.8

Table 5.4: Eigenfrequency for different levels of overburden pressure

Due to the changing values of eigenfrequency with amplitude, the values in table 5.4 were taken as the values after the eigenfrequency had stabilized, where the strain amplitude were considered to be in the very small-strain range.

5.5.1 Sources of Error

Generally, the eigenfrequency of a structure is a unique quantity. Here, though, it was observed to vary with time, which can seem somewhat counter-intuitive. The reason for the varying eigenfrequency is believed to be the soil's varying stiffness with strain amplitude.

The lowpass filter used to modify the measurement results removes frequencies above a given value. This will decease the amplitude by a small amount. However, the frequency of interest is believed to be around 8 Hz, and this was considered to be unaffected by the filtering process.

The time-series have different starting points on the time axis. However, the development with time is what is being considered here. As from figure 5.4, all measurement series show some scatter. This was due to a small variation in what was found to be the wave tops will cause significant change in the value for the eigenfrequency.

5.6 Damping Measurements

Using strain gage measurements, the damping characteristics of the system could be investigated. This was performed by using the method of logarithmic decrement (Chopra (1995)).

$$\zeta = \frac{1}{2\pi} ln(\frac{u_i}{u_{i+1}}) \tag{5.3}$$

The damping ratio was plotted versus time for different levels of overburden pressure and can be seen in figure 5.5. As by Seed et al. (1986), the damping

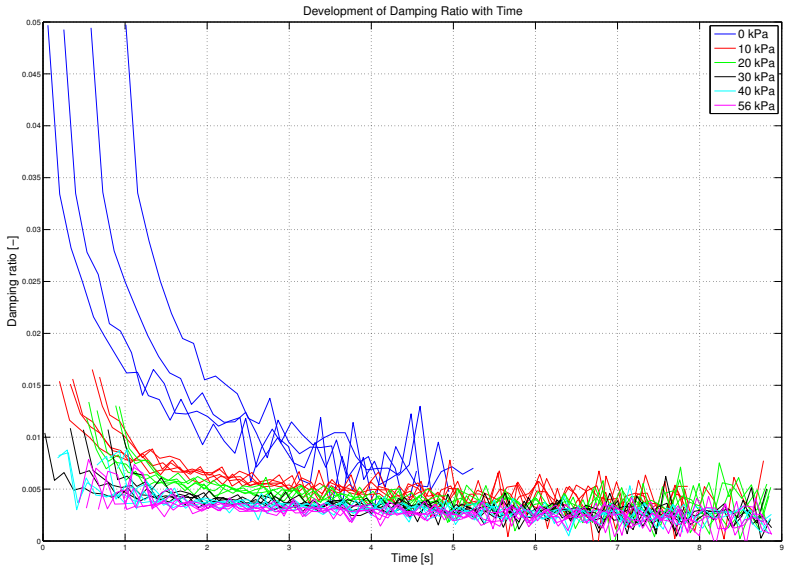

Figure 5.5: Damping ratio versus time for different levels of overburden pressure

ratio varies with amplitude and confining stress. Considering figure 5.5, these characteristics was confirmed for the Hokksund sand as well. The damping ratio was found to be decreasing with increasing confining stress and decreasing amplitude (or shear strain as by Seed et al. (1986)). The decreased damping with increased confining stress could be interpreted as a decreased material damping due to reduced movement and reduced friction between grains. It was also observed that the damping ratio changes less with amplitude as the confining stress is increased, indicating that the most important factor with regards to soil damping is the strain amplitude. This is especially true for deeper soil layers where the higher confining stress will decrease damping. The decreased damping ratio with decreased shear strain amplitude confirms the hysteretic damping characteristics of the Hokksund sand.

Due to the change in damping ratio with time, the damping ratio chosen for back-calculation was the maximum damping ratio in figure 5.5. The determined maximum damping ratio can be seen in table 5.5.

Overburden Pressure [kPa]	Damping ratio [-]
0	0.050
10	0.015
20	0.012
30	0.011
40	0.008
56	0.007

Table 5.5: Maximum damping ratio for different levels of overburden pressure

The results also indicate that the damping for the pile material was very small. As the confining stress was increased, the system damping reduced to values around 0.005. Therefore, the material damping of the pile was considered to be around this value or slightly smaller.

5.6.1 Sources of Error

The values for damping ratio also show some scatter, for the same reason as the eigenfrequency measurements. For practical purposes, however, the scatter was relatively small, and determination of the maximum damping ratio, which was the one tried to obtain in the numerical model, from figure 5.5 was relatively straight-forward.

Note that equation (5.3) relates the damping ratio to a displacement

quantity. However, as previously mentioned, pile top displacement relates linearly to the measured strain, and the damping ratio could therefore be found directly from the measurements.

Chapter 6

Finite Element Model

The deformations of the model pile used in the laboratory testing was back-calculated. This was performed by creating a Finite Element Model in PLAXIS 3D. An effort was made to ensure that the laboratory conditions were modelled in a sufficiently accurate manner. In this chapter the Finite Element Model will be described, as well as discussion of the material properties used.

6.1 Basics of PLAXIS 3D Dynamics

PLAXIS 3D is a three-dimensional finite element program for calculation of deformations and stability for various types of geotechnical problems.

PLAXIS 3D Dynamics is a special feature implemented in the PLAXIS-software which aims at solving the differential equation of dynamic behaviour. Dynamics in PLAXIS 3D is applicable to all soil models as well as to drained and undrained behaviour. The stiffness matrix is constructed as in static calculations. The concepts of dynamic behaviour is the introduction of a mass $[M]$ and damping matrix $[C]$. Constructing the mass matrix, the mass of soil, structures as well as water is taken into account, and the mass matrix in PLAXIS 3D is implemented as a lumped matrix. The damping matrix represents the material damping of the separate materials as well as the geometric damping of the system, and physically describes the energy going out of the system. Damping for soils is caused by friction between grains and irreversible deformations. Assuming elasticity, there will be no material damping. In PLAXIS, Rayleigh damping can then be used (Brinkgreve et al. (2013c)). Theory of plasticity will introduce some damping, and as previously mentioned the HSS model includes hysteretic damping.

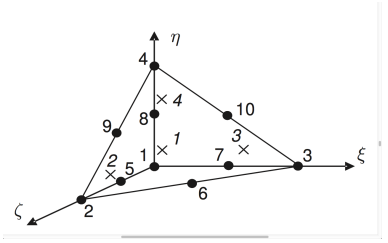

Figure 6.1: 10-noded tetrahedral element used in PLAXIS 3D with corresponding nodes and axes (Brinkgreve et al. (2013c))

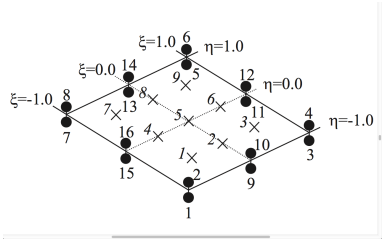

Figure 6.2: 16-node interface element (Brinkgreve et al. (2013c))

6.1.1 Elements Formulation

The 10-noded elements are created in the meshing procedure and provide a second order interpolation of displacements. Figure 6.1 shows such an element with corresponding nodes and axes.

6.1.2 Interface Elements

Interface elements are special elements in the sense that they have pairs of nodes instead of single nodes. This enables differential displacements between the node pairs, and thus uncouples the soil from the structure. In PLAXIS 3D, 12-node interface elements are used. Figure 6.2 shows a 16-node interface element used in 2D. The concept is, however, the same. The material properties of an interface must be specified either as *from adjacent soil* or as *custom*. The roughness of the interaction is modelled by choosing a suitable value for the strength reduction factor R_{inter} between 0 and 1.0, where 0 means smooth and 1.0 means a fully rough surface.

Interfaces have a virtual thickness which is an imaginary dimension used to define the material properties of the interface. Higher thickness gives more elastic deformations. Interfaces should create very little elastic deformations and therefore the virtual thickness should be small. Default value

for virtual thickness factor is 0.1 and the actual thickness is created from the global element size. If the interface is subjected to very large normal stresses it may be reduced, but this could introduce numerical problems. Here, the default value for thickness was used, and the normal interface stress was found to be at a maximum value of around 30 kPa, and will not produce significant deformations.

Corners in stiff structures may lead to high peaks in the stresses and strains. This was solved by introducing additional interface elements inside the soil body. These elements will increase the flexibility of the mesh and thus prevent non-physical stress results. At interface ends, the interface elements are reduced to single nodes. Therefore another interface is introduced at the other side of the structure to introduce a second interface node at the corner points. Interfaces were defined on both sides and underneath the pile with material properties from adjacent soil, meaning $R_{inter} = 1.0$. Also, an additional interface was expanded from the tip of the pile and downwards to avoid stress concentrations at the pile tip. This was created with material properties from adjacent soil also. The interface stresses were checked and no stress concentrations were observed. Appendix F shows an example of the interface stresses which occured in a calculation using the linear elastic material model.

6.2 Model Geometry

The geometry of the FE-model was given by the physical dimensions of the laboratory conditions. In order to reduce computational effort, a half model was created. This was checked against a full model and found to represent the problem correctly. The geometry of the FE-model can be seen in figure 6.3. The boundaries of the Finite Element Model was defined by the points $x = [-2, 2]$ and $y = [0, 2]$. The other model properties used was the default values from PLAXIS.

6.2.1 Soil Volume

To create the soil volume, a single borehole was defined with boundaries $z = [0, -2]$. The conditions were considered to be uniform throughout the soil with regards to soil properties with the exception of soil stiffness, which will be further explained later in this chapter.

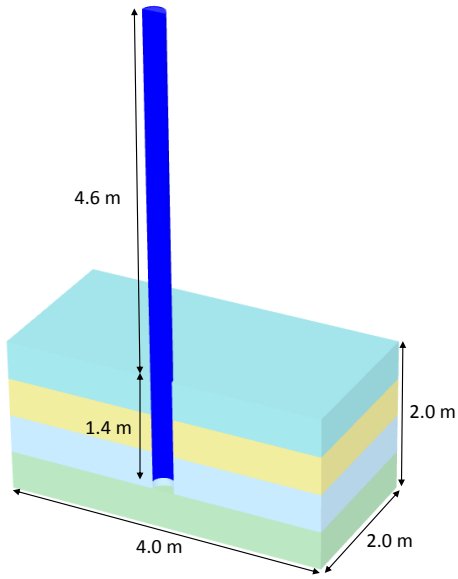

Figure 6.3: Model geometry with corresponding measurements

6.2.2 Pile

The pile was created using the polycurve function, making a half circle with a radius of 0.1365 m, and extruding the half circle from z=[4.6, -1.4]. It was then defined as a plate and material properties were defined according to table 5.2.

The pile also included a top flange of 9 kg and a flange connection of 29 kg. Seeing as this was a half model, only half of the two masses were added to the system. The top flange was modelled as a plate with very high stiffness ($1000 \times E_{steel}$). This reduced ovalization of the steel pipe upon loading and avoided disturbance from other modes. The flange connection was modelled as a plate with very low stiffness ($E_{steel} \times 10^{-6}$) such that its stiffness will not affect the system stiffness. In reality, this was a flange connection, connecting two steel pipes of different lengths, and its stiffness should not contribute to the entire system stiffness.

6.3 Soil Properties

The sand used in the laboratory was from a glazifluvial deposit in Hokksund, Norway. Some material parameters can be found in table 5.1. However,

using more advanced constitutive models, all material parameters can not be found. Thus, some soil parameters were fitted using the Soil Test option in PLAXIS 3D, and some were found using correlations for similar soil types. The soil was defined by a single borehole, consisting of four different layers for the linear elastic model. The borehole was set from 0 to -2 m depth and the ground water head was set to -2 m to ensure the ground water level was below the soil. The soil was modelled using two material models: Linear elastic soil and the Hardening Soil Small model. As previously mentioned, the Hardening Soil Small model includes several features which should make it more applicable to problems of this nature than the linear elastic model. The soil properties used for each model is described next.

6.3.1 Linear Elastic Material Model

The linear elastic material model is a relatively simple model, requiring few input parameters. In order to better estimate the stiffness profile of the sand, four different layers were defined. This is further explained in the next part. However, the general soil and interface properties are defined in table 6.1.

General			Dry sand	Interface
Material model			Linear Elastic	Linear Elastic
Drainage type			Drained	Drained
Parameter	Symbol	Unit	Value	
Weight density	Υ	$[\frac{kN}{m^3}]$	16	16
Lateral stress coeff.	K_0'	[-]	0.38	0.38
Poisson's ratio	ν'	[-]	0.2	0.2
Interface strength			Rigid	Rigid
Strength reduction	R_{inter}	[-]	1.0	1.0

Table 6.1: Material properties of soil and interfaces for linear elastic material model

Soil Stiffness Profiles

The soil stiffness profile is shown to have significant effect with regards to the eigenfrequency of offshore monopile foundations. Using shear wave measurements, it was possible to estimate this quantity for the Hokksund sand. The stiffness profile of sand relates to the effective stress level and follows a power rule as found in Chapter 5. In the linear elastic material model in PLAXIS 3D it is only possible to use linearly increasing stiffness

with depth. This was solved by introducing four layers, and thus making the stiffness profiles piece-wise linear. The E-profiles for different overburden pressures were estimated using equation (5.2) and theory of elasticity, and can be seen in figure 6.4.

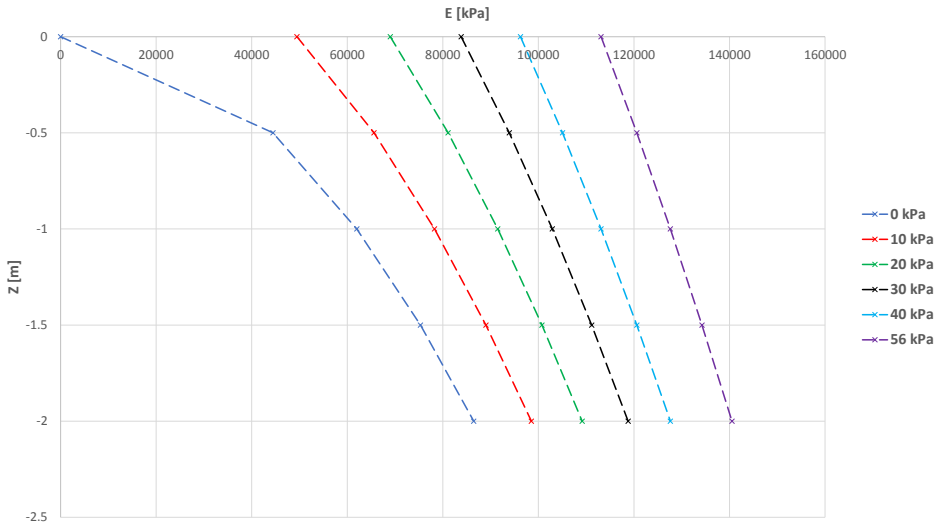

Figure 6.4: Stiffness profiles for different values of overburden pressure

Rayleigh Damping

The linear elastic material model in PLAXIS 3D includes no material damping, and this must be defined by means of Rayleigh Damping. Rayleigh damping has significant limitations with regards to modelling of the hysteretic damping properties of soils. Using Rayleigh Damping, it is only possible to specify one damping ratio for the entire time-series, and the reduced damping ratio with strain amplitude can not be modelled. The decreased damping with increased overburden pressure was taken care of by varying the Rayleigh coefficients for the separate calculations.

A damping ratio was specified for two different frequencies around the systems first eigenfrequency. The damping of the pile material was set to 0.005 for frequencies around the first eigenfrequency, seeing as the damping observed in the laboratory approaches this value for large values of overburden stress. Having no damping in the pile material was also observed to cause disturbance from higher frequencies. The material damping in the soil needed to be adjusted for the geometric and material damping observed in the laboratory. An effort was made to define a ζ_{soil} which gave the *maximum*

damping observed in the laboratory. This means a logarithmic decrement of 0.05, 0.015, 0.013, 0.01, 0.008 and 0.007 for a overburden pressure of 0, 10, 20, 30, 40 and 56 respectively. By fitting and comparing the logarithmic decrement of the different time-series, it was achieved in finding values for the Rayleigh damping which gave approximately the same damping as by laboratory tests. Table 6.2 shows the specific damping ratios defined for the soil to obtain a good fit.

Overburden pressure [kPa]	ζ_{pile} [-]	ζ_{soil} [-]	Frequency range [Hz]
0	0.005	50	7-11
10	0.005	20	7-11
20	0.005	15	7-11
30	0.005	15	7-11
40	0.005	10	7-11
56	0.005	10	7-11

Table 6.2: Damping ratios used to model soil damping

Seeing as little difference was found in the logarithmic decrement for overburden pressure of 20 and 30 kPa, ζ_{soil} was set as equal here. The same goes for 40 and 56 kPa.

Comments on Soil Parameters

The weight density of the sand has been measured in previous investigations Lieng (1984) and is considered to be a well established parameter. However, the parameters ν, K_0' and R_{inter} were assumed values. The Poisson's ratio for soils varies with soil type and strain amplitude. However, for small strains and elastic soil behaviour a value of 0.2 for dry sand is a decent assumption. The interface roughness was difficult to determine, and also has some effect on the eigenfrequency of a system. An increased roughness will increase the eigenfrequency of the system. This is due to the reduction of stiffness according to equation (6.1) (Brinkgreve et al. (2013c)):

$$G_i = R_{inter}^2 G_{soil} \tag{6.1}$$

For the interface in question, a value of $R_{inter} = 1.0$ was chosen. When calculating collapse loads, an interface strength of 1.0 for dry sand against smooth steel would be too high. However, there exist doubt as to how much relative movement there is, and seeing as a reduction in interface strength will decrease the system stiffness, a value of 1.0 is considered a better option.

The coefficient of lateral stress was tested in an oedotriaxial setup by Moen (1978) and found to be 0.3. This is, however, a very low value and corresponds to a friction angle of close to 45°. Therefore a value of 0.38 was chosen based on Jaki's formula.

6.3.2 Hardening Soil Small

The Hardening Soil Small (HSS) model is characterized as an advanced soil model for the simulation of soil behaviour. Limiting states are described as for the Mohr-Coulomb model by the means of c, ϕ and ψ. However, soil stiffness is modelled more accurately by the three parameters E_{50}, E_{ur} and E_{oed}. HSS also has the feature of increasing stiffness with effective stress following the power rule with exponent m. The HSS model includes two additional parameters G_0^{ref} and $\gamma_{0.7}$ in order to account for what is known as small-strain stiffness. Determination of material parameters for HSS was challenging, and was performed based on previous laboratory tests evaluated against experimental numbers for quartz sand. For further explanation of parameter determination see Appendix E. The parameters used can be found in table 6.3.

General			Dry sand	Interface
Material model			HSS	HSS
Drainage type			Drained	Drained
Parameter	Symbol	Unit	Value	
Weight density	Υ	$[kN/m^3]$	16	16
Cohesion	c	$[kPa]$	1	1
Friction angle	ϕ	[°]	38	38
Dilatancy	ψ	[°]	8	8
Secant stiffness	E_{50}^{ref}	$[MPa]$	50	50
Oedometer stiffness	E_{oed}^{ref}	$[MPa]$	50	50
Elastic u-r-stiffness	E_{ur}^{ref}	$[MPa]$	100	100
Shear stiffness	G_0	$[MPa]$	100	100
Stress exponent	m	[−]	0.48	0.48
Threshold shear strain	$\gamma_{0.7}$	[−]	10^{-4}	10^{-4}
Coeff. of lateral stress	K_0	[-]	0.38	0.38
Poisson's ratio	ν'	[-]	0.2	0.2
Interface strength			Rigid	Rigid
Strength reduction	R_{inter}	[-]	1.0	1.0

Table 6.3: Material properties of soil and interfaces for linear elastic material model

Comments on material parameters

- Weight density, Poisson's ratio, coefficient of lateral stress and interface strength were as discussed for the linear elastic soil model.
- Soil cohesion was considered to be 0 kPa for dry sand. It was, however, set to a value of 1 kPa to avoid numerical issues.
- The friction angle was previously tested to a value of 38°, and this also correlated well with Brinkgreve et al. (2010).
- For the threshold shear strain and soil dilatancy, no experimental results existed, and the correlations of Brinkgreve et al. (2010) were used.
- The stress exponent and the initial shear stiffness of the Hokksund sand were found using shear wave measurements and were well established material parameters.
- The oedometer stiffness was fitted to match previous investigations of the sand as can be seen in Appendix E. As by Brinkgreve et al. (2010), the secant stiffness was taken as $E_{50} = E_{oed}$, while the unloading-reloading stiffness was taken as $E_{ur} = 2 \times E_{oed}$. The stiffness parameters were of major importance to the structure in question, and an effort was made to fit these parameters to previous laboratory investigations. As seen in Appendix E, this was not a straight-forward process. Using the stress exponent found from elastic wave propagation, the results could only be fitted for the first part of the curve. To obtain a proper fit with oedometer results, the exponent must be changed and this was considered an inaccurate option. The oedometer stiffness was therefore fitted to the first part of the curve only.

6.4 Mesh

Soil volume in PLAXIS 3D was modelled by 10-node tetrahedral elements, and the finite element mesh consists of a finite number of such elements. The characteristics of a finite element mesh is defined by its coarseness (fineness). Using a finer mesh will give more elements, more nodes and stress points and thus increase computational time. Therefore, significant understanding is needed to optimize the mesh such that it represents the problem in a sufficiently accurate manner without too much computational

effort. There exist a parameter called target element dimension l_e defined by:

$$l_e = \frac{r_e}{20}\sqrt{(x_{max} - x_{min})^2 + (y_{max} - y_{min})^2 + (z_{max} - z_{min})^2} \tag{6.2}$$

Based on a parameter called relative element size factor r_e. r_e is defined by five different global levels. From the highest value of *very coarse* to the lowest value of *very fine*. The target element dimension l_e relates to the critical time step in dynamic calculations by equation (4.11). For description of the interpolation functions, its derivatives and the numerical integration of this element type, it is referred to Brinkgreve et al. (2013c). The finite element mesh was investigated based on the four global levels of relative element size. The resulting target element size was found in the general information tab in PLAXIS output mode and can be seen in table 6.4.

Relative element size	Target element dimension [m]
Very coarse	0.2176
Coarse	0.1755
Medium	0.1120
Fine	0.07602

Table 6.4: Relative element size and the resulting target element dimension

According to Kramer (1996), the maximum dimension of the finite element mesh is related to the shortest wavelength considered in the analysis. Here, the first eigenfrequency was of interest, and was found to be in the range of 8-10 Hz, depending on the amount of overburden pressure. Using, $f = 10$ Hz and $V_P = 200$ m/s, which was around the P-wave velocity measured in the laboratory for 0 overburden pressure, gave a *maximum element dimension* of:

$$\frac{1}{8}\lambda = \frac{1}{8}\frac{200}{10} = 2.5m \tag{6.3}$$

Due to the relatively low loading frequency combined with high wave velocities, the maximum element dimension is very large compared to the model boundaries, and a global level of *very coarse* was considered sufficient. However, with soil layers of 0.5 m thickness for the linear elastic soil model, a global level of *coarse* was needed in order to avoid problems with the flexibility of the elements. The mesh was refined in the area around the pile by defining a *local fineness factor* of 0.125. This allows for a more accurate determination of the deformation pattern of the pile.

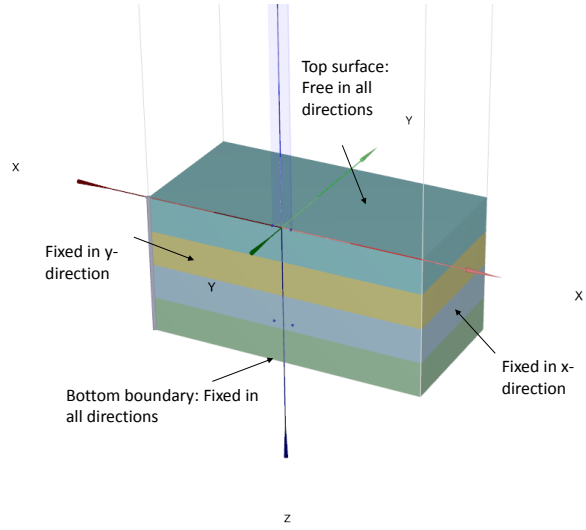

Figure 6.5: Soil volume showing the standard fixities introduced by PLAXIS

6.5 Boundary Conditions

6.5.1 Static Boundary Conditions

For the soil volume, standard fixities were used. According to Brinkgreve et al. (2013b), these are generated according to the following rules:

- Vertical boundaries with their normal in x-direction are fixed in x-direction and free in y- and z-direction.
- Vertical boundaries with their normal in y-direction are fixed in y-direction and free in x- and z-direction.
- Vertical boundaries with their normal in either x- nor y-direction are fixed in x- and y-direction and free in z-direction.
- The model bottom is fixed in all directions.
- The model surface is free in all directions.

Figure 6.5 shows the soil volume and its fixities. The pile was modelled as a plate. According to Brinkgreve et al. (2013b), beams and plates that extend to the model boundary where at least one displacement direction is fixed, obtain at least two fixed rotations in the points at the boundary. In this case, the pile extend to the vertical boundary with normal in y-direction. This means for the structure here:

- $\varphi_x = \varphi_z = 0$ with φ_y free.
- At the model surface: $\varphi_x = \varphi_y = \varphi_z = free$.

No rotation about the z-axis means that no torsion will occur in the pile, and no rotation about the x-axis means that the pile can not rotate perpendicular to the load direction. Seeing as the first mode of vibration was of interest here, this was considered improve the results. Having all the rotations free at the model surface, was considered to have little influence on the results.

6.5.2 Dynamic Boundary Conditions

For dynamic boundary conditions, the option "none" was used. This means the boundaries were unchanged with respect to the standard fixities. This will cause wave reflections at the model boundaries. However, this was considered to model the laboratory conditions in a more accurate way than by for example introducing viscous boundary conditions. To reduce wave propagation, Rayleigh damping was introduced.

6.6 Loading

The load was defined as a dynamic point load with magnitude $F_x = 0.5kN$. A *dynamic load multiplier* was also defined based on acceleration measurements of the hammer used in the laboratory investigations to model the impulse loading caused by the hammer blow. The load multiplier was defined by the five points in table 6.5.

Time [s]	Dynamic multiplier [-]
0.000	0.000
0.001	0.057
0.004	1.000
0.008	0.073
0.009	0.000

Table 6.5: Dynamic multiplier

6.7 Surface Load

For the HSS model, a surface load was introduced to model the overburden pressure used in the laboratory investigations. The load was applied to the

entire surface and the magnitude was adjusted according to the different measurement series of 0 - 10 - 20 - 30 - 40 and 56 kPa overburden pressure.

6.8 Dynamic Time Step

Seeing as the Newmark integration scheme is unconditionally stable for the default values of α and β chosen here, the challenge was to determine the time step needed for sufficient accuracy.

Using a *coarse* mesh, refined in the area around the pile, gave an average element dimension of $l_e = 0.07602$ m (from PLAXIS Output), $\alpha = 0.75$ (as for the 15-node element in 2D), a maximum compression wave velocity of $V_P = 200$ m/s and assuming that the second root term in equation (4.11) is close to 1, gives a critical time step $\Delta t_{critical} = 4.5 \times 10^{-4}$ s.

The critical time step is, however, meant to describe the maximum frequency of the finite elements. For the problem in question, the first mode of vibration is of interest, and this has a frequency of around 8-10 Hz, depending on the soil stiffness. Therefore, the necessary time step to describe the problem need to be investigated further. Equation (4.11) gave a critical time step of order 10^{-4}. However, investigations showed that a time step of order $10^{-}3$ was sufficient for obtaining accurate results.

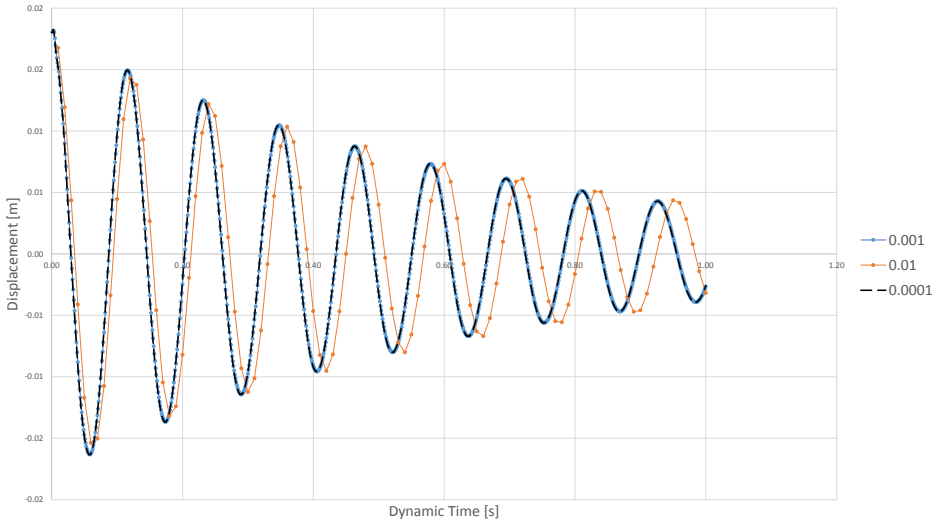

Figure 6.6: Time series using different order of magnitude for time step

As can be seen from figure 6.6, a time step of order 10^{-3} gives very

similar results as a time step of order 10^{-4}, while a time step of order $10^{-}2$ shows some deviations. Thus, it was concluded that a time step of $10^{-}3$ was sufficient to obtain an accurate solution, and was chosen in order to reduce computational effort.

Part III

Results, Discussion, Conclusions and Further Work

Chapter 7

Results and Discussion

In this chapter, the results from the back-calculations will be presented, discussed and compared to laboratory investigations. The calculations were performed using two different material models to enable comparative and reliable results. The system's first eigenfrequency was of main interest and will be considered for different values of overburden pressure. Also soil damping will be discussed and compared to laboratory measurements.

7.1 Linear Elastic Model

The dynamic response of the pile top was found using the finite element model described in Chapter 6. The time-series of the pile top displacement in x-direction for 0 overburden pressure can be seen in figure 7.1.

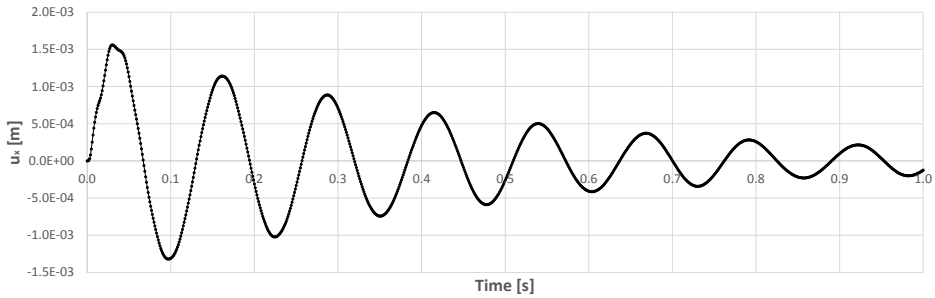

Figure 7.1: time-series of pile top displacement for 0 kPa overburden pressure.

Due to the nature of the impulse loading, which exited the pile in all its modes, the response for the first period showed some disturbance from other

frequencies. Also, note that the peak amplitude appeared after the impulse loading, which was as expected for short impulse loads (Chopra (1995)). From the second wave top, only the first eigenfrequency was observed, which was the one of interest here. This was due to the material damping, defined for both pile and soil, phasing out higher frequencies. Figure 7.2 to 7.6 shows the pile top displacement for different values of overburden pressure.

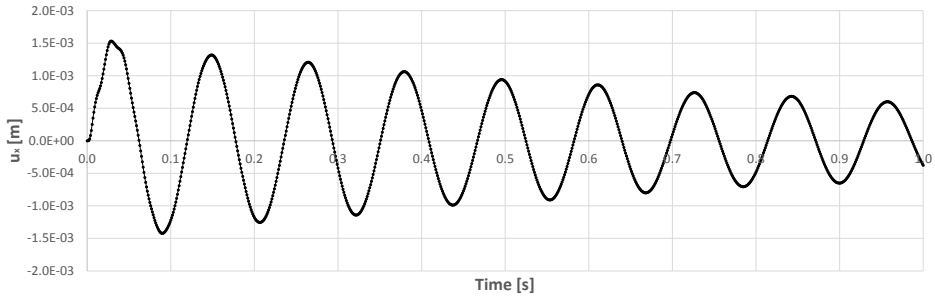

Figure 7.2: time-series of pile top displacement for 10 kPa overburden pressure

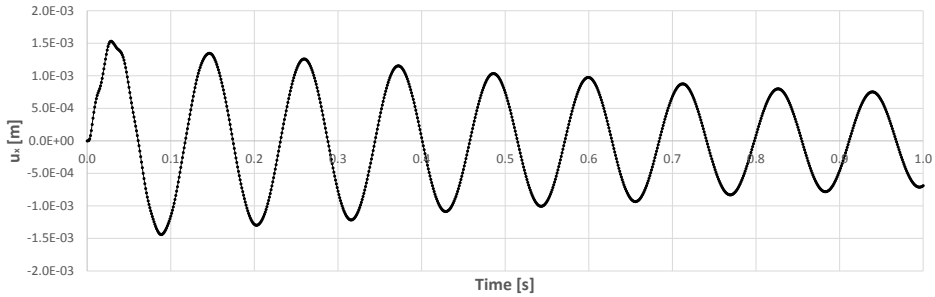

Figure 7.3: time-series of pile top displacement for 20 kPa overburden pressure

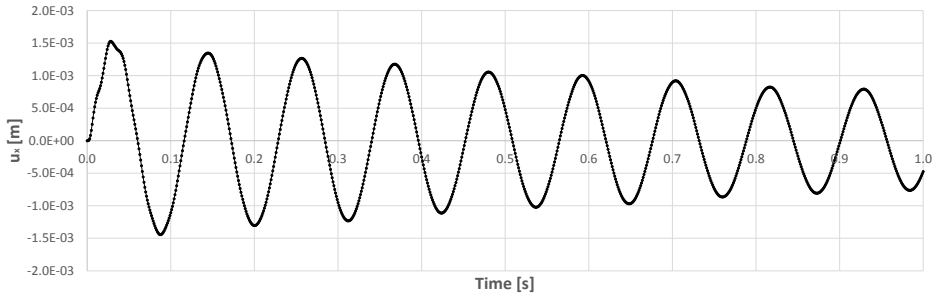

Figure 7.4: time-series of pile top displacement for 30 kPa overburden pressure

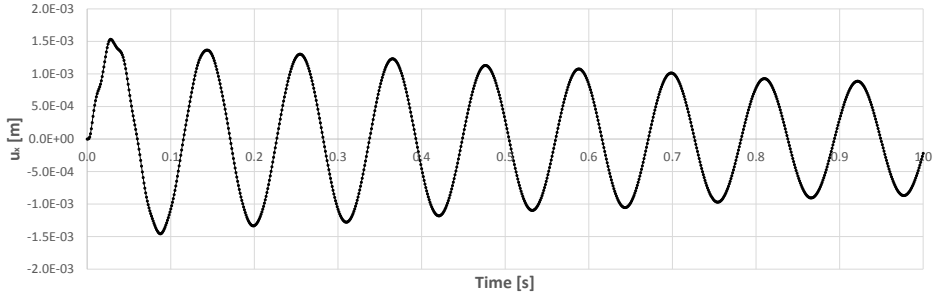

Figure 7.5: time-series of pile top displacement for 40 kPa overburden pressure

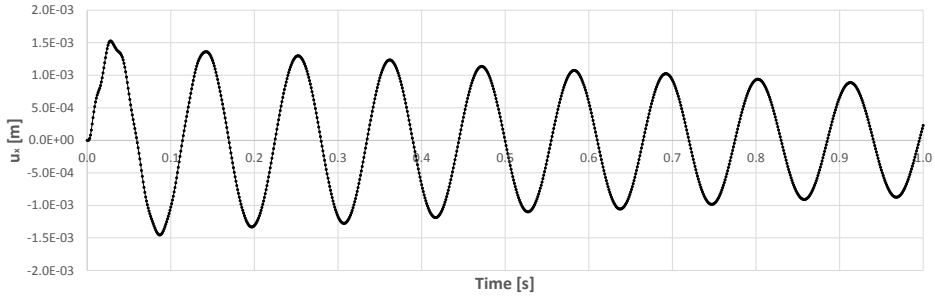

Figure 7.6: time-series of pile top displacement for 56 kPa overburden pressure

The response was very similar for all time-series. The only variation being the amount of damping introduced and the increased eigenfrequency

with increased overburden pressure. Interestingly, the peak response varied only slightly with overburden pressure although increased overburden pressure significantly increased soil stiffness. This indicates what was previously assumed; namely that the structural stiffness is the one of most importance with regards to the structural behaviour. However, the soil stiffness does influence, and next the eigenfrequency was studied.

Taking the inverse of the time difference from one wave top to the next, gave the eigenfrequnecy of the structure as calculated by PLAXIS 3D. This was performed automatically using a MATLAB script found in Appendix D. Figure 7.7 shows the eigenfrequency and its development with time for different values of overburden pressure as calculated by PLAXIS.

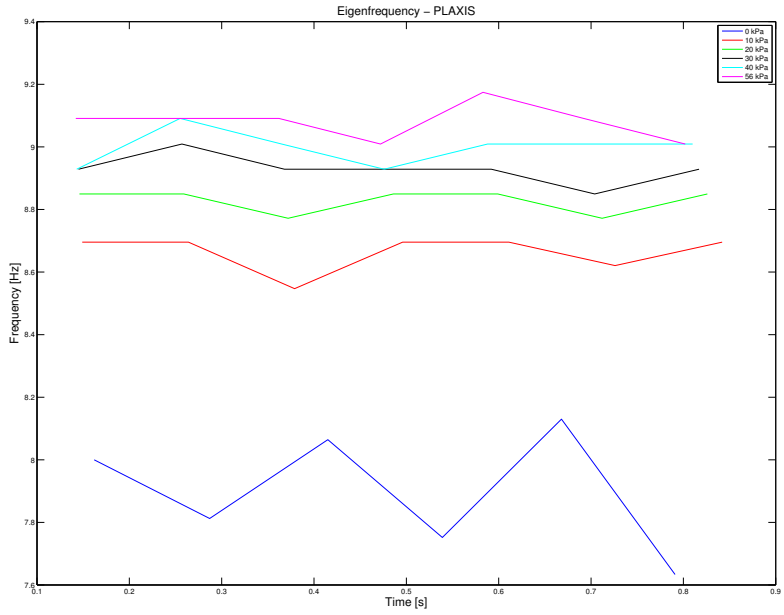

Figure 7.7: Eigenfrequency of the structure as calculated by PLAXIS 3D

As expected for a linear elastic soil model, the eigenfrequency shows little variation with time. The eigenfrequency was found to be increasing with increased overburden pressure due to the increased stiffness, and the only variation within each series with time was due to which point was found to be the wave top. The eigenfrequency was taken as the average values from figure 7.7, and eigenfrequency as calculated using linear elastic

soil in PLAXIS was compared to laboratory measurements in table 7.1.

Overburden pressure [kPa]	EF Lab [Hz]	EF LE [Hz]
0	7.7	7.9
10	8.3	8.7
20	8.5	8.8
30	8.6	8.9
40	8.7	9.0
56	8.8	9.1

Table 7.1: Eigenfrequency found from linear elastic material model compared to measurements

As can be seen from table 7.1, PLAXIS will in this case slightly overestimate the eigenfrequency of the system which was found to be from 7.7 Hz to 8.8 Hz for different overburden pressures from laboratory measurements. The overestimation was believed to have been caused by the use of G_0 as input stiffness. As by Benz (2006), the stiffness decrease with strain amplitude, and the stiffness used here was the maximum stiffness found for elastic wave propagation. Although the strains applied were considered to be relatively small, some stiffness reduction should be introduced, especially in the area around the pile. Interestingly, the increment in eigenfrequency with increasing overburden pressure was approximately the same for the calculations using PLAXIS 3D as for the laboratory measurements, and PLAXIS overestimates the eigenfrequency with a factor of around 1.025-1.050 for all values of overburden pressure. This indicates that soil stiffness does play a significant role with regards to the eigenfrequency and that PLAXIS was able to model the behaviour of the structure in a proper manner.

System damping was also introduced by use of Rayleigh damping. The logarithmic decrement was found for the different time series, and can be seen in figure 7.9. The damping ratios defined were found to represent the *maximum* damping observed in the laboratory in a sufficiently accurate manner. The logarithmic decrement in figure 7.8 is close to the same maximum values obtained by laboratory testing. The obtained Rayleigh damping was taken as the average values in figure 7.8, and table 7.2 shows a comparison between the Rayleigh damping in the linear elastic soil model and observations in the laboratory. The values in table 7.2 match very well seeing as the Rayleigh damping was fitted to match laboratory investigations. An exact match was not considered necessary to obtain, and would be relatively time-consuming to perform. The Rayleigh coefficients indicate that the system damping is highly mass-proportional with an α_R with order

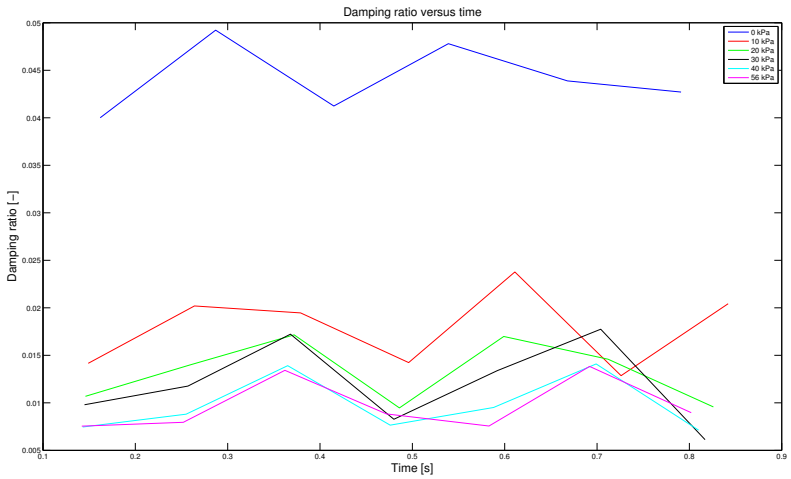

Figure 7.8: Logarithmic decrement from PLAXIS calculations

Overburden pressure [kPa]	ζ_{lab} [-]	ζ_{LE} [-]
0	0.050	0.045
10	0.015	0.015
20	0.012	0.012
30	0.011	0.012
40	0.008	0.008
56	0.007	0.008

Table 7.2: Comparison between Rayleigh damping and observed maximum damping in the laboratory

of magnitude 10^3 larger than β_R. Physically, mass-proportional damping is difficult to interpret. For this problem, however, it is believed to be the relative movement and friction between grains which cause most of the dissipation of energy. This was confirmed by the reduced damping for increased overburden pressure, seeing as increased overburden pressure will reduce grain movement. Considering this, mass-proportional damping could, at least in this case, have the physical interpretation as frictional damping.

7.1.1 Discussion of Results

Calculating eigenfrequency by PLAXIS 3D using the relatively simple linear elastic material model was found to give a reasonable estimate of the first eigenfrequency. However, the linear elastic model has several limitations compared to more advanced models. Most importantly, for this structure, it does not take into account the increasing stiffness with depth and the reduced stiffness upon straining. Increased stiffness with depth was taken care of here by introducing four different layers, and a linearly increasing stiffness with depth within each layer. This gave a reasonably good estimate of the stiffness profile based on G_0. G_0 is, however, an initial stiffness assumed to hold only for very small strains ($< 10^{-6}$). Upon straining, the sand will lose some if its stiffness due to a reduction in intermolecular bonds and re-arrangement of grains. This will mostly happen close to the surface and in the area around the pile, while most of the soil will keep its initial strength. Appendix G shows a contour plot of the shear strains at different values of overburden pressure, meaning different stiffness input for the soil. Using the linear elastic model, there is no way to model this local stiffness reduction, and a more advanced model such as the Hardening Soil Small must be used.

Rayleigh damping was used to model the dissipation of energy observed in the laboratory testing. Although it was succeeded in obtaining almost the same maximum logarithmic decrement as observed in the laboratory, Rayleigh damping has significant limitations with regards to the hysteretic damping behaviour of soils. While most soils show reduced damping with reduced strain amplitude, Rayleigh damping is only able to model a mass- and stiffness-proportional damping constant with strain amplitude. There also exist considerable practical problems with regards to Rayleigh damping. Here the damping ratios were fitted to match the measured response. However, for real projects this is not an option, and the damping could be better approximated by hysteretic damping as in the HSS model.

7.2 Hardening Soil Small

The HSS model includes several features such as reduced stiffness with strain amplitude, increased stiffness with depth and hysteretic damping which makes it more suitable for dynamic calculations of the problem in question. Six calculations were performed for comparison with the calculations using the linear elastic soil model. Parameters used and details on the finite element model can be found in Chapter 6. Here the results are presented, discussed and compared to the results from the linear elastic model and laboratory measurements.

The time-series of pile top displacement can be seen in figure 7.9 to 7.14.

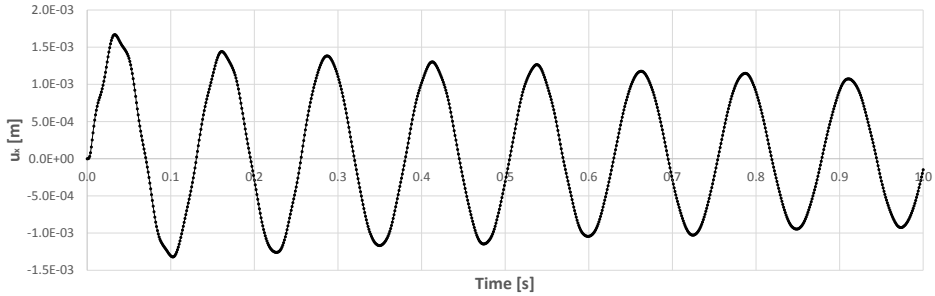

Figure 7.9: time-series of pile top displacement for 0 kPa overburden pressure using HSS

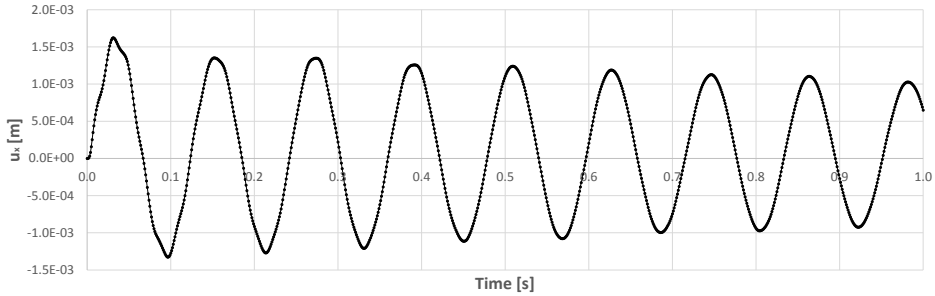

Figure 7.10: time-series of pile top displacement for 10 kPa overburden pressure using HSS

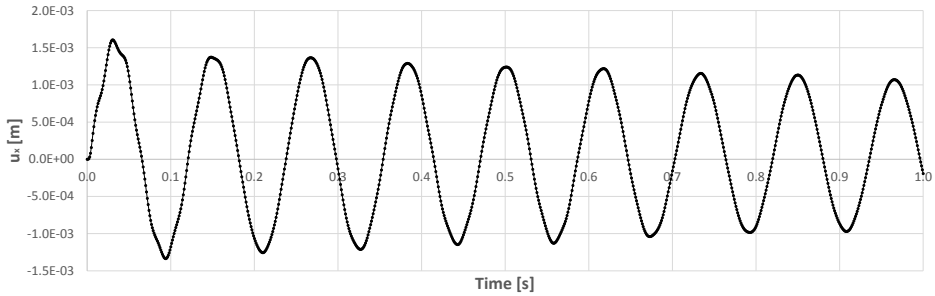

Figure 7.11: time-series of pile top displacement for 20 kPa overburden pressure using HSS

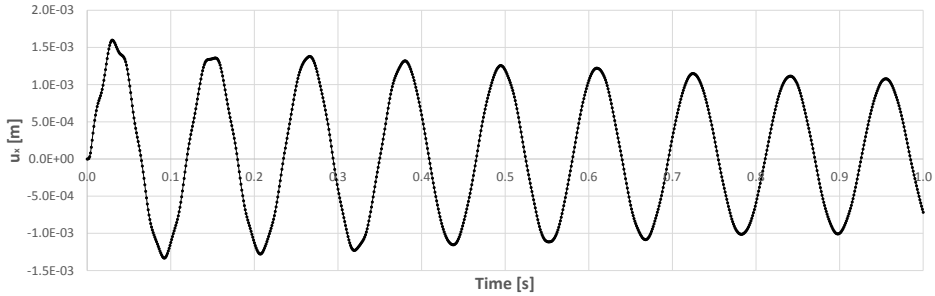

Figure 7.12: time-series of pile top displacement for 30 kPa overburden pressure using HSS

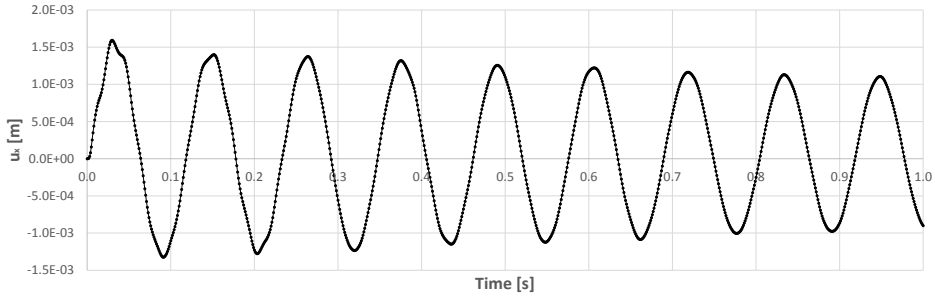

Figure 7.13: time-series of pile top displacement for 40 kPa overburden pressure using HSS

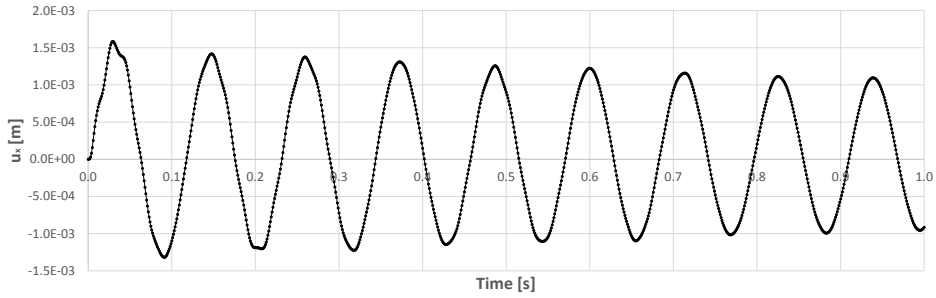

Figure 7.14: time-series of pile top displacement for 56 kPa overburden pressure using HSS

As for the linear elastic model, the peak response appears after the impulse loading. The peak response was slightly larger using HSS than the linear elastic model. This was believed to be due to the plastification of the soil around the pile in the first period of vibration during which the soil stiffness was governed by E_{50}. The plastification expanded the elastic region, and after this the stiffness was governed by G_{ur} and G_0 depending on the amount of shear strains. Appendix I shows contour plots of G/G_{ur} which describes which stiffness was used by PLAXIS in the different parts of the mesh.

The only damping contribution was from the hysteretic damping, which is automatically implemented in the HSS model. Therefore the damping observed in the laboratory was not sufficiently modelled for all series, especially for the calculation without overburden pressure. This could be fitted adding Rayleigh damping to the hysteretic damping. However, since the hysteretic damping is evaluated here, this was not performed.

Interestingly, the displacement in the positive x-direction was found to be larger than the displacement in the negative x-direction. This can be observed from figure 7.9 to 7.14 where the second wave top is larger than the first wave bottom. The reason for this was believed to be the plastification of the soil which occurs during the first period of loading in the HSS model. This most likely caused the pile to rotate slightly, shifting the point that the pile top vibrates about slightly in the positive x-direction.

The eigenfrequency was taken as the inverse of the time difference from one wave top to the next. It was found automatically using a MATLAB script, and the results can be seen in figure 7.15.

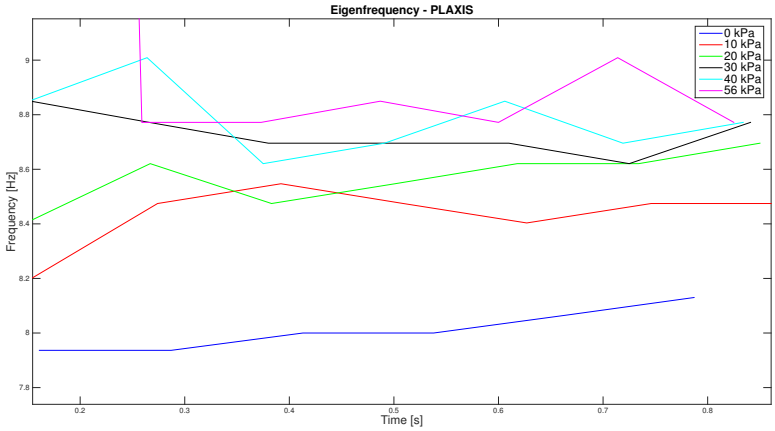

Figure 7.15: Eigenfrequency of the structure as calculated by PLAXIS 3D using HSS

The calculated eigenfrequency was found to vary in the range of 8.0 to 8.9 Hz when using the HSS model, with increasing eigenfrequency with increasing overburden pressure due to the stress-dependent stiffness. The HSS model was generally close to the true eigenfrequency. Only the series without overburden pressure produced a significant error, and this was believed to have been caused by the fact that the linear stiffness profile significantly underestimates soil stiffness for that series thus decreasing the eigenfrequency. This series was also the one with most uncertainty due to the high variation of eigenfrequency with time observed in the laboratory, and was also the most unrealistic series, seeing as the low stiffness around the surface is hard to model, and there will be larger displacements than in reality for such structures. HSS will therefore overestimate this eigenfrequency since the stiffnesses used were relatively large and only relevant for structures in the small-strain range. The eigenfrequency from the HSS model was taken as the average values in figure 7.15. Table 7.3 shows a comparison between the measured eigenfrequency and the eigenfrequency calculated using the HSS model.

Overburden pressure [kPa]	EF Lab [Hz]	EF HSS [Hz]
0	7.7	8.0
10	8.3	8.4
20	8.5	8.6
30	8.6	8.7
40	8.7	8.8
56	8.8	8.9

Table 7.3: Eigenfrequency found from linear elastic material model compared to measurements

The other series with overburden pressure from 10 to 56 kPa compared well to the laboratory measurements and only overestimated the eigenfrequency by a factor of around 1.01. Note that the for the series with 56 kPa overburden pressure, MATLAB found the wave tops wrongly for the first few periods. This also affects the damping ratio in figure 7.16.

The hysteretic damping automatically implemented in the HSS model was of great interest here, and therefore no effort was made to fit the laboratory measurements to the calculations using Rayleigh damping, although this was possible. The objective was to find to which degree the hysteretic damping can describe the damping observed in the laboratory. Therefore, the damping was investigated using the method of logarithmic decrement. Figure 7.16 shows the logarithmic decrement plotted versus time.

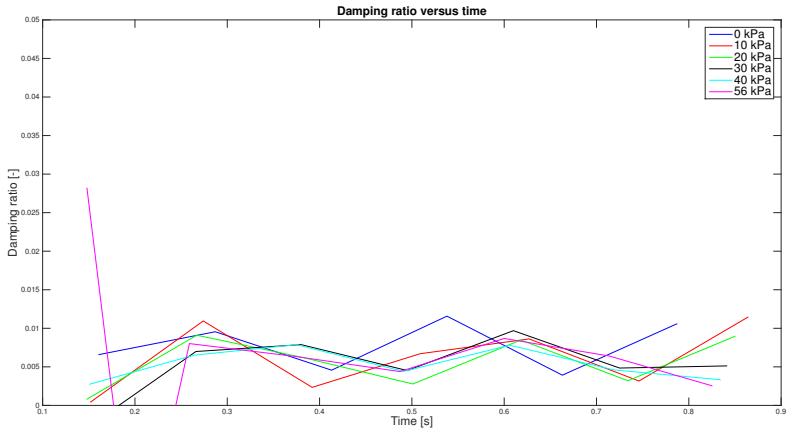

Figure 7.16: Logarithmic decrement plotted versus time for the HSS calculations

Considering figure 7.16, the hysteretic damping used by the HSS model gave a logarithmic decrement in the range of 0.005 to 0.01. This was approximately the same as observed in the laboratory when the strain amplitude decreased. Table 7.4 shows the damping ratio obtained for the HSS model compared to laboratory observations.

Overburden pressure [kPa]	ζ_{lab}	ζ_{HSS}
0	0.050	0.008
10	0.015	0.007
20	0.012	0.007
30	0.011	0.007
40	0.008	0.007
56	0.007	0.007

Table 7.4: Damping ratio for the HSS model compared to laboratory measurements

The hysteretic damping is of great interest, seeing as it is automatically implemented based on the stiffness parameters. No significant variation in the hysteretic damping was observed for the different series. Seeing as the calculated displacement amplitude was similar for all values of overburden pressure, this was as expected. The hysteretic damping is proportional to the area inside the unloading-reloading loop, and, as can be seen from figure 7.9 to 7.14, there were little change in the displacement amplitude for the different series. The magnitude of the hysteretic damping fitted the maximum damping for the series with 40 and 56 kPa overburden pressure very well. The largest deviation observed being the series without overburden pressure, for which the assumption of small-strain stiffness was considered to be wrong.

The calculations show little or no variation in logarithmic decrement with time, and the only variation observed was due to the variation in what was found as the wave tops. To get a better idea of the variation with time (or amplitude), longer dynamic calculation time must be used. Due to significant computational effort this was only performed for one calculation. Figure 7.17 shows the logarithmic decrement of a calculation performed with dynamic time of 6 s. The results show significant scatter, and in order to see the trend of the damping, the basic fitting tool in MATLAB was used. As expected the damping ratio was shown to decrease with decreasing amplitude. Soil damping is proportional to the area inside the unloading-reloading loop, and when the amplitude decreases, so does the damping.

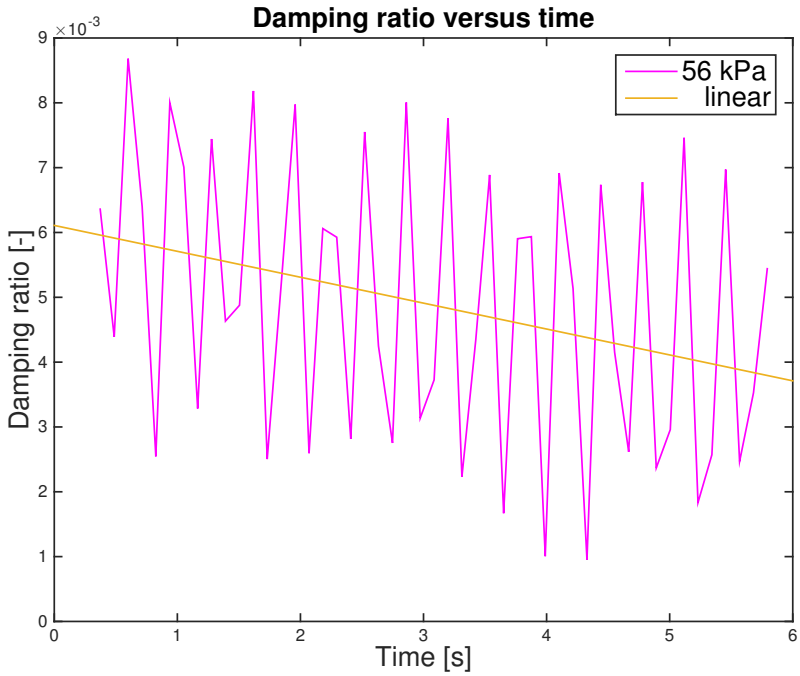

Figure 7.17: Hysteretic damping of the HSS model

7.2.1 Discussion of Results

The HSS model generally performed well in back-calculating the first eigenfrequency of the system, with the exception of the series without overburden pressure. This measurement was, however, difficult to model due to the very low stiffness around the surface combined with the relatively low embedded length of the pile. This will cause larger deformations at the surface, and create surface effects. This was also confirmed by the PLAXIS calculations in appendix H, which showed that the maximum shear strains were of a higher order of magnitude for this series. Seeing as a cut of shear strain γ_c is introduced, the HSS model will not reduce the stiffness further after this value is reached. In reality, however, the stiffness will continue to reduce upon straining, and this was believed to be the reason for the higher error in this series.

For the calculations with overburden pressure, the HSS model overestimated the eigenfrequency with a factor of around 1.01. Considering the uncertainty in parameters such as G_{ur}, ν_{ur} and R_{inter} which all have considerable impact on the system eigenfrequency, the results are very satisfying.

The main reason why the HSS model performed better was the reduced stiffness with strain amplitude. This can be seen in appendix I where contour plots of G/G_{ur} are shown. The stiffness in the area around the pile will be reduced due to the occurrence of shear strains (appendix H). Physically, this means that the re-arrangement of grains as the pile moves back and forth causes a loss of stiffness which can be described as a loss of intermolecular bonds and re-arrangement of grains.

The HSS model also models the stiffness in a more accurate manner by using a power rule for an increasing stiffness with depth, fitting well with the stiffness profile found from laboratory measurements.

The shear strain profiles are shown in appendix H. Note that the shear strain profiles in Appendix G and H show the calculated shear strains for the *last* dynamic time step. This means that the magnitude of shear strains can not be compared for the different values of overburden pressure, seeing as the magnitude of shear strain will vary depending on the displacement magnitude for the last time step. The shear strain profiles should therefore be considered in context with figure 7.1 to 7.6 and figure 7.9 to 7.14. However, it does give an indication of the deformation pattern of the pile. With the exception of the series without overburden pressure, it was believed that the calculated shear strains were of same order of magnitude. This indicated that the increased eigenfrequency with overburden pressure was due to the stress-dependent stiffness and not the reduced occurence of shear strains.

The hysteretic damping in HSS was found to be representative only

for the series with 40 and 56 kPa overburden pressure. The logarithmic decrement obtained from the HSS calculations were in the same range as observed in the laboratory for these series. As by Seed and Idriss (1970) and from laboratory measurements, damping ratio for soils vary with confining stress and strain amplitude. However, no variation with overburden pressure was found from the HSS results. This was as expected seeing as this feature is not implemented into the PLAXIS code and the calculated displacement amplitude were similar for all series. The hysteretic damping should, however, show a variation through a time-series seeing as the damping is proportional to the area inside the unloading-reloading loop, with a larger damping ratio at the start when the amplitude is larger. This was found to be true also in this case by using longer dynamic calculation time for one of the series.

The hysteretic damping from the HSS model is more suited for practical application with regards to soil damping. Using Rayleigh damping, one must guess on a damping ratio and try to fit this to relevant experience, if existent. Hysteretic damping is created automatically from the area of the unloading-reloading loop, and can thus be used directly. It will, however, not in all cases give the correct damping ratio. In the case with no overburden pressure especially, it underestimates soil damping significantly. In such cases it is possible to use Rayleigh damping in order to obtain similar damping to experience. However, experience numbers do not always exist and will depend on soil type and type of structure.

7.3 Material Models Comparison

Both models were found to be suited for deformation calculations of the structure. The HSS model, however, performed significantly better in estimating the eigenfrequency of the structure. HSS overestimated the eigenfrequency by a factor of around 1.01 while the linear elastic model overestimated by a factor of around 1.03. The reasons for this have been discussed previously, and are mainly the strain-dependent stiffness in the HSS model. Figure 7.18 shows the variation in eigenfrequency with overburden pressure for both material models compared to laboratory results.

Damping is not automatically included in the linear elastic model as in the HSS model. While the hysteretic damping introduced in the HSS model was in the correct range for two of the calculation, it does not include a change in damping ratio with confining stress as observed in the laboratory. The advantage of the HSS model is that it gives an estimate of the damping based on the stiffness quantities of the soil.

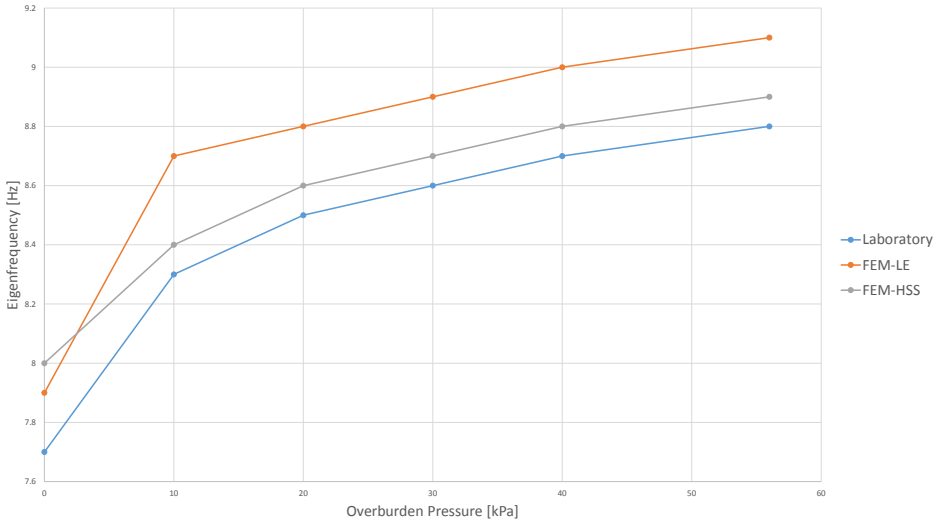

Figure 7.18: Eigenfrequency as calculated by PLAXIS compared to laboratory measurements

Modelling a piece-wise linear stiffness with depth using the linear elastic model was a cumbersome process. A reference stiffness had to be introduced for each layer as well as a linear increase with depth. The HSS model was superior in this case, only demanding a reference stiffness and a stress exponent with depth. A surface load could then be introduced to model the overburden pressure, which automatically increased the stress level in the soil and thus also the stiffness.

Chapter 8

Conclusions

The laboratory results were successfully back-calculated. Especially the eigenfrequency was well estimated using the numerical model described in this thesis. Assuming small-strain stiffness was found to represent the stiffness profile of the Hokksund sand in a good manner.

The eigenfrequency was generally better estimated using the HSS model than the linear elastic model, with the exception of the series with no overburden pressure, as previously discussed. The main advantage of the HSS model compared to the linear elastic and other material models is the stiffness reduction with strain amplitude. This feature makes the HSS model superior to material models without small-strain stiffness incorporated with regards to the problem in question, and also general deformation calculations of soils. However, the determination of parameters for the HSS model is challenging. As well as using well-known soil parameters such as cohesion, friction angle and dilatancy etc., the elastic stiffness G_0 and the reference shear strain $\gamma_{0.7}$ are needed in order to perform calculations using HSS. In this thesis, G_0 was found by elastic wave propagation. This is, however, an expensive procedure to carry out in field. Still, it would be beneficial to use the HSS model with G_0 and $\gamma_{0.7}$ based on correlations with other parameters or previous investigations on similar soil types.

The hysteretic damping of the HSS model was also found to be superior to the Rayleigh damping introduced in the linear elastic model. Using Rayleigh damping, the Rayleigh coefficients must be fitted to match an expected damping ratio which is difficult to perform without existing experimental numbers. The hysteretic damping in the HSS model is implemented automatically based on the stiffness parameters and a cut-off shear strain γ_c. This will, in any case, give a good first estimate of the damping ratio for the soil in question, and can also be improved by adding Rayleigh damping

as well.

Soil dynamics is often considered in the context of wave propagation, especially with regards to earthquake calculations. While wave propagation plays a significant role in the determination of soil stiffness G_0, it was here found to have little or no influence on the system eigenfrequency. For the problem in question there will be no concentration of waves, only disturbance as they reflect from the concrete walls surrounding the sand. The waves will therefore be unable to create any unison movement, and thus affect the deformations of the structure very little. This can also be transferred to the general case of monopile offshore wind turbine foundations, where the waves will spread out radially from the source (wind turbines) and have little or no effect on the surroundings.

Based on the results from this thesis, it can be concluded that PLAXIS 3D is well-suited for calculations of deformations and eigenfrequency of the pile in question. Both material models performed reasonably well with HSS the most suited of the two. The problem is best considered as a static structure with stiffness contribution from both soil and structure. Although the structural stiffness has the largest influence on the first eigenfrequency, soil stiffness also contributes significantly. The importance of the soil stiffness is confirmed by considering the increment in eigenfrequency by increasing the overburden pressure both with regards to the laboratory measurements and the PLAXIS calculations.

This thesis can be seen both as a validation of PLAXIS 3D for calculations of such structures and as a confirmation of the small-strain stiffness properties of the Hokksund sand. It is widely believed that such monopile windturbine foundations operate at a low strain level, and therefore exhibit a larger stiffness than measured in conventional laboratory testing. If the stiffness from oedometer or triaxial testing were to be used for the same problem, it would be likely to underestimate the eigenfrequency of the structure significantly and could cause design problems. Thus, based on the fact that the eigenfrequency from PLAXIS 3D matched the eigenfrequency measured in laboratory using the assumption of small-strain stiffness, it can be concluded that the soil do in this case show a larger stiffness than that from conventional laboratory tests.

Chapter 9

Further Work

This thesis successfully back-calculated the laboratory results, and found the numerical model to give a good estimate of the first eigenfrequency and damping ratio of the model pile. However, more work is required. The hysteretic damping quantities could be further examined using longer dynamic calculation time for all overburden pressures. It could also be of interest to compare the Hardening Soil Small model to the Hardening Soil model to check how much the small-strain overlay improves the results.

The pile top displacements calculated by PLAXIS was very similar for all values of overburden pressure, and this caused the hysteretic damping in the HSS model to show little variation with overburden pressure as well. Therefore, another objective could be to back-calculate the pile top displacements observed in the laboratory and compare to the numerical model. This could be achieved using the strain gage measurements and converting the voltage output to bending moments and then assuming a centre of rotation.

There also exist uncertainties with regards to several parameters used in this thesis. Among them are ν_{ur}, R_{inter}, ψ, E_{ur} and E_{50}, which were all assumed values or based on correlations with other parameters. Although it is challenging to recreate the in situ conditions for sand, an effort could be made to perform laboratory tests and determine more reliable estimates for the parameters ψ, ν_{ur}, E_{ur} and E_{50}. The parameter R_{inter} is difficult to determine. Its effect was studied slightly in this thesis and shown to decrease the eigenfrequency. This should, however, be further studied.

Dry sand is a material rarely found in nature, and back-calculations of full-scale wind turbine structures with known soil conditions could be very useful in expanding the knowledge with regards to the dynamic behaviour of such structures.

Design of offshore wind turbines is a demanding process with often more

than 20,000 load cases to be considered. It is therefore asked of the geotechnical engineer to come up with a simple model for the soil stiffness. Converting soil-structure interaction stiffness found in the time consuming FE-analysis to spring stiffness for more efficient analysis may be an interesting approach and is recommended for further studies.

Bibliography

Benz, T. (2006). *Small-strain stiffness of soils and its numerical consequences*. Inst. für Geotechnik.

Brinkgreve, R., Broere, W., and Waterman, D. (2013a). Plaxis 3d 2013 - material models manual. *Version*.

Brinkgreve, R., Broere, W., and Waterman, D. (2013b). Plaxis 3d 2013 - reference manual. *Version*.

Brinkgreve, R., Broere, W., and Waterman, D. (2013c). Plaxis 3d 2013 - scientific manual. *Version*.

Brinkgreve, R., Engin, E., and Engin, H. (2010). Validation of empirical formulas to derive model parameters for sands. *Numerical Methods in Geotechnical Engineering Numge*, pages 137–142.

Chopra, A. K. (1995). *Dynamics of structures*, volume 3. Prentice Hall New Jersey.

Darendeli, M. B. (2001). *Development of a new family of normalized modulus reduction and material damping curves*.

Duncan, J. M. and Chang, C.-Y. (1970). Nonlinear analysis of stress and strain in soils. *Journal of the Soil Mechanics and Foundations Division*, 96(5):1629–1653.

Hardin, B. O. and Drnevich, V. P. (1972a). Shear modulus and damping in soils: design equations and curves. *Journal of the soil mechanics and foundations division*, 98(7):667–692.

Hardin, B. O. and Drnevich, V. P. (1972b). Shear modulus and damping in soils: measurement and parameter effects (terzaghi leture). *Journal of the soil mechanics and foundations division*, 98(6):603–624.

Hashiguchi, K. (2009). *Elastoplasticity theory*, volume 42. Springer.

Hetland, J. (2014). *Investigation of Shear Wave Velocities and Small-Strain Stiffness in Sand*.

Ishibashi, I. and Zhang, X. (1993). Unified dynamic shear moduli and damping ratios of sand and clay. 33(1):182–191.

Janbu, N. (1967). *Settlement calculations based on the tangent modulus concept*. Technical University of Norway.

Kondner, R. L. (1963a). *A hyperbolic stress-strain formulation for sands*. Northwestern University.

Kondner, R. L. (1963b). *A hyperbolic stress-strain formulation for sands*. Northwestern University.

Kramer, S. (1996). Geotechnical earthquake engineeringprentice hall. *Upper Saddle River, NJ*.

Lieng, J.T., M. T. S. K. (1984). *Large Scale Model Tests - Test Facilities and Test Examples*.

Mair, R. et al. (1993). Unwin memorial lecture 1992. developments in geotechnical engineering research: Application to tunnels and deep excavations. delivered at the ice on 17 march 1992.(abridged).(winner of 1994 geotechnical research medal). In *Proceedings of the ICE-Civil Engineering*, volume 97, pages 27–41. Thomas Telford.

Moen, T. (1978). *Hokksund Sand. Determination of the Sand's Routine Data, Deformation and Strength Characteristics.*

Olivadoti, G. (2001). Sensing, analyzing, and acting in the first moments of an earthquake. *Analog Dialogue*, pages 35–1.

Oñate, E. (2013). *Structural Analysis with the Finite Element Method. Linear Statics: Volume 2: Beams, Plates and Shells*, volume 2. Springer.

Pal, O. (1998). *Modélisation du comportement dynamique des ouvrages grâce à des éléments finis de haute précision*. PhD thesis, thesis, L'université Joseph Fourier-Grenoble I.

Schanz, T., Vermeer, P., and Bonnier, P. (1999). The hardening soil model: formulation and verification. *Beyond 2000 in computational geotechnics*, pages 281–296.

Seed, H. B. and Idriss, I. M. (1970). Soil moduli and damping factors for dynamic response analyses.

Seed, H. B., Wong, R. T., Idriss, I., and Tokimatsu, K. (1986). Moduli and damping factors for dynamic analyses of cohesionless soils. *Journal of Geotechnical Engineering*, 112(11):1016–1032.

List of Figures

List of Tables

Nomenclature

$[\ddot{u}]$	Nodal acceleration vector
$[\dot{u}]$	Nodal velocity vector
$[C]$	Damping matrix
$[K]$	Stiffness matrix
$[M]$	Mass matrix
$[P(t)]$	Nodal force vector
$[u]$	Nodal displacement matrix
α	Newmark's integration parameter
α_e	Factor depending on type of element
α_R	Rayleigh coefficient
α_z	Impedance ratio
β	Newmark's integration parameter
β_R	Rayleigh coefficient
$\ddot{u}$	Acceleration
Δe	Deviatoric strain increment
δt	Dynamic time step
$\Delta t_{critical}$	Critical time step
ϵ	Strain
$\gamma_{0.7}$	Reference shear strain when G is reduced to 70 % of initial value

γ_c	Cut-off shear strain
γ_{hist}	Shear strain history
γ_h	Hyperbolic shear stress
γ_r	Reference shear strain
γ_s	Shear strain
λ	Wavelength
ν	Poisson's ratio
ν_{ur}	Poisson's ratio for unloading-reloading
ω	Circular frequency
ϕ	Friction angle
ψ	Dilatancy angle
ρ	Density
σ	Stress
σ_i	Incident stress
σ_r	Reflected stress
σ_t	Transmitted stress
τ_{max}	Maximum shear stress
Υ	Weight density
φ	Rotation
ζ	Damping ratio
a	Curve fitting parameter used in equation for γ_h
A_i	Incident wave amplitude
A_r	Reflected wave amplitude
A_t	Transmitted wave amplitude
B	Largest dimension of the finite element

b	Curve fitting parameter used in equation for γ_h
c	Soil cohesion
c_{cr}	Critical damping
D	Pile diameter
D_r	Relative density
E	Young's modulus
E_{50}	Modulus determined from triaxial tests for $q = 0.5q_f$
E_{oed}	Oedometer stiffness
E_t	Tangent modulus
E_{ur}	Unloading-reloading modulus
EI	Bending stiffness
f	Frequency
f_D	Damped frequency
G	Shear modulus
G_0	Initial shear modulus
G_s	Secant shear modulus
G_t	Tangent shear modulus
G_{ur}	Unloading-reloading shear modulus
H	Symmetric tensor describing the deviatoric strain history
I_P	Plasticity index
K	Modulus number
k	Stiffness
K_0'	Coefficient of lateral stress
K_{Rs}	Relation between Rayleigh velocity and S-wave velocity
K_{ur}	Unloading-reloading modulus number

L	Pile length
l_e	Average element length
m	Mass
m	Stress exponent describing increasing stiffness with depth
m_D	Maximum number of calculation steps
n	Porosity
n_D	Number of dynamic substeps
p'	Mean effective confining stress
p'_{ref}	Reference stress
p_a	Reference stress for the Duncan-Chang model
q	Deviatoric stress
q_a	Asymptotic deviatoric stress
q_f	Ultimate deviatoric stress
R_f	Curve fitting parameter
R_{inter}	Interface strength reduction factor
S	Surface area of the finite element
t	Dynamic calculation time
$tpile$	Pile thickness
u	Displacement
V_P	P-wave velocity
V_R	Rayleigh wave velocity
V_S	S-wave velocity

Appendix A

Timeseries from Strain Gage Measurements

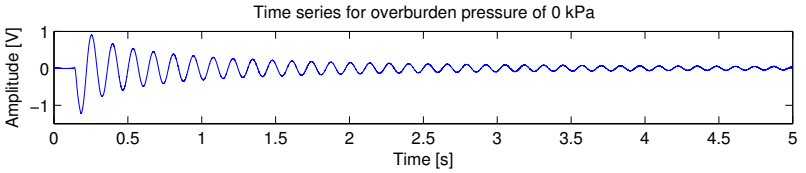

Figure A.1: Time series for overburden pressure of 0 kPa

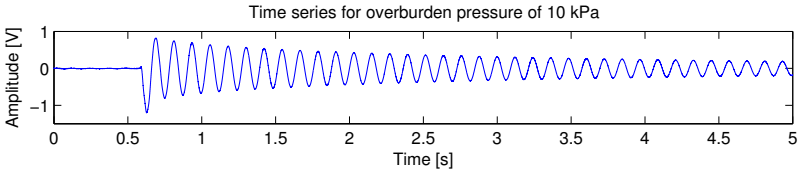

Figure A.2: Time series for overburden pressure of 10 kPa

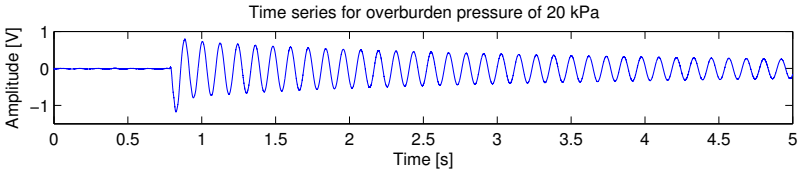

Figure A.3: Time series for overburden pressure of 20 kPa

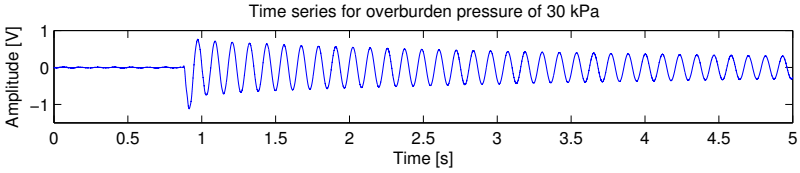

Figure A.4: Time series for overburden pressure of 30 kPa

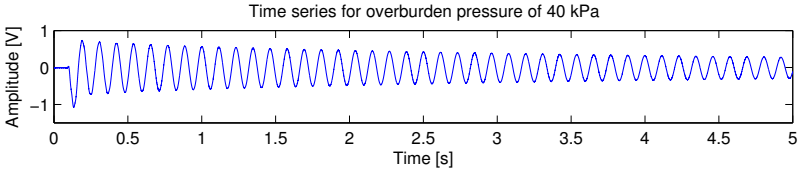

Figure A.5: Time series for overburden pressure of 40 kPa

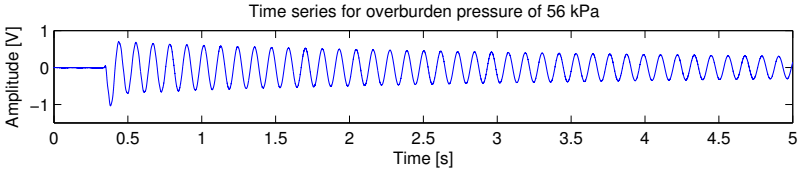

Figure A.6: Time series for overburden pressure of 56 kPa

Appendix B

Filtered and Unfiltered Timeseries Example

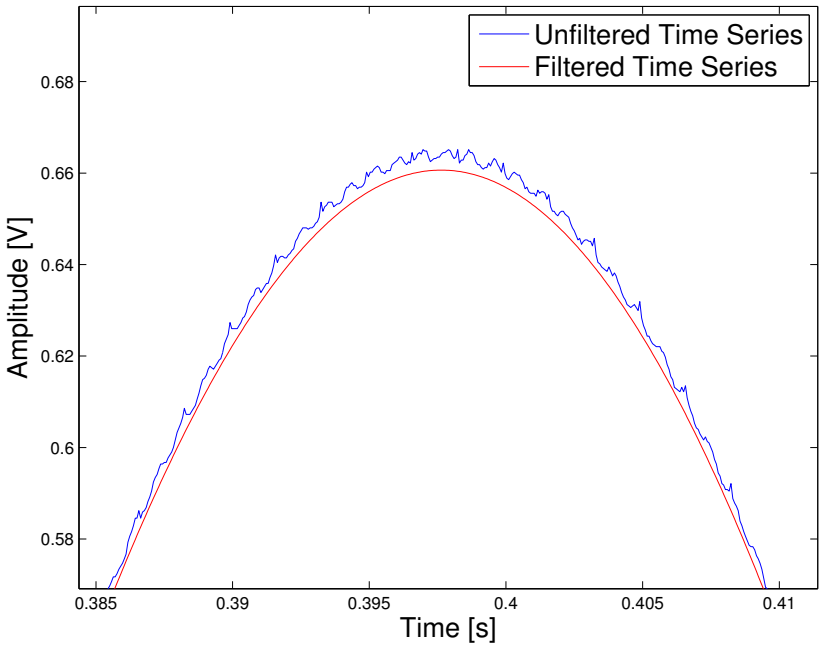

Figure B.1: Unfiltered and filtered time series

Appendix C

Pile lab with Pump

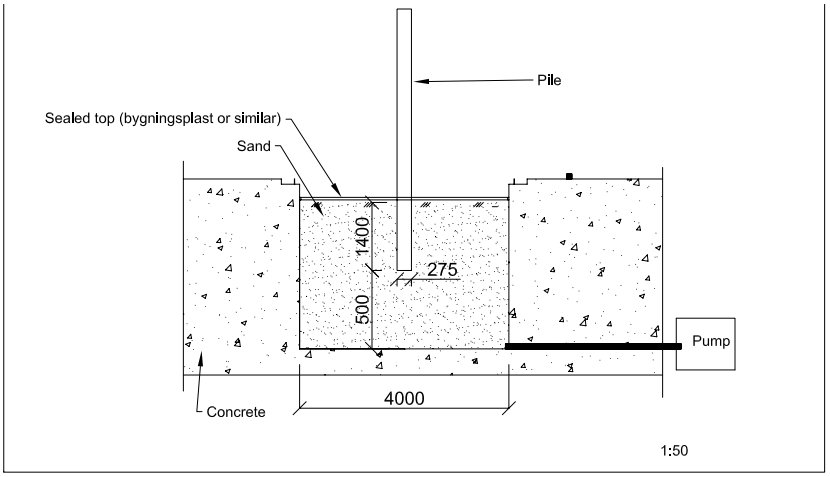

Figure C.1: Pile lab with pump

Appendix D

MATLAB Scripts and Functions

```
function tag=plotLVRecording(filename)

%%%%%%%%%%%%%%%%%%%%%%%%%%%%%%%%%%%%%%%%%%%%%%%%%%%%%%%%%%%%%%%%%%%%%%%%
%
% plotLVRecording.m
%
% Function for plotting the results generated by LabView
% for the PileLab Test. Indata must come in the form with 3
% accelerometers, and headerformat as specified in the
% current LabView-script.
%
%
%
%%%%%%%%%%%%%%%%%%%%%%%%%%%%%%%%%%%%%%%%%%%%%%%%%%%%%%%%%%%%%%%%%%%%%%%%

a = importdata(filename,'\t',23);

l = length(a.data);
tag.time = zeros(l,1);
tag.Acc1 = zeros(l,1);
tag.Acc2 = zeros(l,1);

for i=1:l
    tag.time(i) = a.data(i,1);
    tag.Acc1(i) = a.data(i,2);
    tag.Acc2(i) = a.data(i,3);
end
tag.text = a.textdata;
tag.dt = tag.time(2)-tag.time(1);
```

```
figure
subplot(3,1,1)
plot(tag.time,tag.Acc1,tag.time,tag.Acc2)
legend('Acc1','Acc2')
grid minor
xlabel('Time [s]')
ylabel('Acceleration [m/s^2]')
ylim([-10,10])

subplot(3,1,2)
plot(tag.time,tag.Acc1,'Color',[0,0.5,0])
legend('Acc1')
grid minor
xlabel('Time [s]')
ylabel('Acceleration [m/s^2]')
ylim([-10,10])

subplot(3,1,3)
plot(tag.time,tag.Acc2,'b')
legend('Acc2')
grid minor
xlabel('Time [s]')
ylabel('Acceleration [m/s^2]')
ylim([-10,10])


function FilteredTimeSeries=runFilter(TimeSeries,Length)

%%%%%%%%%%%%%%%%%%%%%%%%%%%%%%%%%%%%%%%%%%%%%%%%%%%%%%%%%%%%%%%%%%%%%%%
%
% FilteredTimeSeries.m
%
% Function based on http://www.mathworks.se/help/signal/ug/
% filtering-data-with-signal-processing-toolbox.html
%
% Executes zerophase lowpass filter that removes the
% frequenzy after a given frequenzy
%
%%%%%%%%%%%%%%%%%%%%%%%%%%%%%%%%%%%%%%%%%%%%%%%%%%%%%%%%%%%%%%%%%%%%%%%


d = fdesign.lowpass('N,Fc',100,30,Length);
Hd = design(d,'window','Window',kaiser(101,3));
FilteredTimeSeries = filtfilt(Hd.Numerator,1,TimeSeries);

%yzp = filtfilt(Hd.Numerator,1,tag.PileTop)
```

```
%%%%%%%%%%%%%%%%%%%%%%%%%%%%%%%%%%%%%%%%%%%%%%%%%%%%%%%%%%%%%%%%%%%%%%%%
% Script for determination of damping ratio based on
% logarithmic decrement
% Takes in recorded data from LABView
% Based on functions plotLVRecording.m and runFilter.m
%%%%%%%%%%%%%%%%%%%%%%%%%%%%%%%%%%%%%%%%%%%%%%%%%%%%%%%%%%%%%%%%%%%%%%%%
tag=plotLVRecording('2014-10-23 SL56kPa-5.lvm');
% importdata and split into column vectors
filtered=runFilter(tag.Acc2, length(tag.time));
% Filter the time series using runFilter
b=zeros(1,1);
c=zeros(1,1);
j=0;
% Use for loop to find the wave tops of the time series and
% add them to the
% vector b
        for i=2:(length(tag.time)-1)
            if filtered(i+1)<filtered(i) &&
            filtered(i-1)<filtered(i) && filtered(i)>0.05
                j=j+1;
                b(j)=tag.time(i);
                c(j)=filtered(i)
            end
        end
%Determination of system damping (logarithmic decrement)
zeta=zeros(1,1)
for m=1:(length(b)-1)
    zeta(m)=(1/(2*pi))*log(c(m)/c(m+1))
end

plot(c(1:m),zeta,'k')
xlabel('Amplitude [V]')
ylabel('Damping ratio [-]')
hold on


%%%%%%%%%%%%%%%%%%%%%%%%%%%%%%%%%%%%%%%%%%%%%%%%%%%%%%%%%%%%%%%%%%%%%%%%
% Plotting of strain gage measurmements for different
% overburden pressure
% Based on plotLVRecording.m and runFilter.m
%%%%%%%%%%%%%%%%%%%%%%%%%%%%%%%%%%%%%%%%%%%%%%%%%%%%%%%%%%%%%%%%%%%%%%%%
clear all
close all
% 0 kPa
tag1=plotLVRecording('2014-10-23 SL0kPa-2.lvm');
% importdata and split into column vectors
filtered=runFilter(tag1.Acc2, length(tag1.time));
% Filter the time series using runFilter
figure
```

```
plot(tag1.time,tag1.Acc2)
xlim([0 5])
ylim([-1.5 1])
title('Time series for overburden pressure of 0 kPa')
xlabel('Time [s]')
ylabel('Amplitude [V]')
daspect([1 4 1])
% 10 kPa
tag2=plotLVRecording('2014-10-23 SL10kPa-2.lvm');
% importdata and split into column vectors
filtered=runFilter(tag2.Acc2, length(tag2.time));
% Filter the time series using runFilter
figure
plot(tag2.time,tag2.Acc2)
ylim([-1.5 1])
xlim([0 5])
title('Time series for overburden pressure of 10 kPa')
xlabel('Time [s]')
ylabel('Amplitude [V]')
daspect([1 4 1])
% 20 kPa
tag3=plotLVRecording('2014-10-23 SL20kPa-2.lvm');
% importdata and split into column vectors
filtered=runFilter(tag3.Acc2, length(tag3.time));
% Filter the time series using runFilter
figure
plot(tag3.time,tag3.Acc2)
xlim([0 5])
ylim([-1.5 1])
title('Time series for overburden pressure of 20 kPa')
xlabel('Time [s]')
ylabel('Amplitude [V]')
daspect([1 4 1])
% 30 kPa
tag4=plotLVRecording('2014-10-23 SL30kPa-2.lvm');
% importdata and split into column vectors
filtered=runFilter(tag4.Acc2, length(tag4.time));
% Filter the time series using runFilter
figure
plot(tag4.time,tag4.Acc2)
xlim([0 5])
ylim([-1.5 1])
title('Time series for overburden pressure of 30 kPa')
xlabel('Time [s]')
ylabel('Amplitude [V]')
daspect([1 4 1])
% 40 kPa
tag5=plotLVRecording('2014-10-23 SL40kPa-2.lvm');
% importdata and split into column vectors
```

```
filtered=runFilter(tag5.Acc2, length(tag5.time));
% Filter the time series using runFilter
figure
plot(tag5.time,tag5.Acc2)
xlim([0 5])
ylim([-1.5 1])
title('Time series for overburden pressure of 40 kPa')
xlabel('Time [s]')
ylabel('Amplitude [V]')
daspect([1 4 1])
% 56 kPa
tag6=plotLVRecording('2014-10-23 SL56kPa-2.lvm');
% importdata and split into column vectors
filtered=runFilter(tag6.Acc2, length(tag6.time));
% Filter the time series using runFilter
figure
plot(tag6.time,tag6.Acc2)
xlim([0 5])
ylim([-1.5 1])
title('Time series for overburden pressure of 56 kPa')
xlabel('Time [s]')
ylabel('Amplitude [V]')
daspect([1 4 1])
```

Appendix E

Parameter Evaluation for HSS

The parameters for the HSS model were determined based on laboratory tests and empirical formulas as by Brinkgreve et al. (2010).

Moen (1978) performed oedometer tests on the Hokksund sand to investigate its stiffness parameters. These results were backcalculated using Soil Test in PLAXIS. Figure xx shows a comparison of a laboratory test with a porosity of 39 %.

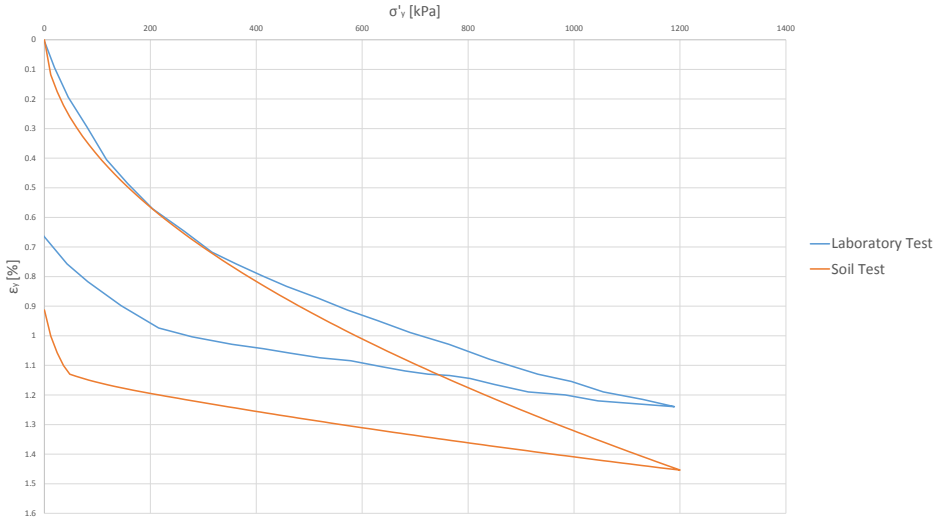

Figure E.1: Back-calculation of oedometer test

The test shows a decent fit using $E_{oed}^{ref} = 50$ MPa, $E_{ur}^{ref} = 200000$ and $m = 0.48$. However, the stress exponent m must be set to a unrealistically high value to obtain a good fit for the entire curve. Since only one stress exponent can be used in the HSS model, it was considered more correct to use the one found according to shear wave measurements. The unloading-reloading stiffness was also found to be unrealistically high. Seeing as the unloading-reloading stiffness in PLAXIS acts as a cut-off stiffness in the stiffness reduction curve, a high E_{ur} will significantly reduce the damping quantities of the soil. Table xx shows a comparison of the values found from different tests and calculated vaules based on Brinkgreve et al. (2010):

Parameter	Symbol	Unit	Test	Empirical
Oedometer stiffness	E_{oed}^{ref}	$[MPa]$	50	46
Secant stiffness	E_{50}^{ref}	$[MPa]$	-	46
Unloading-reloading stiffness	E_{ur}^{ref}	$[MPa]$	200	138
Shear stiffness	G_0	$[MPa]$	100	112
Stress exponent	m	$[-]$	0.48	0.46
Threshold shear strain	$\gamma_{0.7}$	$[-]$	-	1.2×10^{-4}
Friction angle	ϕ	$[^\circ]$	38	38
Failure ratio	R_f	$[-]$	-	0.9

Table E.1: Comparison between test data and empirical values based on Brinkgreve et al. (2010)

Where reliable test data exist as for G_0, m and ϕ, these values were used. However, there exist significant uncertainties with regards to other parameters. There exist no test data for $\gamma_{0.7}$ and R_f. These are therefore taken as in table xx. The oedometer stiffness was found to be around 50 MPa, while the secant stiffness $E_{50}^{ref} = E_{oed}^{ref}$. The measured E_{ur}^{ref} was considered to be too high and a value of $E_{ur}^{ref} = 3 \times E_{oed}^{ref}$.

Appendix F

Interface Stresses

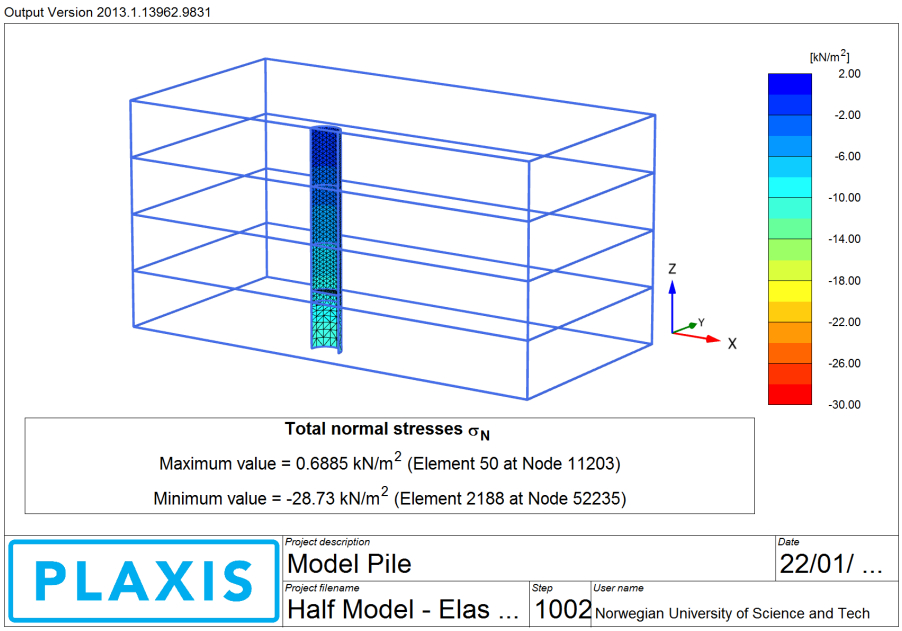

Figure F.1: Example of interface normal stresses

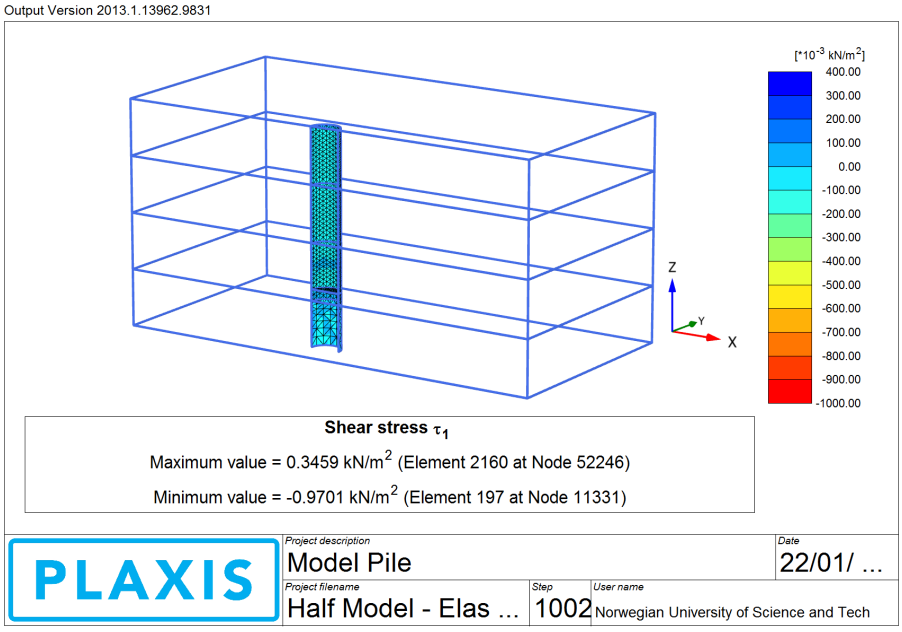

Figure F.2: Example of interface shear stress

Appendix G

Shear Strain Profiles Linear Elastic

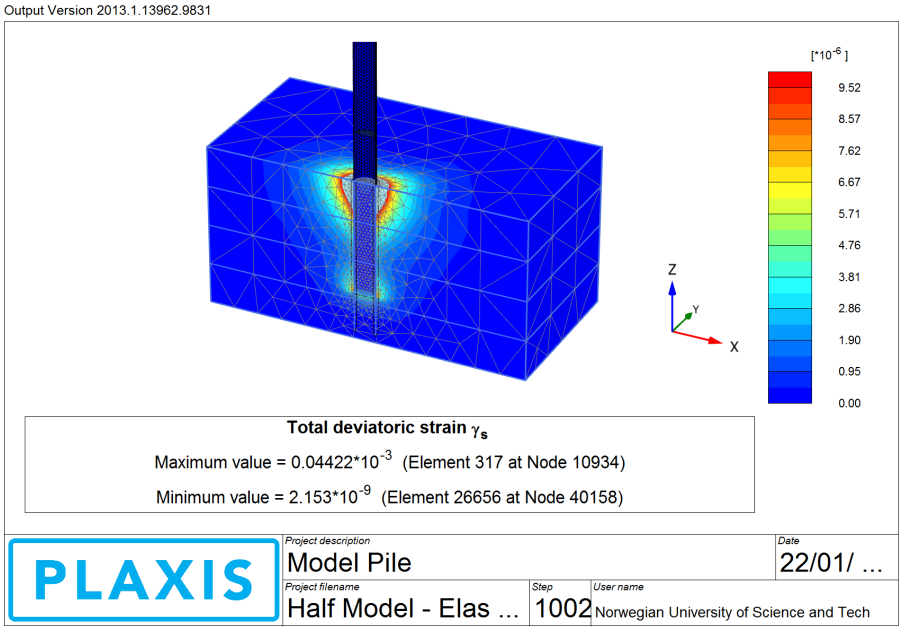

Figure G.1: Shear strain profile for 0 kPa overburden pressure

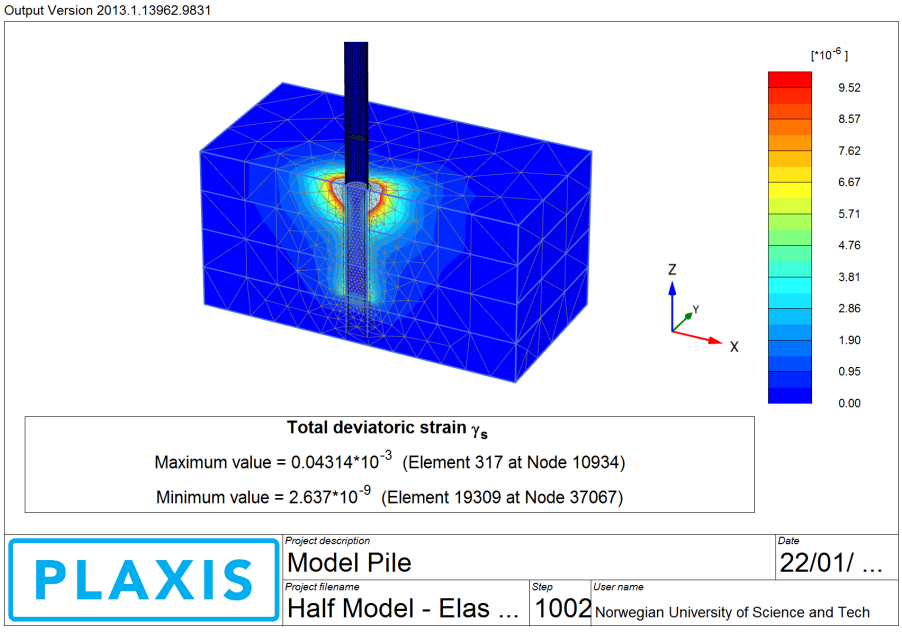

Figure G.2: Shear strain profile for 10 kPa overburden pressure

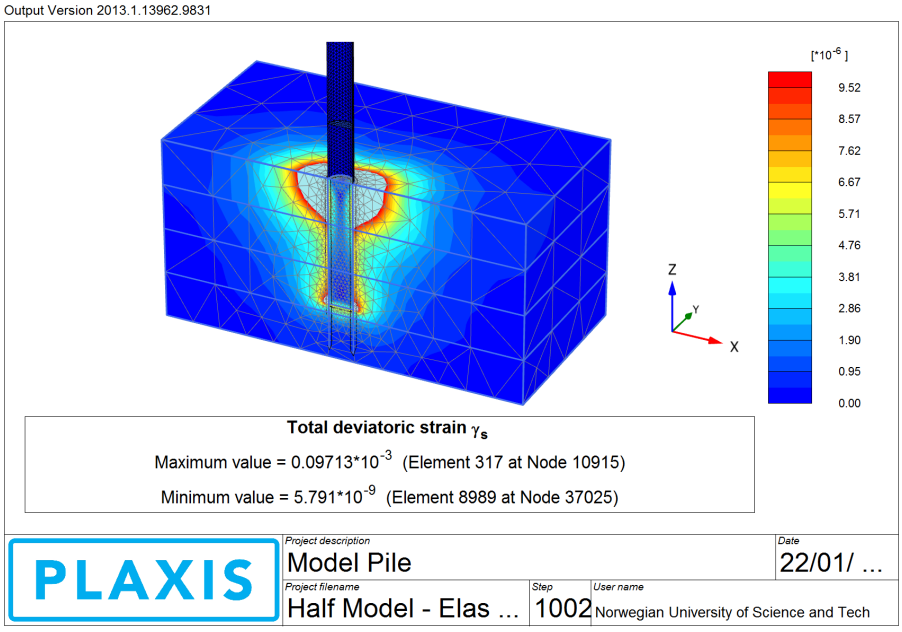

Figure G.3: Shear strain profile for 20 kPa overburden pressure

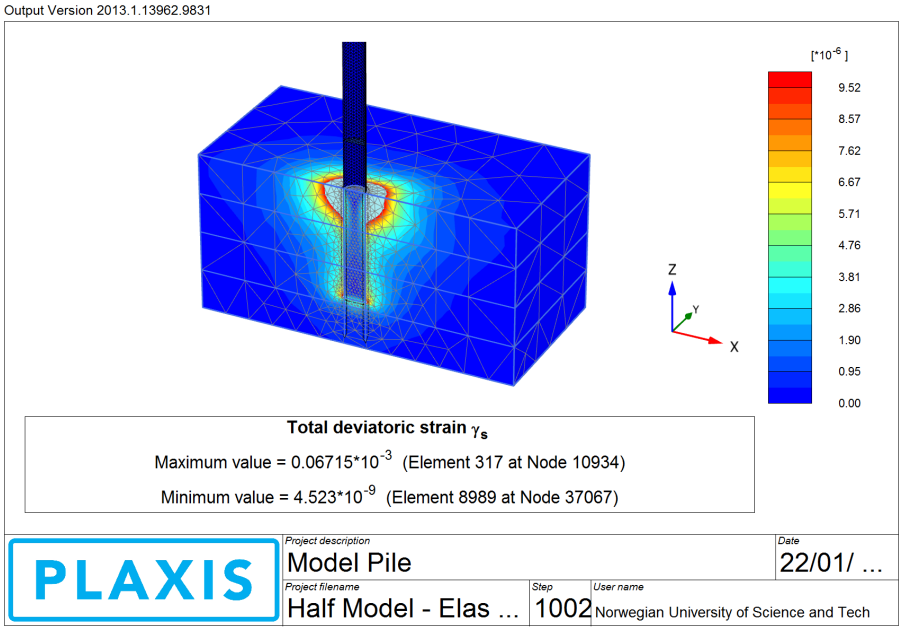

Figure G.4: Shear strain profile for 30 kPa overburden pressure

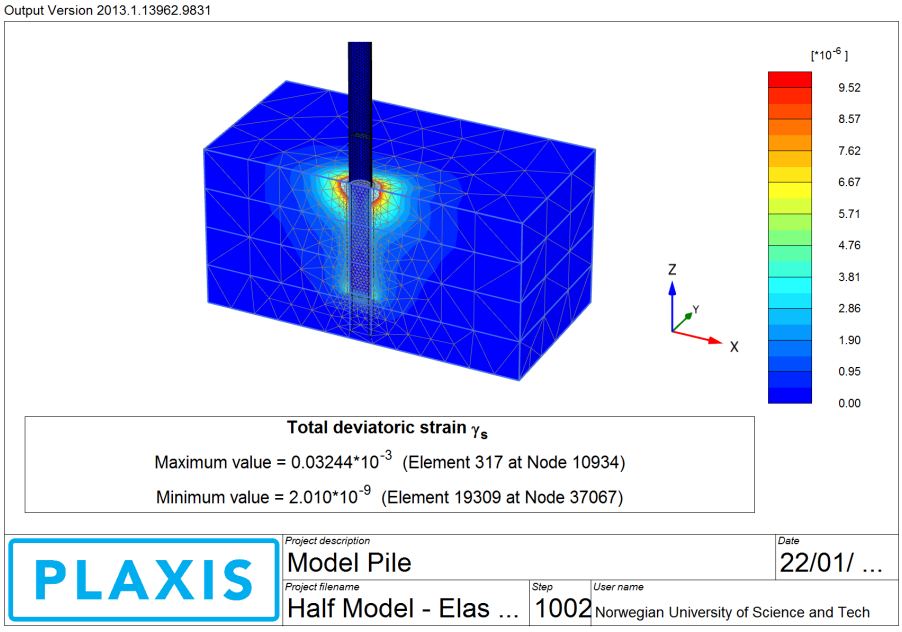

Figure G.5: Shear strain profile for 40 kPa overburden pressure

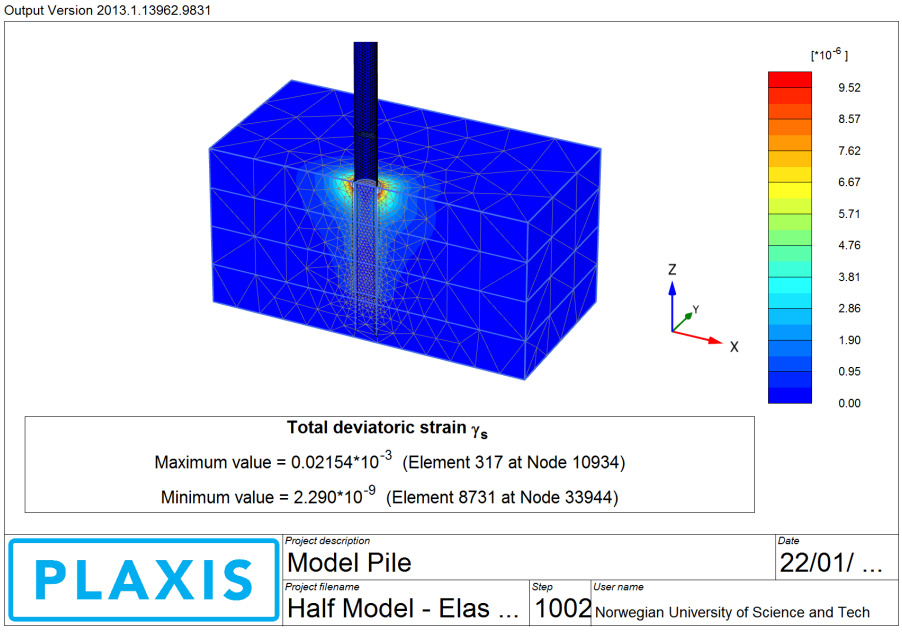

Figure G.6: Shear strain profile for 56 kPa overburden pressure

Appendix H

Shear Strain Profiles HSS

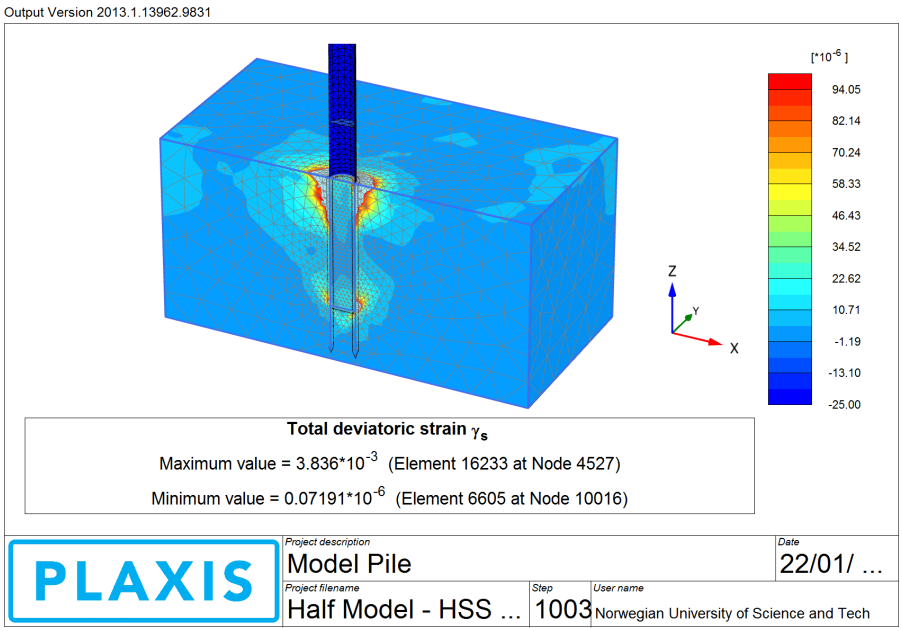

Figure H.1: Shear strain profile for 0 kPa overburden pressure

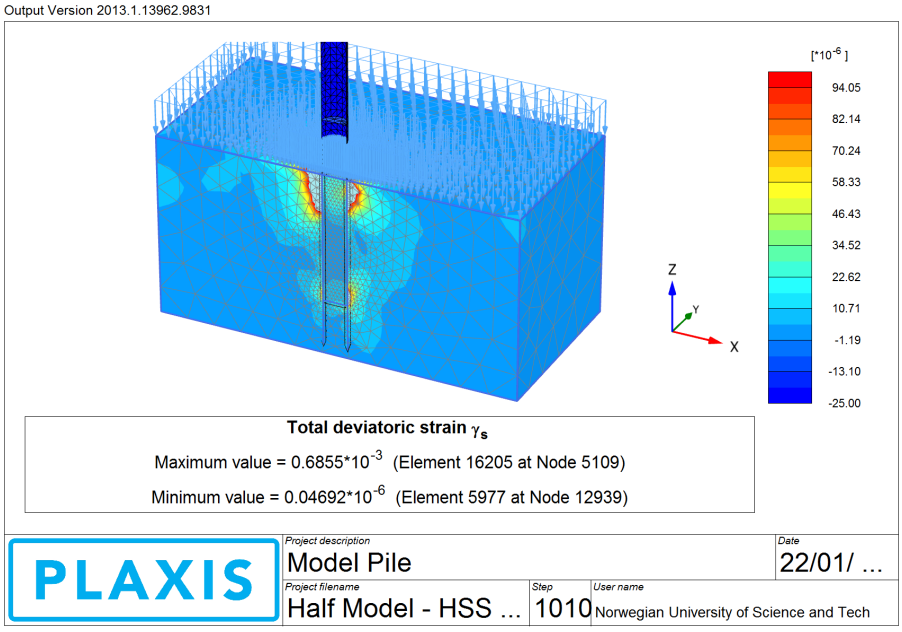

Figure H.2: Shear strain profile for 10 kPa overburden pressure

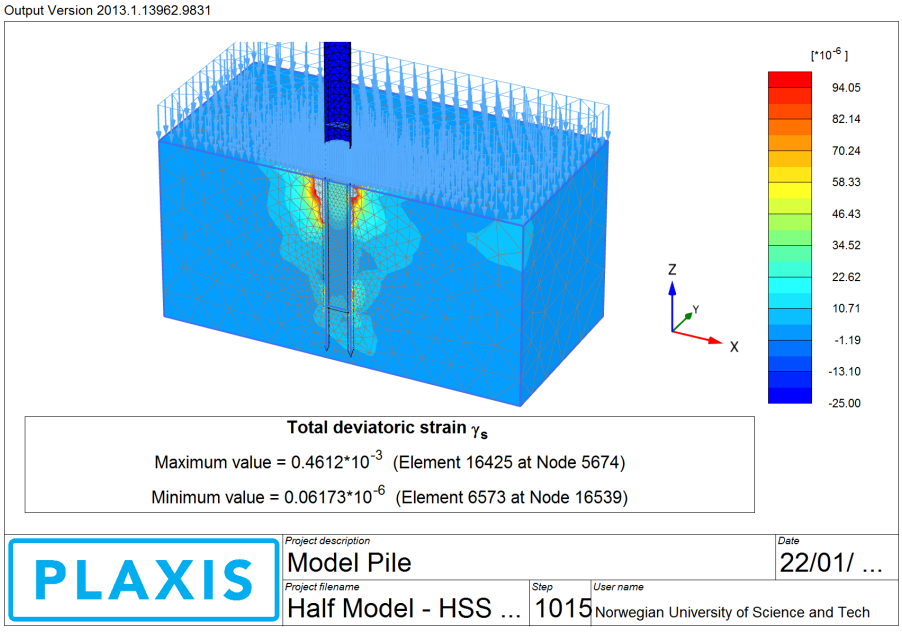

Figure H.3: Shear strain profile for 20 kPa overburden pressure

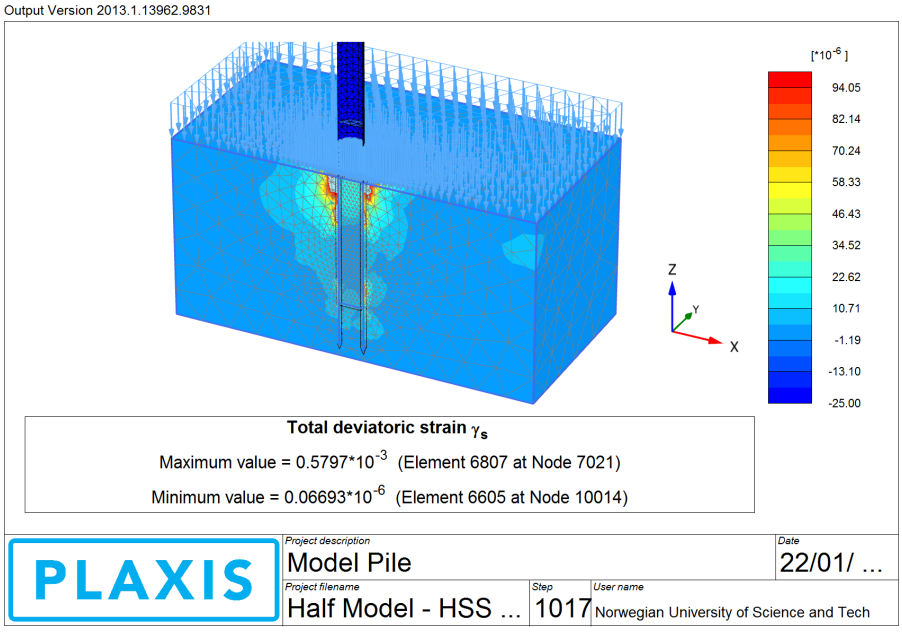

Figure H.4: Shear strain profile for 30 kPa overburden pressure

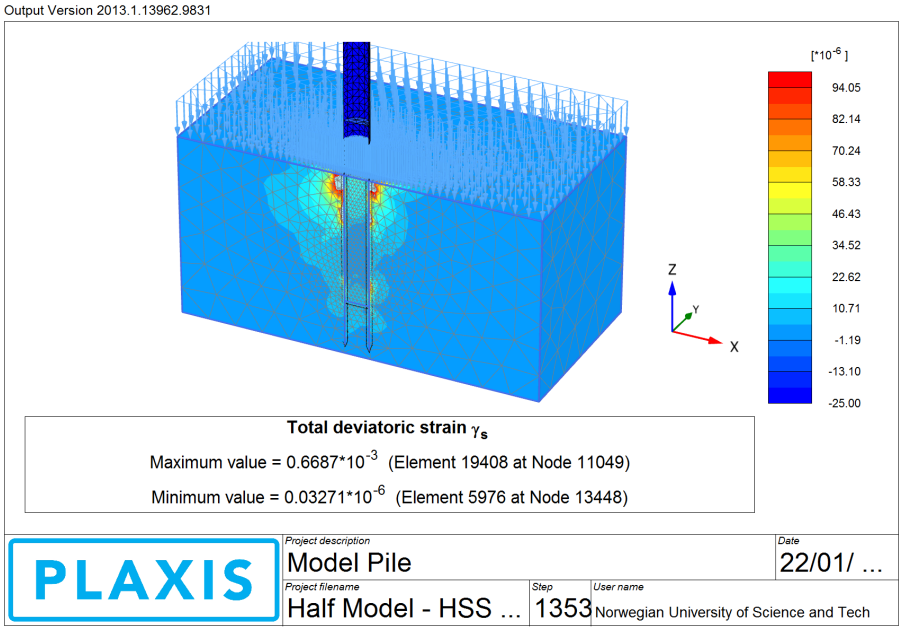

Figure H.5: Shear strain profile for 40 kPa overburden pressure

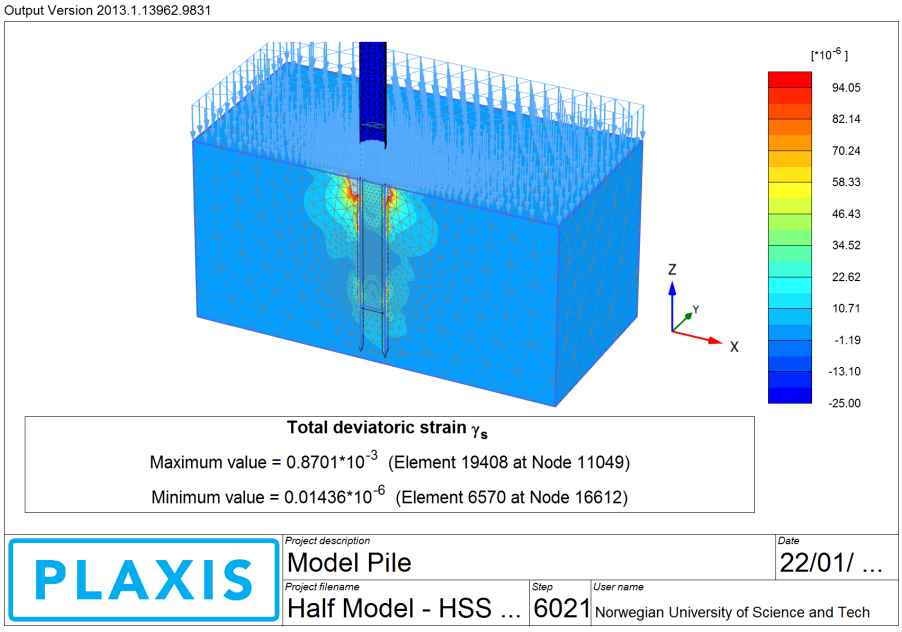

Figure H.6: Shear strain profile for 56 kPa overburden pressure

Appendix I

Stiffness G/G_{ur}

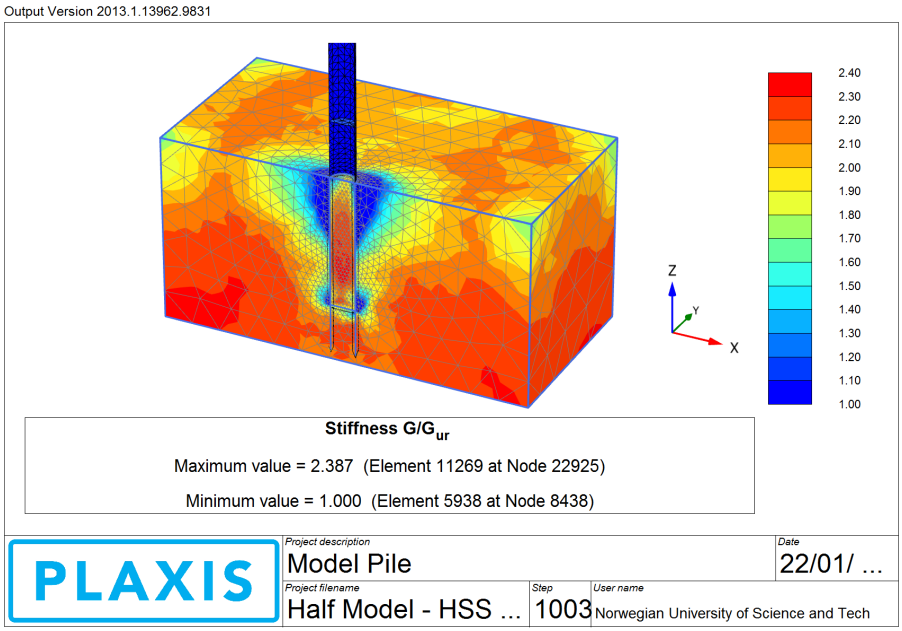

Figure I.1: Stiffness profile for 0 kPa overburden pressure as used by HSS model

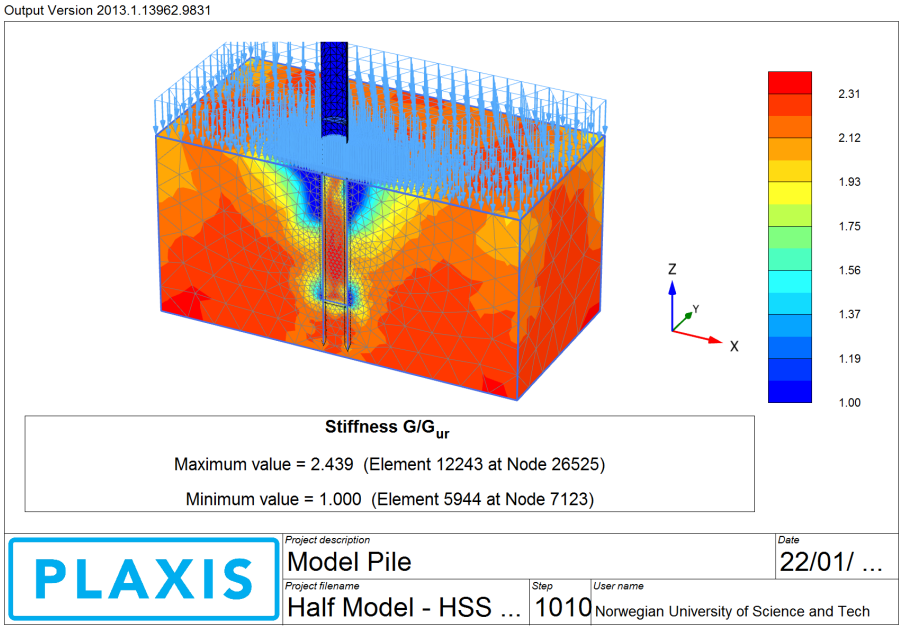

Figure I.2: Stiffness profile for 10 kPa overburden pressure as used by HSS model

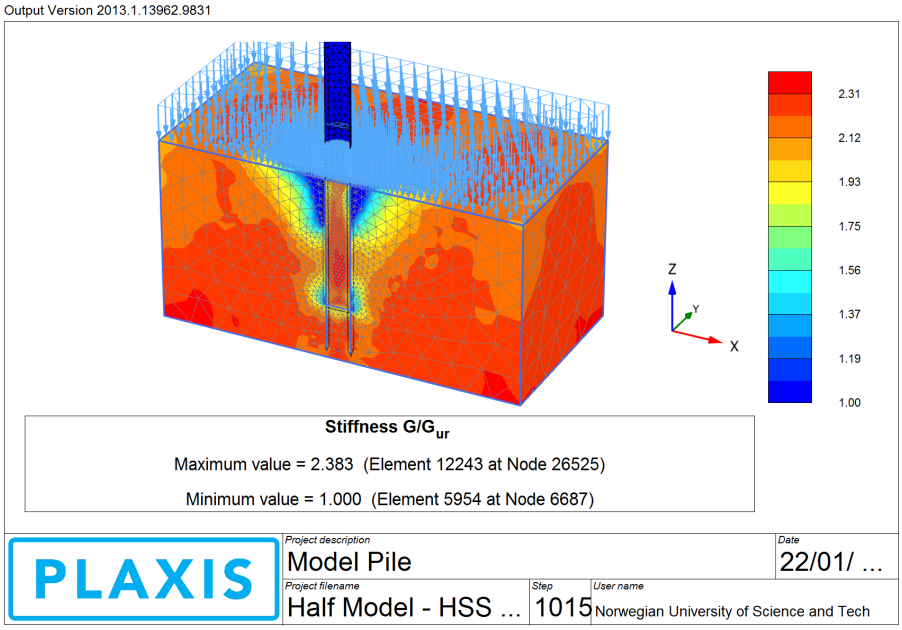

Figure I.3: Stiffness profile for 20 kPa overburden pressure as used by HSS model

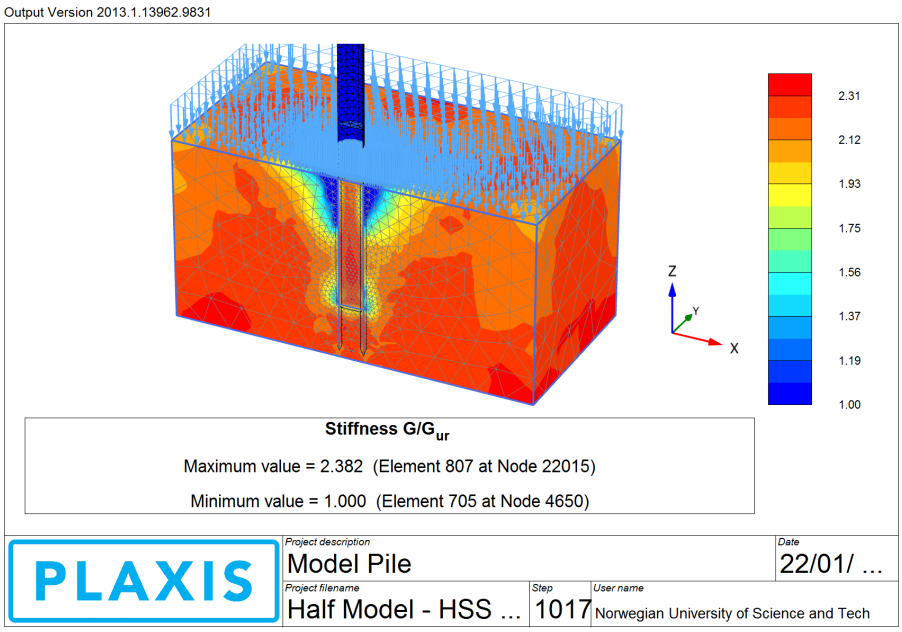

Figure I.4: Stiffness profile for 30 kPa overburden pressure as used by HSS model

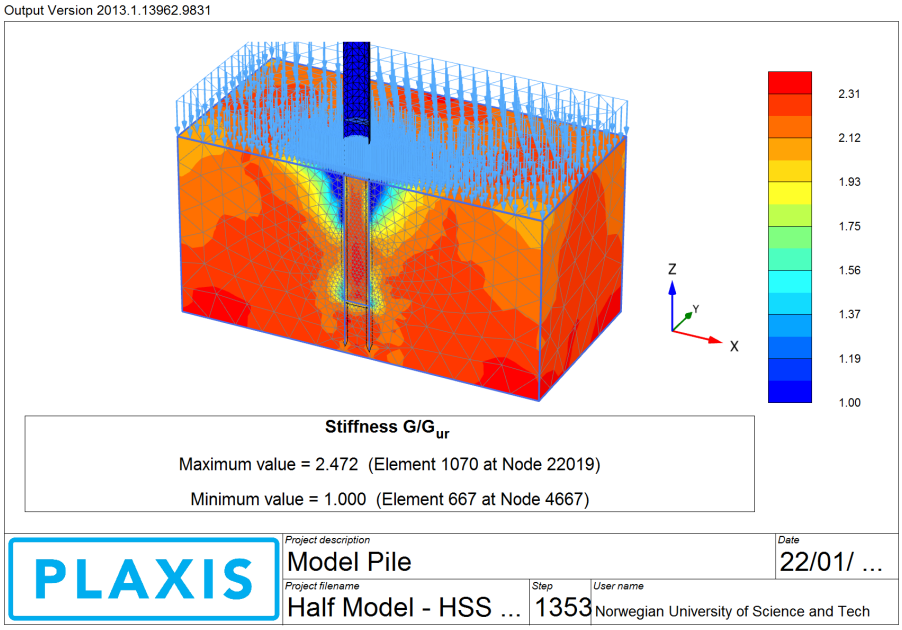

Figure I.5: Stiffness profile for 40 kPa overburden pressure as used by HSS model

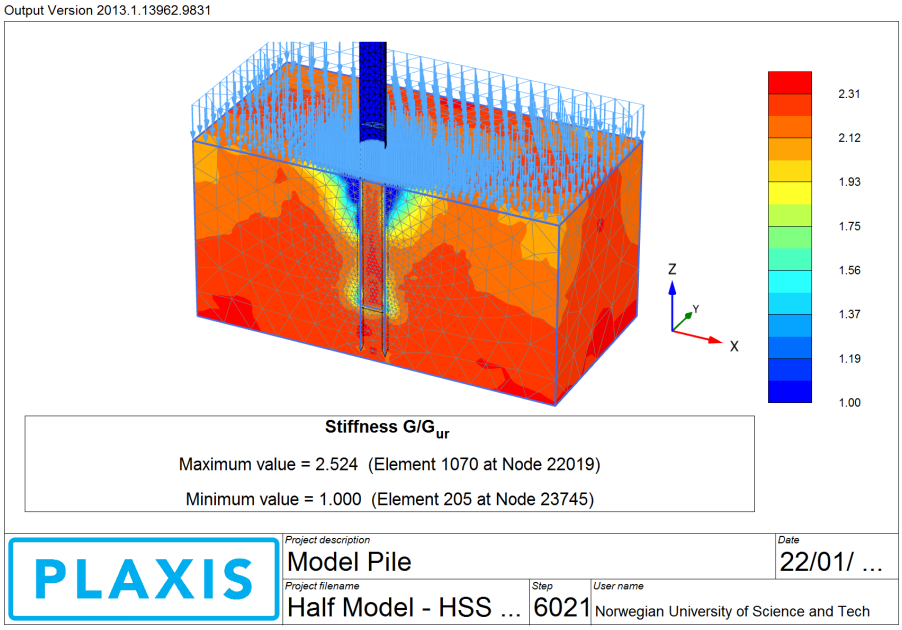

Figure I.6: Stiffness profile for 56 kPa overburden pressure as used by HSS model